



# LUND UNIVERSITY

## Development of Single Nanowire Optoelectronic Devices

Lamers, Nils

2025

[Link to publication](#)

*Citation for published version (APA):*

Lamers, N. (2025). *Development of Single Nanowire Optoelectronic Devices*. Lund University.

*Total number of authors:*

1

### General rights

Unless other specific re-use rights are stated the following general rights apply:

Copyright and moral rights for the publications made accessible in the public portal are retained by the authors and/or other copyright owners and it is a condition of accessing publications that users recognise and abide by the legal requirements associated with these rights.

- Users may download and print one copy of any publication from the public portal for the purpose of private study or research.
- You may not further distribute the material or use it for any profit-making activity or commercial gain
- You may freely distribute the URL identifying the publication in the public portal

Read more about Creative commons licenses: <https://creativecommons.org/licenses/>

### Take down policy

If you believe that this document breaches copyright please contact us providing details, and we will remove access to the work immediately and investigate your claim.

LUND UNIVERSITY

PO Box 117  
221 00 Lund  
+46 46-222 00 00



# Development of Single Nanowire Optoelectronic Devices

NILS LAMERS

DEPARTMENT OF PHYSICS | FACULTY OF SCIENCE | LUND UNIVERSITY





## Development of Single Nanowire Optoelectronic Devices





# Development of Single Nanowire Optoelectronic Devices

Nils Lamers



**LUND**  
UNIVERSITY

DOCTORAL DISSERTATION

by due permission of the Faculty Science, Lund University, Sweden.  
To be defended on Friday, March 21<sup>st</sup>, 2025, at 9:15 in the Rydberg lecture  
hall at the Department of Physics, Professorsgatan 1, Lund, Sweden.

*Faculty opponent*  
Prof. Maarten Roeffaers  
KU Leuven, Belgium

<b>Organization</b> LUND UNIVERSITY		<b>Document name</b> Doctoral Dissertation	
<b>Author(s)</b> Nils Lamers		<b>Date of issue</b> 2025-03-21	
		Sponsoring organization	
<b>Title and subtitle</b> Development of Single Nanowire Optoelectronic Devices			
<b>Abstract</b> <p>Semiconductor nanowires (NW) have been of interest to optoelectronics research for several decades due to the unique optical effects resulting from their geometry. Today, NWs are fabricated from a wide range of materials, ranging from Si to III-Vs and emerging materials like metal-halide perovskites (MHPs). Among NW devices, single NW devices are of special interest because they offer both a useful low-dimensional test platform for transport and optical phenomena and because they have potential for ultra-high-resolution applications, which could surpass currently established display and photodetector array technologies. At the same time, single NW devices represent a unique challenge to semiconductor processing, requiring a high degree of precision and control.</p> <p>This thesis addresses the manufacturing challenges of two optoelectronic materials systems by developing novel processes for manufacturing single NW devices. For the III-V InP, an established semiconductor, this challenge consists in pushing from larger area vertical NW devices towards single vertical NW devices which ultimately unlock ultra-high-resolution photodetector and display applications. For the MHP CsPbBr<sub>3</sub>, the challenge consists of pushing towards nanostructured devices that can combine the advantages of MHPs with nanoscale engineering. This in turn requires a re-development and re-thinking of established processes in an MHP-compatible manner.</p> <p>Papers I and II address vertical single NW InP devices, a device geometry which has been rarely reported but is ultimately necessary for photodetector and display applications based on single InP NWs. The devices are based on single vertical NWs of 60 nm diameter, contacted inside a NW array (paper I). We demonstrate a high yield fabrication process for quality single NW devices with ideality factors as low as <math>n = 1.8</math>. These NWs work as LEDs, solar cells, and photodetectors. We take advantage of the low NW diameter to use the single NW photodetectors for ultra-high-resolution imaging of an optical focus at a 70 nm step size. The resulting images allow us to characterise the beam parameters but also reveal additional details in the intensity distribution which may be invisible with other methods (paper II).</p> <p>Papers III to VI address the nanofabrication of MHPs, specifically horizontal CsPbBr<sub>3</sub> NWs. Papers III and VI deal with CsPbBr<sub>3</sub> NW solvent-based synthesis using anodised aluminium oxide templates, a low-cost method when compared to the established metal-organic vapour phase methods used for III-V materials. Paper IV develops an MHP-compatible electron-beam lithography processes which allows us to create nanostructured contacts of our CsPbBr<sub>3</sub> NWs. In paper V, we demonstrate a gas-phase anion exchange process to create CsPb(Br<sub>1-x</sub>Cl<sub>x</sub>)<sub>3</sub> NWs from CsPbBr<sub>3</sub> NWs. We demonstrate how the combination of the EBL and anion exchange processes can be used to create heterostructured NWs which could form the building blocks of future nanostructured MHP optoelectronic devices.</p>			
<b>Key words</b> Nanowire, Metal-halide perovskite, III-V semiconductor, photodetector, EBL			
Classification system and/or index terms (if any)			
Supplementary bibliographical information		<b>Language</b> English	
ISSN and key title		<b>ISBN</b> 978-91-8104-406-5 (print) 978-91-8104-407-2 (electronic)	
Recipient's notes	<b>Number of pages</b> 204	Price	
	Security classification		

I, the undersigned, being the copyright owner of the abstract of the above-mentioned dissertation, hereby grant to all reference sources permission to publish and disseminate the abstract of the above-mentioned dissertation.

Signature

Date 2025-03-21

# Development of Single Nanowire Optoelectronic Devices

Nils Lamers



**LUND**  
UNIVERSITY

Copyright pp i-64, front cover, back cover Nils Lamers

Paper 1 © The Authors. Published by American Chemical Society under CC BY 4.0

Paper 2 © The Authors. Published by American Chemical Society under CC BY 4.0

Paper 3 © The Authors. Published by Wiley-VCH GmbH under CC BY 4.0

Paper 4 © The Authors. Published by American Chemical Society under CC BY 4.0

Paper 5 © The Authors. Published by IOP Publishing Ltd

Paper 6 © The Authors (Manuscript unpublished)

Division of Synchrotron Radiation Research

Department of Physics, Faculty of Science

Lund University

ISBN 978-91-8104-406-5 (print)


ISSN 978-91-8104-407-2 (electronic)

Printed in Sweden by Media-Tryck, Lund University

Lund 2025



Media-Tryck is a Nordic Swan Ecolabel  
certified provider of printed material.  
Read more about our environmental  
work at [www.mediatryck.lu.se](http://www.mediatryck.lu.se)

**MADE IN SWEDEN** 

# Table of Contents

Abstract.....	i
Acknowledgements .....	iii
Popular Science Summary.....	v
List of Papers .....	vii
Publications included in this thesis .....	vii
Publications not included in this thesis .....	ix
Abbreviations .....	xi
<b>1 Introduction .....</b>	<b>1</b>
<b>2 Semiconductors .....</b>	<b>4</b>
2.1 <i>pn</i> -junctions and diodes .....	4
2.2 Optoelectronics.....	7
2.2.1 Photocurrent and solar cells .....	7
2.2.2 Carrier recombination.....	8
2.2.3 Photo- and electroluminescence.....	9
<b>3 Vertical single InP nanowire devices.....</b>	<b>10</b>
3.1 Fabrication.....	11
3.1.1 NW seed particles .....	12
3.1.2 Nanowire growth.....	12
3.1.3 Insulation layer .....	13
3.1.4 Isolation layer.....	13
3.1.5 Top contacts.....	14
3.1.6 BCB and PECVD SiO <sub>2</sub> – a comparison .....	15
3.2 Characterisation.....	15
3.2.1 Single nanowire diode.....	16
3.2.2 Single nanowire solar cell.....	17
3.2.3 Single nanowire LED.....	17
3.3 Sub-wavelength imaging using a single nanowire detector.....	19
3.3.1 Setup .....	20



3.3.2	Calibration of photoresponse .....	20
3.3.3	Characterisation of focal spot .....	21
3.3.4	Modelling of imaging with single nanowire detector .....	22
3.3.5	Imaging of a dense diffraction pattern .....	23
<b>4</b>	<b>Horizontal single nanowire CsPbBr<sub>3</sub> devices .....</b>	<b>25</b>
4.1	Basic properties of MHPs and CsPbBr <sub>3</sub> .....	27
4.1.1	The perovskite crystal .....	27
4.1.2	MHP synthesis .....	28
4.1.3	Properties of CsPbBr <sub>3</sub> and CsPb(Br <sub>1-x</sub> Cl <sub>x</sub> ) <sub>3</sub> .....	28
4.2	Synthesis of free-standing CsPbBr <sub>3</sub> nanowires via AAO templates .....	29
4.2.1	Anodised aluminium oxide .....	29
4.2.2	Growth of free-standing CsPbBr <sub>3</sub> nanowires .....	30
4.2.3	Improvement of growth via controlled-flow reactor .....	32
4.3	Horizontal single CsPbBr <sub>3</sub> nanowire devices .....	33
4.3.1	Lift-off processing .....	33
4.3.2	MHP-compatible EBL with PMMA resist .....	34
4.3.3	Fabrication of horizontal single CsPbBr <sub>3</sub> nanowire devices .....	36
4.3.4	Optoelectronic characterisation .....	37
4.4	Anion exchange for CsPb(Br <sub>1-x</sub> Cl <sub>x</sub> ) <sub>3</sub> nanowires .....	38
4.4.1	Anion exchange processing with HCl and Cl <sub>2</sub> gases .....	39
4.4.2	Correlating PL and EDS with anion exchange .....	40
4.4.3	Anion exchange behaviour of HCl and Cl <sub>2</sub> processes .....	41
4.4.4	Modelling the diffusion into a nanowire .....	43
4.5	Heterostructured CsPbBr <sub>3</sub> /CsPb(Br <sub>1-x</sub> Cl <sub>x</sub> ) <sub>3</sub> nanowires .....	45
4.5.1	Self-aligned free-standing heterojunctions .....	45
4.5.2	Nanostructured heterojunctions in horizontal nanowires .....	45
<b>5</b>	<b>Conclusions and Outlook .....</b>	<b>48</b>
<b>6</b>	<b>References .....</b>	<b>50</b>

# Abstract

Semiconductor nanowires (NW) have been of interest to optoelectronics research for several decades due to the unique optical effects resulting from their geometry. Today, NWs are fabricated from a wide range of materials, ranging from Si to III-Vs and emerging materials like metal-halide perovskites (MHPs). Among NW devices, single NW devices are of special interest because they offer both a useful low-dimensional test platform for transport and optical phenomena and because they have potential for ultra-high-resolution applications, which could surpass currently established display and photodetector array technologies. At the same time, single NW devices represent a unique challenge to semiconductor processing, requiring a high degree of precision and control.

This thesis addresses the manufacturing challenges of two optoelectronic materials systems by developing novel processes for manufacturing single NW devices. For the III-V InP, an established semiconductor, this challenge consists in pushing from larger area vertical NW devices towards single vertical NW devices which ultimately unlock ultra-high-resolution photodetector and display applications. For the MHP CsPbBr<sub>3</sub>, the challenge consists of pushing towards nanostructured devices that can combine the advantages of MHPs with nanoscale engineering. This in turn requires a re-development and re-thinking of established processes in an MHP-compatible manner.

Papers I and II address vertical single NW InP devices, a device geometry which has been rarely reported but is ultimately necessary for photodetector and display applications based on single InP NWs. The devices are based on single vertical NWs of 60 nm diameter, contacted inside a NW array (paper I). We demonstrate a high yield fabrication process for quality single NW devices with ideality factors as low as  $n = 1.8$ . These NWs work as LEDs, solar cells, and photodetectors. We take advantage of the low NW diameter to use the single NW photodetectors for ultra-high-resolution imaging of an optical focus at a 70 nm step size. The resulting images allow us to characterise the beam parameters but also reveal additional details in the intensity distribution which may be invisible with other methods (paper II).

Papers III to VI address the nanofabrication of MHPs, specifically horizontal CsPbBr<sub>3</sub> NWs. Papers III and VI deal with CsPbBr<sub>3</sub> NW solvent-based synthesis using anodised

aluminium oxide templates, a low-cost method when compared to the established metal-organic vapour phase methods used for III-V materials. Paper IV develops an MHP-compatible electron-beam lithography processes which allows us to create nanostructured contacts of our CsPbBr<sub>3</sub> NWs. In paper V, we demonstrate a gas-phase anion exchange process to create CsPb(Br<sub>1-x</sub>Cl<sub>x</sub>)<sub>3</sub> NWs from CsPbBr<sub>3</sub> NWs. We demonstrate how the combination of the EBL and anion exchange processes can be used to create heterostructured NWs which could form the building blocks of future nanostructured MHP optoelectronic devices.

# Acknowledgements

Around half a year ago, I was on a train with Kristi who was about to finish his PhD. As we discussed whether anyone would ever bother reading our theses, a stranger remarked that this part, the acknowledgements, would most certainly be read. And that is for good reason. I could not have accomplished any of the work within this thesis by myself, a lot of work has gone into this thesis by other people who have helped me along the way.

First, of course, I want to thank my main supervisor Jesper Wallentin for all the guidance throughout my studies. You were always patient enough to let me follow my curiosities but knew when and how to get me to wrap up a project and tie it all up neatly. I would also like to thank my co-supervisor Magnus Borgström, who always had an open door to answer any questions or discuss. Although it was a long walk, I always left your office knowing how to proceed.

My thanks and appreciation to Zhaojun and Ziyun, my fellow travellers in all things perovskite nanoprocessing. It was great working with you. Thanks to Lert for taking the time to teach me. To Dmitry, Hanna, Huaiyu, Lucas, Meghan, Klara, and Sanna: thank you for being an amazing and welcoming group, even though my work had little to do with X-rays. Thanks also for all the interesting processing challenges whenever there was a beam time, it made for a great bunch of sideprojects. Thanks also to Jesper L., I had a lot of fun working with and teaching you.

Thanks to everyone at Synchrotron radiation for all the fika, kick-offs, and for making our division a great place to work. To Vidar for sharing all my cleanroom woes, for all the gym, and all the beers. To Yen-Po for being the most genuinely wholesome person I have ever met and for taking me on my first beamtime. To Ahmed for all the supporting words and encouragement. To Patrik, for always being helpful and funny at the same time.

At FTF and the NanoLab, my second home, I want to give a big thanks go to Lukas and Kristi for the nanowire growth and all the related discussion, as well as those that went beyond just science. Thanks also to David, Yue, Hossein, and many other users of the cleanroom for being open to discussions on processing or teaching me on tools. Thanks to Asmita for her help. To the NanoLund innebandy group, thanks for all the

great games. I am grateful to Claes and Dan for letting me borrow their equipment without any fuss and helping me out patiently. A lot of credit to the cleanroom staff for all the hard work that they do and for always being open to accommodating new ideas. None of this could have happened without help from Natalia, Håkan, George, Dmitry, Anders, Peter, David, Elvedin, Alex, and Luke. I am sorry about that month when everything broke while I was using it, I promise it wasn't my fault.

To Arky and Lea, thanks for being the best, most supportive friends one could ever ask for. Thanks to Illya, Lavie, and Spencer for all the shenanigans, you made many stressful times a lot more bearable. Thanks to my parents and brother for all the support, even when I am tough to deal with. Finally, thanks to my wife Mariia for all the love, help, and encouragement. You are the best!

# Popular Science Summary

A critical component to our modern lives is the back-and-forth conversion of light to electricity and electricity to light. Our homes are lit with light-emitting diodes (LEDs) converting electricity into light and our phones, TVs, and other screens use many thousands of LEDs to display information. When we take an image with our phones or other digital cameras, we record light by converting it into electric signals. The same is true when we share it digitally with our friends and family, as laser light races down fibreoptic cables to convey information. And in an ever-increasing effort to make these luxuries sustainable, we try to power it in part via solar panels which convert sunlight into electric power.

We ask of our devices to improve in many ways: for our displays and cameras to increase in resolution and colour accuracy, for our telecommunications to become faster, and for it all to be more energy efficient. This continued drive for improved device performance requires a large scientific effort to keep up with expectations. Two key changes we can make to our devices lie in their geometry and material.

For optoelectronics, nanowires are a geometric shape that is of great promise. Nanowires are crystals with a diameter on the order of tens to hundreds of nanometres but a length of several micrometres. Since nanowires are generally comparable in diameter to the wavelengths of visible light, their shape allows for many interesting interactions with light. Just like fibreoptic cables which transport light to allow for communication, nanowires are also often light guiding. This makes them great for directional light-emission and detection applications. Due to interactions between their diameter and the wavelengths of light, the specific absorption and emission properties can be fine-tuned by simply adjusting the nanowire diameter. While nanowires come in many materials, I have worked on nanowires from two promising optoelectronic materials.

The first is indium phosphide (InP) which nowadays is commonplace in telecommunications where it is used to both emit and detect signals sent via optical fibres. I have focused on fabricating devices made from single InP nanowires standing vertically on top of the substrate. This allows us to macroscopically align the nanowire by adjusting the macroscopic position of the substrate. These single nanowires function



as solar cells, photodetectors, and light-emitting diodes (although not in the visible spectrum). Each device is one small single pixel, around ten times smaller than the wavelength of light and 20 to 40 times smaller than the pixels used in your phone's camera. Using these devices, I was able to record images of the shape of a focused laser using a spatial step size around 10 times smaller than the wavelength of the laser light.

The second material I focused on was caesium lead bromide ( $\text{CsPbBr}_3$ ), a metal-halide perovskite (MHP). These materials are not yet in widespread use but have shown increasing promise for solar cell and other optoelectronic applications. Just like table salt, MHPs are ionic crystals which are highly soluble in water and other polar solvents. This represents both a challenge and an opportunity. On one hand, these materials are easily grown from solutions. Especially for nanoscale materials, they can be grown by making the solution conform to a nanoscale template akin to how ice cubes of all shapes can be made with fancy ice cube trays. I make use of this in this thesis to grow MHP nanowires.

On the other hand, water and polar solvents are in ubiquitous use not just in everyday life but also in cleanroom processing. This represents a major challenge if we intend to use MHP materials for applications like displays and cameras because without cleanroom processing methods we cannot define pixels at resolutions that match modern devices. I therefore developed a new chemical process for using an established patterning process on these materials, the potential of which is demonstrated by its use in creating single  $\text{CsPbBr}_3$  nanowire devices.

Lastly, I worked on characterising a process which allows for the conversion of one type of MHP material to a different MHP material. This change in composition changes the colour of light which would be emitted from LEDs made from these materials. In established semiconductors, such composition changes must be made during the growth of the semiconductor crystal but for MHPs this modification is possible even after the crystal is grown. By combining the process, I developed for patterning MHP nanowires with this compositional process, we attain nanoscale control over MHP crystals, bringing them closer to parity with established semiconductors.

# List of Papers

## Publications included in this thesis

This thesis includes the following publications. In the text they are referred to by ‘paper X’ and their Roman numerals as listed here:

I. **Single vertical InP nanowire diodes with low ideality factors contacted in-array for high-resolution optoelectronics**

N. Lamers, K. Adham, L. Hrachowina, M.T. Borgström, and J. Wallentin

*Nanotechnology* **2025**, *36*, 07LT01

DOI: [10.1088/1361-6528/ad96c3](https://doi.org/10.1088/1361-6528/ad96c3)

I adapted and developed new processing for these devices and carried out all fabrications aside from NW growth which was carried out by K. Adham and L. Hrachowina. I collected and analysed all relevant data and was the main responsible for writing the manuscript.

II. **Deep Sub-Wavelength Imaging Using a Single Nanowire Detector**

N. Lamers, N. Anttu, K. Adham, L. Hrachowina, D. Hessman, M.T. Borgström, and J. Wallentin

*In manuscript*

I fabricated the devices, developed the measurement setup and procedure, and carried out the measurements and data analysis. I was the main responsible for writing the manuscript. Modelling was performed by Assoc. Prof. N. Anttu who also wrote the relevant parts of the manuscript.

III. **Free-standing Metal Halide Perovskite Nanowire Arrays with blue-green Heterostructures**

Z. Zhang, N. Lamers, C. Sun, I.G. Scheblykin, and J. Wallentin,

*Nano Letters* **2022**, 22 (7), 2941-2947

DOI: [10.1021/acs.nanolett.2c00137](https://doi.org/10.1021/acs.nanolett.2c00137)

I developed the anion exchange process and helped with the related processing. I helped with the electrical measurements and contributed to the discussion of the data.

IV. **Perovskite-Compatible Electron-Beam-Lithography Process Based on Nonpolar Solvents for Single-Nanowire Devices**

N. Lamers, Z. Zhang, and J. Wallentin,

*ACS Applied Nano Materials* **2022**, 5 (3), 3177-3182

DOI: [10.1021/acsanm.2c00188](https://doi.org/10.1021/acsanm.2c00188)

I developed the new process described in the paper and carried out all fabrication aside from NW growth which was carried out by Z. Zhang. I collected and analysed all relevant data and was main responsible for writing the manuscript.

V. **Gas-Phase Anion Exchange for Multisegment Heterostructured CsPb(Br<sub>1-x</sub>Cl<sub>x</sub>)<sub>3</sub> Perovskite Nanowires**

N. Lamers, Z. Zhang, I. G. Scheblykin, and J. Wallentin

*Adv. Optical Mater.* **2024**, 12, 2300435

DOI: [10.1002/adom.202300435](https://doi.org/10.1002/adom.202300435)

I developed the new process described in the paper and carried out all fabrication aside from NW growth which was carried out by Z. Zhang. I collected and analysed all relevant data and developed the diffusion model used in the paper. I was the main responsible for writing the manuscript.

VI. **Controlled Ligand-Free Growth of Free-Standing CsPbBr<sub>3</sub> Perovskite Nanowires**

Z. Huang, Z. Zhang, N. Lamers, D. Baranov, and J. Wallentin

*ACS Omega* **2024**, 9, 49, 48390–48396

DOI: [10.1021/acsomega.4c06646](https://doi.org/10.1021/acsomega.4c06646)

I helped in the development of the improved growth process and the discussion of the results.

**Publications not included in this thesis**

I contributed to the following publications during my PhD, but they are outside the scope of this thesis:

VII. **Single-Crystalline Perovskite Nanowire Arrays for Stable X-ray Scintillators with Micrometer Spatial Resolution**

Z. Zhang, H. Dierks, N. Lamers, C. Sun, K. Nováková, C. Hetherington, I. Scheblykin, and J. Wallentin

*ACS Applied Nano Materials* **2022**, 5(1), 881-889

DOI: [10.1021/acsanm.1c03575](https://doi.org/10.1021/acsanm.1c03575)

I contributed to the discussion and helped develop the scintillator growth.

VIII. **3D X-ray microscopy with a CsPbBr<sub>3</sub> nanowire scintillator**

H. Dierks, Z. Zhang, N. Lamers, and J. Wallentin

*Nano Res.* **2023**, 16, 1084–1089

DOI: [10.1007/s12274-022-4633-7](https://doi.org/10.1007/s12274-022-4633-7)

I contributed to the discussion of the data and worked on passivation for the scintillators.

IX. **Structural and chemical properties of anion exchanged CsPb(Br<sub>1-x</sub>Cl<sub>x</sub>)<sub>3</sub> heterostructured perovskite nanowires imaged by nanofocused x-rays**

L.A.B. Marçal, N. Lamers, S. Hammarberg, Z. Zhang, H. Chen, D. Dzighaev, M.A. Gomez-Gonzalez, J.E. Parker, A. Björling, A. Mikkelsen, and J. Wallentin

DOI: [10.1088/1361-6528/ad355c](https://doi.org/10.1088/1361-6528/ad355c)

*Nanotechnology* 2024, 35, 265710

I fabricated the samples for the experiment and helped in the discussion of the results.

X. **Nanoscale X-ray Imaging of Composition and Ferroelastic Domains in Heterostructured Perovskite Nanowires: Implications for Optoelectronic Devices**

S. Hammarberg, L.A.B. Marçal, N. Lamers, Z. Zhang, H. Chen, A. Björling, and J. Wallentin

*ACS Applied Nano Materials* **2023**, 6 (19), 17698-17705

DOI: [10.1021/acsanm.3c02978](https://doi.org/10.1021/acsanm.3c02978)

I fabricated the devices used in the experiment and carried out PL measurements. I contributed to the discussion of the results.

XI. **Ion Migration and Redox Reactions in Axial Heterojunction Metal Halide Perovskite CsPb(Br<sub>1-x</sub>Cl<sub>x</sub>)<sub>3</sub> Nanowire Devices revealed by Operando Nanofocused X-ray Photoelectron Spectroscopy**

Y.-P. Liu, N. Lamers, Z. Zhang, N. Zaiats, A. Mikkelsen, J. Wallentin, R. Dittmann, and R. Timm

*ACS Nano* **2024**, 18, 51, 34763–34775

DOI: [10.1021/acsnano.4c11458](https://doi.org/10.1021/acsnano.4c11458)

I fabricated the samples and provided PL measurements. I attended the beamtime and helped carry out the measurements. I contributed to the discussion of the results.

# Abbreviations

AAO	Anodised aluminium oxide
ALD	Atomic layer deposition
AlO <sub>x</sub>	Aluminium oxide
BCB	Benzo cyclobutene
CMP	Chemical mechanical polishing
CsPbBr <sub>3</sub>	Caesium lead bromide
CsPbCl <sub>3</sub>	Caesium lead chloride
DEZn	Diethyl zinc
DMF	Dimethylformamide
DMSO	Dimethyl sulphoxide
EBL	Electron beam lithography
EDS	Energy-dispersive spectroscopy
EL	Electroluminescence
EQE	External quantum efficiency
FA	Formadinium
FF	Fill factor
InP	Indium phosphide
IPA	Isopropyl alcohol
ITO	Indium tin oxide
LED	Light emitting diode
MA	Methylammonium
MHP	Metal-halide perovskite



MIBK	Methylisobutyl ketone
MOCVD	Metal-oxide chemical vapour deposition
NA	Numerical aperture
NW	nanowire
PECVD	Plasma-enhance chemical vapour deposition
PL	Photoluminescence
PMMA	poly(methyl methacrylate)
RIE	Reactive ion etching
SEM	Scanning electron microscopy
SiO <sub>x</sub>	Silicon oxide
SiN <sub>x</sub>	Silicon nitride
SRH	Shockley-Read-Hall
TEM	Transmission electron microscopy
TESn	Triethyl tin
TMAI	Trimethyl aluminium
TMIn	Trimethyl indium
TTBS	Tri(tert-butoxy) silanol
XRD	X-ray diffraction

# 1 Introduction

Modern optoelectronic devices are foundational to many everyday technologies we use to interact with the world. We use cameras to record our experiences, convey these experiences via optoelectronic telecommunication technologies to our fellow humans, and power all of this, in part, with energy harvested from sunlight via optoelectronics. As we strive to improve optoelectronic devices in all these areas, we look for ways to make devices for energy and space efficient, cheaper, and higher performing. An additional change to these devices that could offer improvements in all these characteristics is a move from thin-film devices towards using semiconductor nanowires (NW) as the active absorber and optical material.

Semiconductor NWs have been researched as active layers for electronic and optoelectronic applications for over two decades. Although definitions differ, NWs are generally classified as having a high aspect ratio such that they are significantly longer than they are wide, with the diameter typically being below 1  $\mu\text{m}$ . The NW geometry offers significant advantages for optoelectronic devices. Compositional variation can be introduced along the NW-axis to produce changing doping profiles or heterostructured NWs made from several different materials. Radial strain relaxation allows for the vertical integration of materials in NWs which in bulk would be too strongly strained due to lattice mismatch [1, 2]. The high surface-to-volume ratio of NWs allows for easy channel manipulation via gate-all-around approaches [3-6] and the anisotropic shape lends itself to light guiding [7-10]. Absorption in NWs can be enhanced by resonances related to NW diameter [11-13], as well as increasing NW length to match the absorption length of a given wavelength inside the NW material. NWs have therefore been used in applications like transistors [3-6, 14-18], light emitting diodes (LEDs) [19-23], photodetectors [24-35], lasers [36-39], and solar cells [40-43].

NWs can be made from different semiconductor materials using a variety of methods. For Si and III-V, NWs are mostly synthesised via chemical vapour deposition (CVD) (bottom-up) or etching methods (top-down), with the NWs standing vertically on a substrate. Metal-halide perovskite (MHP) NWs can also be synthesised via similar CVD methods [16, 44-49], but solvent-based synthesis is much more common and generally much more affordable. Solvent-based synthesis of MHP NWs and other

nanocrystals can be achieved via colloidal synthesis [50, 51] and solvent evaporation (recrystallisation) methods [52-54] or by using growth templates [55-58]. The latter is especially flexible, since it gives a large amount of control over crystal shape and orientation, as well as placement of the crystal on the substrate.

The focus of this thesis is the processing of both III-V NWs and MHP NWs into single NW devices, specifically InP NWs and CsPbBr<sub>3</sub> NWs. In both cases, these single NW devices and their associated processing are unique in their fields and allow for novel devices and measurements.

The work on InP NWs describes how to fabricate devices from single vertical (standing) NWs inside a NW array. Such devices have tremendous potential for display or detector applications with very small pixel size, where each NW in an array could form an individual pixel of small diameter and tight pitch. To accomplish this, processing must allow for alignment between NW growth and top-side contact, such that many different NWs can be contacted individually on the same chip.

To date, few reports exist which describe processing of single vertical NW devices [26, 35, 59, 60]. Largely, these existing reports circumvent this requirement for alignment between the contact layer and NW. One method is to grow NWs not in arrays but as “lone” NWs, removing the need for nanoscale alignment [35, 59]. Alternatively, NWs are grown in arrays, but the embedding isolation layer is removed only from a single NW, with contacting again using more macroscopic alignment techniques [60]. Neither of these approaches is conducive to contacting multiple single NWs within the same array.

A previous approach using EBL to pattern the top-contact layer forms the foundation of the work in this thesis [26]. However, several issues remained with the processing and sample design in the published form, including low device yield and low-quality diodes. The work put forth in this thesis improves the sample structure and processing, resulting in improved device performance and much higher processing yields. The resulting devices are demonstrated as single NW diodes, solar cells, and LEDs. Finally, imaging is performed using these single NWs as photodetectors for imaging of an optical focus at 70 nm spatial step size.

The work on CsPbBr<sub>3</sub> NWs focuses on developing lithography and processing methods to create horizontal single MHP NW devices. Although MHP nanocrystals are seeing widespread use in optoelectronic research devices with good results, little actual nanoscale processing of these devices is taking place. This is partially due to the high solubility of MHPs in polar solvents, which makes them incompatible with established nanoprocessing techniques [61-65]. A re-development of these methods is therefore necessary to find MHP-compatible versions of the techniques. Especially for NWs, an

electron-beam lithography (EBL) process is critical for depositing contacts in an aligned fashion. However, the importance goes far beyond this, as a nanoscale patterned polymer mask could also be used for dry etching, applying surface modifications, or other nanoscale processes. Similarly, not just NWs but all nanoscale MHPs and even thin films could benefit by the versatility of processing offered if an MHP-compatible lithography process was readily available.

Efforts have been made to re-develop lithography techniques with MHP-compatible solvents [61, 62, 65-67]. Specifically for EBL, the commonly used PMMA process has been modified by using dried solvents for use with the more stable MHPs like CsPbBr<sub>3</sub> [66]. Alternatively, the developer solution in the process has been replaced with a more MHP-compatible non-polar solvent solution [62]. The process put forward in this thesis replaces the developer solution with non-polar solvents, which mimic the performance of the established PMMA EBL process almost identically. The contacts fabricated via this process are more highly structured and thicker than those produced using any previously reported MHP-compatible EBL processes.

A second processing technique missing from MHPs is the creation of nanoscale heterostructures, which are critical for optoelectronic devices like LEDs where they serve as the emissive layer [68]. Although heterostructured MHP NWs can be grown directly by some techniques [45], a more universal approach uses a post-growth modification effect known as anion exchange [69]. This allows for the conversion of the halide anion of an MHP to a different halide species, e.g. CsPbBr<sub>3</sub> to CsPbCl<sub>3</sub>. We study two gas-based anion exchange processes for conversion of CsPbBr<sub>3</sub> to CsPb(Br<sub>1-x</sub>Cl<sub>x</sub>)<sub>3</sub> in this thesis. Lastly, we combine this process with the EBL patterning process to create heterostructured NWs, demonstrating that nanoscale composition modification and contact patterning are possible, which may enable new and novel MHP devices structured at the nanoscale.

The thesis is structured as follows: Chapter 2 introduces the relevant semiconductor background shared between both InP and CsPbBr<sub>3</sub> materials. Chapter 3 deals with the vertical single InP NW devices, describing fabrication, characterisation, and their use as ultra-high-resolution photodetectors in imaging a laser focus. Chapter 4 describes my work with the CsPbBr<sub>3</sub> NW devices, delving into the challenges faced when processing these materials, how we can overcome these challenges to fabricate single CsPbBr<sub>3</sub> NW devices via EBL, and how we can further process these NWs via anion exchange to create heterostructured NWs.

# 2 Semiconductors

In this chapter I will give an overview of the basic semiconductor physics relevant to the single NW devices discussed later in the thesis. I will discuss diodes and *pn*-junctions which are the fundamental building blocks of modern optoelectronics. Although this section is currently mostly relevant to the InP NWs, the processing methods described later for MHP NWs are potential pathways for also achieving *pn*-junctions and diodes within MHPs. I will also discuss the optoelectronic effects relevant to both InP and CsPbBr<sub>3</sub> NWs.

## 2.1 *pn*-junctions and diodes

The combination of many atoms in a crystal lattice gives rise to the appearance of a distribution of states with energies  $E$  and crystal momentum  $k$  that electrons and holes, positively charged electron vacancies, are allowed to occupy [70, 71]. Likewise, forbidden states exist which cannot be occupied and thus divide energy-momentum space into energy bands. The probability of finding a certain state occupied is given by the Fermi-Dirac distribution with a 50% probability of finding an occupied state at a Fermi level  $E_F$ . The lowest not fully occupied band is called the conduction band, and the highest fully occupied band is called the valence band. The energy difference between the bottom state of the conduction band and top state of the valence band is called the band gap with energy  $E_G$ . If these states are located at the same crystal momentum  $k$ , we refer to this as a direct band gap and a direct optical transition between them is possible. Otherwise, it is an indirect band gap and an electron transitioning between these states must either gain or lose sufficient crystal momentum by interaction with phonons to be able to transition between these states.

The movement of electrons, current, requires both available electrons and available unoccupied states. Therefore, the position of the energy bands relative to the Fermi level and the resulting occupation levels of valence and conduction bands dictate the conductivity of a material. Semiconductors have traditionally been defined as having a conductivity or band gap between that of metals and insulators, with ranges of

$10^2 \text{ } \Omega\text{cm} - 10^9 \text{ } \Omega\text{cm}$  and  $0 \text{ eV} - 4 \text{ eV}$  given, respectively [72]. This definition increasingly runs into exceptions where materials such as gallium nitride (GaN) and diamond are used for semiconductor applications but would be classified as insulators via these definitions. A better definition may therefore be that semiconductors are materials where the conductivity, electronic properties, and underlying band structure can be meaningfully altered and controlled by means such as composition.

An intrinsic semiconductor is not very conductive, since there are few electrons in the conduction band and the valence band is completely filled and contains few holes. This only allows very few carriers to move and conduct current. We can alter this picture by introducing atomic impurities into the crystal in a process called doping as illustrated in Figure 2.1. Taking the InP crystal as an example we see that each In atom binds to three P atoms and vice versa. If a Zn impurity is introduced, it replaces an In atom in the lattice but only has sufficient valence electrons itself to covalently bind to two neighbouring P atoms. This creates an electron vacancy called an acceptor state just above the valence band edge which can be occupied by valence band electrons resulting in an increase of holes in the valence band. This in turn increases conductivity and is called *p*-doping. Similarly, we can increase the number of mobile conduction band electrons by replacing an In atom with an atom like Sn which has one more valence electron than In. This excess electron is not involved in the covalent bonding of the crystal. It occupies a donor level state just under the conduction band edge. Thus, these electrons are easily promoted to the conduction band where they increase conductivity via *n*-doping.

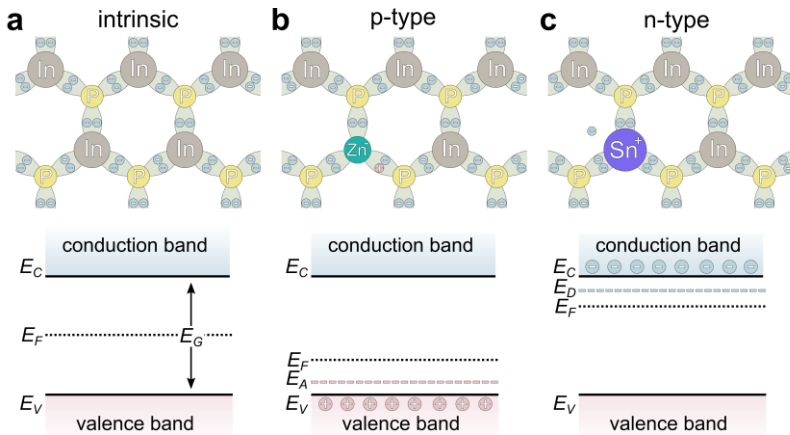


**Figure 2.1 Illustration of doping and its effect on crystal and band structure**

**a-c** The crystal structure and band diagram for intrinsic, *p*-doped, and *n*-doped InP, respectively. The *p*- and *n*-doped crystals include Zn and Sn doping atoms, respectively. This moves the Fermi level relative to the band gap centre, increasing the number of available holes for *p*-type and electrons for *n*-type doping.



The higher conductivity of doped semiconductors on their own is already advantageous since it allows for the formation of ohmic contacts to these materials. A lot of additional functionality emerges when we combine a  $p$ -doped and  $n$ -doped material to form a  $pn$ -junction.

When a  $p$ -doped and  $n$ -doped material are in contact the imbalance of charge carriers drives a diffusion current. The holes from the  $p$ -doped side diffuse into the  $n$ -doped material and vice versa for the electrons. As these charge carriers meet, they recombine. This results in a depletion region  $W$  without free charge carriers. At the same time, the ionised acceptor and donor atoms within this depletion region cannot move themselves since they are bonded into the crystal lattice. As a result, an electric field spans this depletion region, often called a built-in electric field. By constructing a  $pin$ -junction with an intrinsic central segment, the width of the depletion region can be expanded.

Looking at the band diagram across a  $pn$ -junction as shown in Figure 2.2, we see that the conduction and valence bands are shifted relative to each other by this built-in potential. Equal but opposite diffusion and drift currents flow across the unbiased  $pn$ -junction. The diffusion current is driven by the imbalance of charge carriers due to the different doping, whereas the drift current is driven by the built-in electric field. When the  $pn$ -junction is biased, the external electric field can either be aligned with or against the built-in field resulting in asymmetrical current-voltage characteristics. When the external field reinforces the built-in field, the number of carriers with sufficient energy for diffusion is reduced as the bands become more strongly offset between the  $p$ - and  $n$ -doped regions. This results in a net current driven by drift and is called reverse biasing. If instead we apply an external electric field so that it opposes the built-in field, we can cancel it out or oppose it sufficiently that a large diffusion current can flow across it as the conduction band energies of the  $p$ - and  $n$ -regions align. At the same time, the drift current is reduced due to the lowered electric field. This is called the forward bias regime.

Mathematically, the current density through an ideal  $pn$ -junction is given by the Shockley diode equation [73] as

$$J = J_0 \left[ e^{\frac{V}{nV_T}} - 1 \right] \quad (2.1)$$

With a dark saturation current density  $J_0$ , a bias voltage  $V$ , the thermal voltage  $V_T = q/k_B T$ , and an ideality factor  $n$ . For a perfectly ideal diode  $n = 1$  and diffusion currents are dominating the device in forward direction. However, for direct-bandgap diodes with both electron and hole carriers, recombination plays a significant role and leads to an increase of the ideality factor up to  $n = 1-2$  [74]. Higher values of  $n$  indicate that

there are other mechanisms reducing the current and available carriers, such as traps which significantly increase recombination.

It should be clear from the above that controlling local charge carrier concentrations and band structures via doping is a critical part of semiconductor fabrication. However, while the doping of materials such as III-Vs and Si is nowadays trivial, doping of MHP materials is much more difficult and currently still poorly understood [75]. Doping as illustrated in Figure 2.1 is applicable to III-Vs and Si, which are covalently bonded crystals, but not to MHPs which have a more ionic crystal character for which a cohesive understanding of electrical doping is yet to be developed.

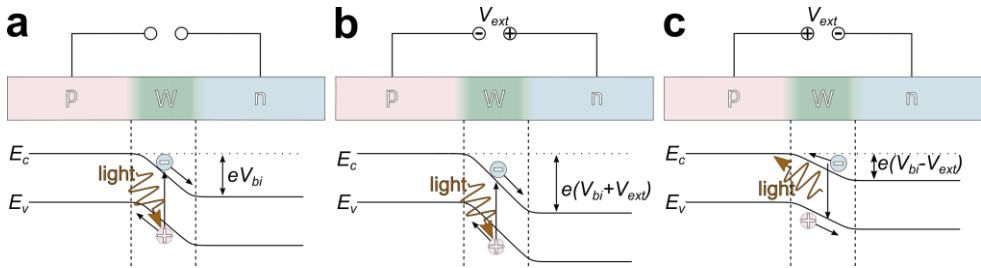


**Figure 2.2 Schematic of a pin-junction under bias and associated band diagrams**

**a-c** Schematics and band diagrams of unbiased, reverse biased, and forward biased *pin*-junctions, respectively. **a-b** Carrier separation occurs via the built-in or built-in + external electric field after light absorption. **c** Electroluminescence after carrier recombination in the depletion region.

## 2.2 Optoelectronics

### 2.2.1 Photocurrent and solar cells

If we take a semiconductor and shine light on it, the incident photons can be absorbed by electrons in the semiconductor provided they have more energy than the band gap. This promotes the electron into the conduction band, yielding an electron-hole pair. Just as with doping this increases the number of carriers in the device, making it more conductive. If we are biasing the semiconductor we can measure a photocurrent and correlate this photocurrent to the incident optical power, giving us a very basic photodetector.

However, it is not desirable to input energy into the system to harvest the carriers. Instead, the built-in field inside a *pn*- or *pin*-junction can separate the carriers for us. Generally, each photon of optical light above the band gap energy  $E_G$ , absorbed inside the depletion region will create a single electron-hole pair which is then separated by

the built-in field yielding a photocurrent  $I_{ph}$  as illustrated in Figure 2.2a-b. The incoming photon flux  $\Phi$  is then proportional to the photocurrent  $I_{ph} \propto \phi^\alpha$  with  $\alpha = 1$  for the ideal case [68].

If we take this photocurrent, we can modify the ideal diode equation of Eq. 2.1 to that of the solar cell such that

$$J = J_0 \left[ e^{\frac{V}{nV_T}} - 1 \right] - J_{ph} \quad (2.3)$$

Under illumination but with no bias, we therefore observe a short-circuit current  $J_{sc} = J_{ph}$  which increases with increasing illumination. A bias voltage  $V_{oc}$  exists such that  $J = 0$ , which is called the open-circuit voltage. A key figure of merit for solar cells is the fill factor (FF), which describes how close the real output power  $P_{mpp}$  is to the theoretical maximum output power given by the product of  $I_{sc}$  and  $V_{oc}$ .

$$FF = \frac{P_{mpp}}{I_{sc}V_{oc}} \quad (2.4)$$

### 2.2.2 Carrier recombination

Ideally, all photoexcited carriers would contribute to the photocurrent. In practice the carriers recombine based on the carrier lifetime in the material. This recombination reduces the charge carrier collection efficiency  $\eta_{CCE}$  which describes which portion of generated carriers is collected at the contacts. The percentage of carriers seen as current at the contacts versus that expected from excitation itself is called the external quantum efficiency (EQE) and is an important figure of merit, which depends not just on  $\eta_{CCE}$  but also on the absorption efficiency. Notably, EQE for solar cells is usually spectrally dependent.

$$EQE = \frac{I_{ph}}{q\phi} \quad (2.5)$$

With elementary charge  $q$ . Similarly, we can define a power efficiency  $\eta = P_{in} / P_{out}$ .

The three main recombination mechanisms are radiative recombination, Shockley-Read-Hall (SRH) recombination, and Auger recombination. During radiative recombination an electron from the conduction band combines directly with a hole in the valence band while emitting the excess energy, generally similar to the band gap energy, as a photon. In SRH recombination, the electron instead recombines with the hole via trap states located inside the band gap [76, 77]. In Auger recombination, the excess energy of the valence band electron is not emitted via a photon but is instead passed onto a second (Auger) electron, which in turn loses the energy via thermalisation as phonon emission.

Both SRH and Auger recombination are generally non-radiative. To maximise the photocurrents and efficiencies of our devices, we therefore want to reduce all non-radiative recombination pathways. Therefore, passivation of semiconductors is an important processing step taken in order to reduce surface states that contribute to SRH combination. At the same time, radiative recombination is a useful mechanism that we can make use of in luminescence applications or for photon recycling in solar cells [78].

### 2.2.3 Photo- and electroluminescence

Both photo- and electroluminescence (EL) are two ways to make use of radiative recombination for characterisation. In photoluminescence (PL) measurements, we use light of energy greater than the band gap to create photocarriers. When these excited photocarriers recombine radiatively, we can then measure the light which is emitted. This lets us determine a material's band gap based on the emitted wavelengths and can also provide insights into the carrier lifetime when performed as time-resolved PL.

EL is the working mechanism behind LEDs. Here, we inject carriers into a  $pn$ -junction by biasing it in forward direction as illustrated in Figure 2.2c. The injected charge carriers recombine in the active region and the emitted light can be used for illumination. Just as during PL, the light emitted during EL is of a wavelength corresponding to recombining states, typically the band gap. Spectroscopy of the emitted light can therefore also reveal information about the material. As with photodetection, EQE is also a valid figure of merit for these devices, given as the fraction of emitted photon flux  $\phi_{out}$  versus injected current  $I_{inj}$ .

$$EQE = \frac{q \phi_{out}}{I_{inj}} \quad (2.6)$$

### 3 Vertical single InP nanowire devices

Devices utilising single vertical NWs as individual pixels would allow for high-resolution display and detector applications. Pixel sizes in current optical sensors are generally of the order  $1\text{ }\mu\text{m}$  to  $2\text{ }\mu\text{m}$  [79, 80], much larger than NW diameters or even NW-to-NW spacing achievable within NW arrays. In practice, the spatial resolution of a detector or display is not exclusively limited by the absorber or emitter elements but also affected by circuit elements such as access transistors or storage capacitors that together form an independent pixel [81]. Additionally, as pixel size decreases, the sensitivity of the absorber material must increase so that a good read-out signal can be obtained [79, 80, 82]. This raises the question of how small we can make our optoelectronic devices and what sort of limitations arise when our detector is significantly smaller than the wavelength of light? NW-shaped detectors offer a great starting point for such an investigation, since they have a small transversal pixel size but a length that can be increased for optimal absorption.

The requirement for a sensor based on single NW pixels is that the NWs are grown inside a NW array or grid but are then contacted individually via patterned contacts. Only a few reports describing vertical single NW devices are currently published [26, 35, 59, 60]. In both *Farrell et. al.* and *Krogstrup et. al.*, vertical single NW devices were processed, but not in a fashion that satisfies the requirements above. In both cases, the single NW device was accomplished by simply growing a lone NW before depositing a larger area contact [35, 59]. In *Li et. al.*, the authors took a different approach [60]. They grow NWs in an array and embed them in polymer. The tips of individual NWs were then revealed from the polymer via focused-ion-beam etching, and a contact was evaporated. In both approaches, no effort was made to specifically pattern the contact or to make the processing suitable to be upscaled for fabrication of multiple single NW pixels. In contrast, the process put forward by *Chayanun et. al.*, which was developed by a previous member of our research group, uses EBL to pattern contacts to the tips of individual NWs [26].

However, problems remain even with this processing. The resulting single NW devices are poor diodes with ideality factors of  $n = 14$ . This is in stark contrast to the ideality factors of  $n = 2.6$  and even  $n = 1$  reported by *Krogstrup et. al.* and *Farrell et. al.*,

respectively. Issues also remain with the device yield and overall sample structure, which utilised a photoresist isolation layer and only a 30 nm thin  $\text{SiN}_x$  insulation layer to insulate the top and bottom contacts. Despite this, the single NW devices showed great performance for ultra-high-resolution imaging.

The work put forward in this chapter demonstrates a refined process for creating single vertical NW devices by aligning the top-side contacts directly to the grown NWs. In the first part, the processing is developed and two isolation layer materials, benzo cyclobutene (BCB) and  $\text{SiO}_2$ , are compared. The resulting devices are then characterised as single NW diodes, solar cells, and LEDs.

Finally, an 80 nm diameter single NW device is utilised as an optical detector for imaging of an optical focus with a step size of 70 nm. Both the step size and NW diameter are significantly smaller than the 633 nm wavelength of the laser light used to form the focus. We find that the detector shows a good linear photoresponse over many orders of magnitude and can be readily used for imaging, revealing detail in the recorded intensity distributions that would be difficult to measure with any other method.

### 3.1 Fabrication

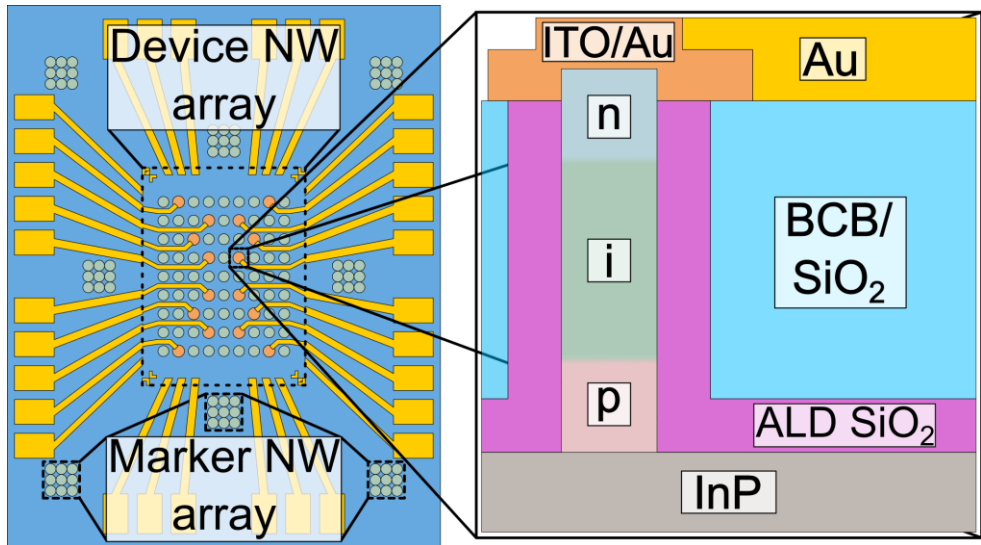


**Figure 3.1 Schematic of sample layout and device structure cross-section**

Left side shows a top view of the finished chip with a central array of device NWs and finished bond pads plus traces. Right side shows a cross-section view of finished vertical single NW device.

The structure of the entire sample and a finished single NW device are shown in Figure 3.1. Our goal is to contact single NWs located inside an array at the centre of our substrate. The backside contact will be provided by the substrate itself, but the top side contact must be patterned to individual NWs in order to complete the circuit. I will now give a condensed overview of the processing.

### 3.1.1 NW seed particles

To begin fabrication, we pattern Au seed particles for the MOVPE growth onto a p-type InP (111)B substrate via EBL. Holes of 50 nm to 70 nm diameters are patterned in a 2  $\mu\text{m}$  by 4  $\mu\text{m}$  array and 20 nm of Au are deposited, as illustrated in Figure 3.2a-b. We place dense arrays of dots and area structures around the sample as alignment marks which will also grow into NWs, making them easily visible in future EBL steps. Due to the e-beam focus quality and resist thickness varying slightly for each sample, we obtain a slight variation of seed diameters across different samples.

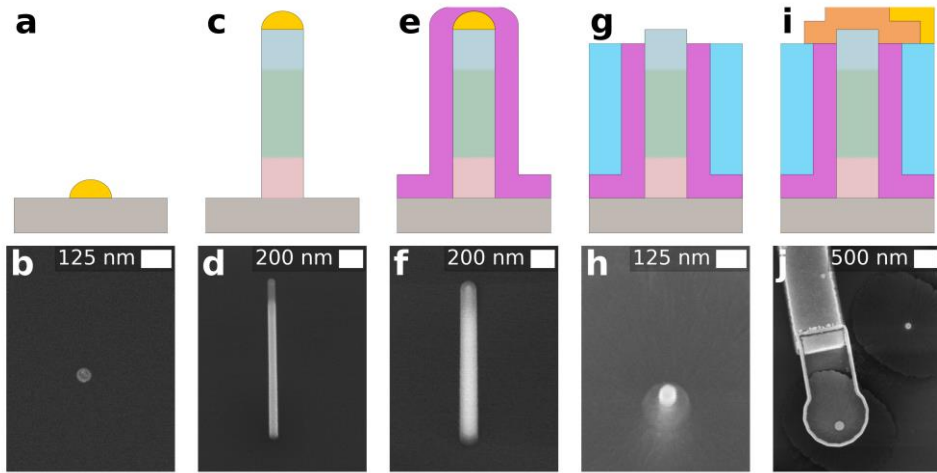


**Figure 3.2 Schematics and SEM images of nanowire device throughout processing**

**a-b** Top view of Au seed particle. **c-d** As-grown NW with SEM image taken at 30° tilt. The top *n*-section is visible from the SEM contrast. **e-f** NW after ALD, SEM image taken at 30° tilt. **g-h** NW after isolation layer deposition, CMP polishing, and RIE etching with NW tip revealed, imaged at 30° tilt. **i-j** Top view of finished single NW device with ITO top contact.

### 3.1.2 Nanowire growth

NWs are grown from the Au seed particles via the VLS growth mechanism in an MOVPE reactor [83, 84]. All InP NWs in this thesis were grown by L. Hrachowina and K. Adham in Prof. M.T. Borgström's group at Lund University. The previously

deposited Au seed particles act as catalysts during the growth, forming NWs underneath themselves. Trimethyl indium (TMIn) and phosphine ( $\text{PH}_3$ ) were used as the source gases for In and P. To create a *pin*-doping profile, dopants are introduced during the growth. Diethyl zinc (DEZn) and tetraethyl tin (TESn) are used as the *p*- and *n*-dopants, respectively. A small amount of DEZn is also used during the *i*-segment growth to compensate for the inherent *n*-type behaviour of undoped InP [85, 86]. As-grown NWs are shown in Figure 3.2c-d and vary in length between 2.0  $\mu\text{m}$  and 2.5  $\mu\text{m}$ , corresponding to the variation of the seed particle diameter.

### 3.1.3 Insulation layer

Next, we deposit an insulation layer to encapsulate the NWs and insulate them electrically. We grow a layer 20 nm of  $\text{SiO}_x$  via ALD to encapsulate the NWs as shown in Figure 3.2e-f. Since we use trimethyl aluminium (TMAl), tri(tert-butoxy) silanol (TTBS), and water as the precursors, the layer also contains some  $\text{AlO}_x$  [87]. This layer also provides a rudimentary level of passivation [88].

### 3.1.4 Isolation layer

As a next step, we need to create an isolation layer which will protect the NWs and allows us to deposit top-side contacts to the NW tips. We want this layer to be chemically and mechanically stable, a good dielectric, and optically transparent. Additionally, the layer is structurally important since it supports the bond pads which we use to integrate the device into chip holders. We investigated both benzo cyclobutene (BCB) polymer (Cyclotene 3000 series) and  $\text{SiO}_2$  deposited via PECVD for this purpose.

#### *Benzo cyclobutene isolation layer*

By choosing the correct combination of Cyclotene formulation and spin speed, we spin coat a layer of BCB that is 500 nm to 1  $\mu\text{m}$  thicker than the NWs. The BCB is first soft baked on a hot plate and then hard cured in an RTP system. Afterwards, RIE is used to back etch the BCB and reveal the NW tips. The ALD passivation layer around the NW tip is then removed with HF followed by removing the Au dot with Au etchant.

#### *PECVD $\text{SiO}_2$ isolation layer*

The processing of the PECVD  $\text{SiO}_2$  is more complicated. We grow the  $\text{SiO}_2$  from  $\text{SiH}_4$  and  $\text{N}_2\text{O}$  at 100 °C. As with the BCB, we overgrow the PECVD  $\text{SiO}_2$  to a thickness



around 1  $\mu\text{m}$  thicker than the NWs are long. Even with this much excess thickness above the NW tips, the PECVD oxide leaves a bumpy surface as shown in Figure 3.3a. Each bump on the surface corresponds to a NW underneath. To remove these bumps, we use chemical mechanical polishing (CMP). During CMP, the sample is fixed into a holder and pushed onto a rotating sanding surface onto which a polishing solution containing silica nanoparticles is dispensed. While this step appears very macroscopic, it allows gradual removal of material at very slow and controllable rates. A problem that arises during this process is that the bumps on the sample surface are not very stable when pressed onto the rotating polishing plate. The resulting shear forces can often tear out the bumps alongside the NW within, as shown in Figure 3.3b. To prevent this, we spin coat an additional PMMA layer first. This layer embeds the bumps and provides a smoother surface as shown in Figure 3.3c. We can then polish this sample until we obtain a flat surface as seen in Figure 3.3d. Just as with the BCB layer, we can then back etch with RIE removing both the PECVD and ALD  $\text{SiO}_2$  layers in a single step. The Au seed particle is then removed with gold etchant. This results in a NW protruding from the PECVD layer as shown in Figure 3.2g-h.

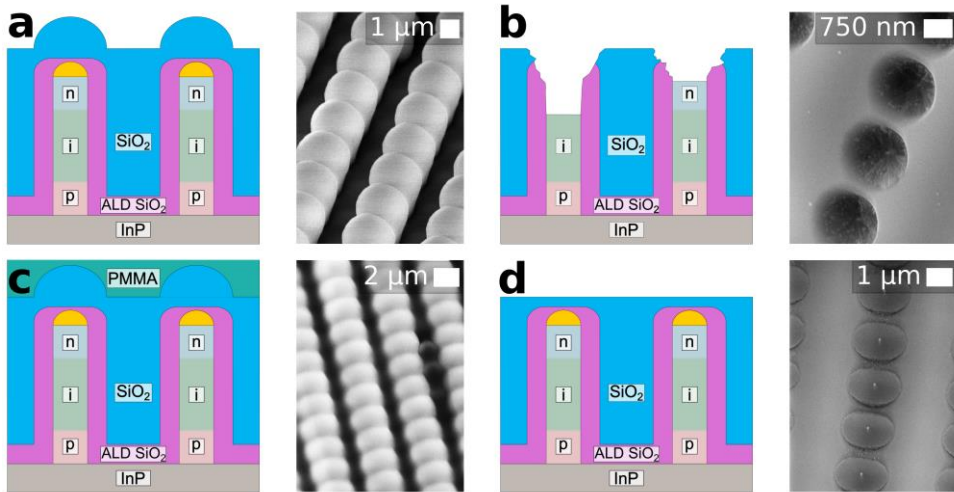


**Figure 3.3 PECVD layer planarisation process**

**a-d** Schematics and SEM images at 30° tilt of PECVD layer throughout planarisation processing. **a** PECVD cones after deposition. **b** PECVD surface with tear out of cones and NWs after polishing without polymer encapsulation. **c** PECVD cones encapsulated in PMMA. **d** Flat PECVD surface with visible NWs after polishing.

### 3.1.5 Top contacts

With a flat surface and the NW tips protruding from it, we now pattern contacts to individual NWs. To align the top contacts, we rely on the NWs which were grown

around the sample as markers. The tips of these NWs protrude from the isolation layer just like the device NWs and are therefore visible in EBL. We can combine several EBL and UV lithography steps to deposit new sets of markers, contact pads, and contact traces to individual NWs. For the materials of the contact cap just above the NW we use both transparent indium tin oxide (ITO) and gold contacts, resulting in completed single NW devices as shown in Figure 3.2i-j.

### 3.1.6 BCB and PECVD SiO<sub>2</sub> – a comparison

The choice of isolation layer has a significant impact on the device quality. While the impact on individual NW characteristics is discussed below, there are two significant impacts on device fabrication.

Firstly, integration of the chips into chip carriers is significantly affected. Wire bonding is a necessity to establish a contact between the bond pads on the chip and those on the chip carrier. While PECVD samples are trivial to bond with wedge bonding, the same is not true of the BCB samples. Due to the low adhesion of the metal layers to the BCB surface, both wedge bonding and the much gentler ball bonding end up stripping the contact pads off the sample surface, damaging the contact pad permanently.

Secondly, device yield is significantly different between the two isolation layers. The BCB isolation layer results in many unexplained device failures where devices which appear properly contacted in the SEM show no electrical response. This failure rate is around 40%. Combined with the low wire bonding yield, this makes it very difficult to obtain wire-bonded devices on BCB-based samples. A more detailed discussion of both these effects is found in paper I.

## 3.2 Characterisation

Before we use our newly fabricated devices for any application, we want to get an understanding of the device quality and parameters. Given the different device configurations, we also want to know what the effect of the isolation layer and contact material is. We therefore characterised them electrically, as diodes, solar cells, and light emitters.

### 3.2.1 Single nanowire diode

As a first step in electrical characterisation, we measured the current-voltage response of individual NWs in the dark, as shown in Figure 3.4a. For the best devices, there is little difference based on the choice of isolation layer or top contact material, with ideality factors close to  $n = 2$  for all configurations. However, when we look at the average device, we can find a stark difference. For BCB/Au and BCB/ITO devices, we find  $n = 5.0 \pm 2.9$  (sample size of 8 devices,) and  $n = 3.3 \pm 1.1$  (sample size of 16 devices), respectively. These values are much higher and less consistent than that of the average  $\text{SiO}_2/\text{ITO}$  device at  $n = 1.8 \pm 0.5$  (sample size of 13 devices). Even though the passivation layer is shared across BCB and PECVD  $\text{SiO}_2$  samples, this difference in ideality factors indicates a difference in carrier and recombination dynamics in the device. From theory, we expect  $n = 2$  for InP devices, due to the participation of both holes and electrons in the conduction [70], although  $n = 1$  has been demonstrated for III-V NWs [35]. However, the high value of  $n = 5$  for BCB devices indicates additional recombination mechanisms, which are non-desirable. This could be due to strain introduced by the curing of the BCB layer. It is clear therefore that the BCB isolation layer is not the best choice for diode performance, in addition to the previously mentioned processing challenges.

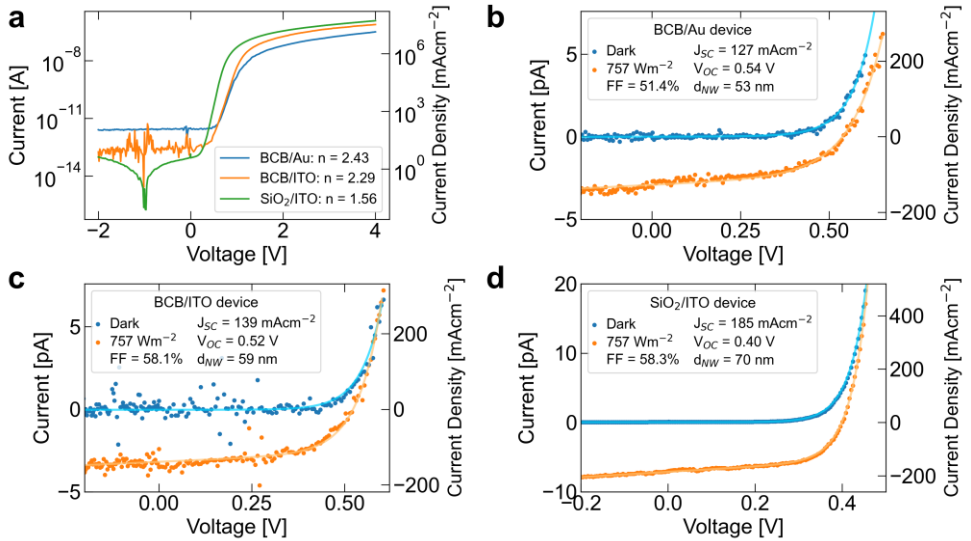


**Figure 3.4** Current-voltage and solar cell characteristics of single nanowire solar cells with different device architectures

**a** Current-voltage curves of three exemplary BCB/Au, BCB/ITO, and  $\text{SiO}_2/\text{ITO}$  devices, measured in the dark. The fitted diode ideality factors  $n$  are also shown. **b-d** Solar cell measurements of BCB/Au, BCB/ITO, and  $\text{SiO}_2/\text{ITO}$  devices shown in **a**. The figures-of-merit for the individual solar cells and fitted diode curves are also shown. Reproduced from paper I.

### 3.2.2 Single nanowire solar cell

We next characterised the single NWs as solar cells using a solar simulator with an excitation intensity of  $757 \text{ Wm}^{-2}$  (0.7 suns, AM1.5G spectrum), as shown in Figure 3.4b-d. The figures of merit obtained for the different device architectures are summarised in Table 3.1. We can see that the average  $V_{oc}$  is higher for the BCB-based devices, corresponding to the later turn on and poorer ideality factors. At the same time, the short-circuit current densities  $J_{sc}$  are similar regardless of architecture. This translates into higher fill factors for the BCB-based devices, causing them to have better figures-of-merit for solar cell performance. Curiously, there is no advantage to the transparent top contact, when one would intuitively expect that the Au metal cap would shadow the underlying NW. However, this has no significant effect because the absorption area of the NW far exceeds its geometrical cross-section. This is because the NWs act like antennae, where the incoming light can be coupled into resonant modes within the NWs through the sidewalls and subsequently absorbed [11, 41, 43, 59, 60, 89]. It is this effect that also leads to apparent power conversion efficiencies of  $\eta_{\text{BCB/Au}} = 49.7\%$ ,  $\eta_{\text{ITO/Au}} = 55.8\%$ , and  $\eta_{\text{SiO}_2/\text{ITO}} = 60.8\%$ . All of these are far beyond the Shockley-Queisser limit of 33.7% [90] but this is merely an artefact of using the geometrical cross-section for both absorbed power and current density calculations.

**Table 3.1 Average figures-of-merit for single nanowire solar cells of different architectures**  
Current density is calculated from the geometrical cross-section of the NWs. Averages are taken for 8 devices for BCB/Au, 16 devices for BCB/ITO, and 13 devices for SiO<sub>2</sub>/ITO. The standard deviation is also given for  $J_{sc}$ .

Device architecture Isolation layer / top contact	$V_{oc}$ [V]	$J_{sc}$ [mAcm <sup>-2</sup> ]	FF [%]
BCB/Au	0.56	$104 \pm 34$	57.9
BCB/ITO	0.57	$81 \pm 57$	58.3
SiO <sub>2</sub> /ITO	0.37	$97 \pm 57$	49.4

### 3.2.3 Single nanowire LED

Lastly, we characterised the NWs as single NW LEDs. Due to the wire bonding issues with BCB samples, this was limited to devices with PECVD SiO<sub>2</sub> isolation layers. Emission from the NW LED was observed at biases as low as 2 V, but discernible spectra required at least 2.5 V. This corresponds to current densities of  $1 \times 10^7 \text{ mAcm}^{-2}$  as shown in Figure 3.5a. We measured the emission up to current densities of  $4 \times 10^8 \text{ mAcm}^{-2}$ , corresponding to 15.4  $\mu\text{A}$  through a single NW. Despite these high current densities, we saw no degradation in performance even for sustained periods. The emission spectra can be found in Figure 3.5b. At low biases and currents, only two peaks are observed: one at 1.37 eV (907 nm) and another at 1.55 eV (800 nm). At higher biases an additional third peak emerges at 1.74 eV (710 nm).

The 1.37 eV (907 nm) peak is associated with the InP band gap, which lies at 1.34 eV (922 nm) for zincblende InP and 1.40 eV – 1.42 eV for wurtzite InP [91-96]. Since the NWs crystallise as a mixture of zincblende and wurtzite crystals the core emission lies in the range between that of the pure zincblende and wurtzite crystals. The additional two peaks are not associated with any distinct transitions from tabulated values but are likely the result of band filling and transitions to split-off bands.

In terms of emission efficiency, we find that the EQE is very low and peaks at  $1.5 \times 10^{-6} \%$ . These values are calculated based on the NW tip being a point emission source without considering emission perpendicular to the NW axis. We see two regimes, where the EQE rises initially before stabilising at this value. This can also be seen in the emission power which follows two separate power laws with  $P_{opt} \propto I_{inj}^{2.67}$  for lower biases and  $P_{opt} \propto I_{inj}^{1.03}$  for high biases, indicating a change in recombination dynamics with increasing carrier injection.

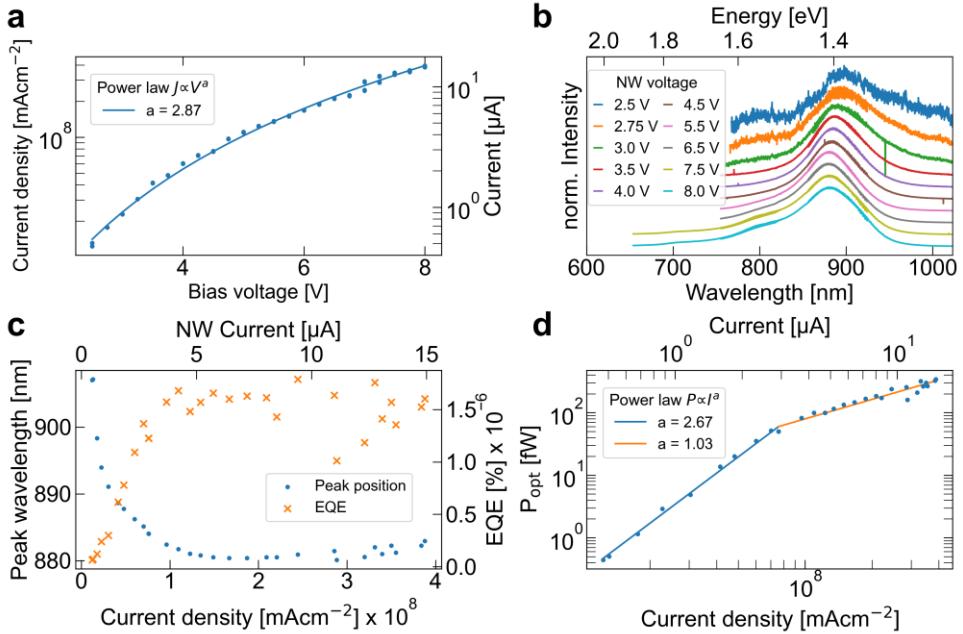


**Figure 3.5 Characterisation of a single nanowire as an LED**

**a** Current density – voltage curve for high forward bias as well as power law fit  $J \propto V^a$ . **b** Normalised and offset emission spectra of single NW LED at selected bias levels. **c** Peak emission wavelength and EQE evolution with increasing current density. **d** Optical emission power versus current density, showing two distinct regimes which follow power laws  $P \propto I^a$  with  $a$  decreasing from  $a = 1.03$  to  $a = 2.67$ . Reproduced from paper I.

### 3.3 Sub-wavelength imaging using a single nanowire detector

As is one of the primary uses of larger photodiode arrays, we can also use our single NW photodetector for imaging. However, while the previous generation of these devices was used for X-ray imaging [26], we instead make use of the transparent ITO top contact and use the devices to image an optical focus.

The imaging of optical foci is a well-studied field because ever since the invention of the laser, the applications for highly focused optical fields have only grown. They are used widely in industrial applications such as laser cutting or direct laser writing, and in analytical applications like super-resolution microscopy. Lithography also often makes use of intensity distributions with very spatially dense intensity variations, as is the case in displacement Talbot lithography and modern super-resolution lithography methods [97]. Commercially available photodiode arrays typically have pixels sizes on the order of micrometres, far too large to image intensity distributions which approach the diffraction limit of optical or shorter wavelength light [79, 80]. NW-shaped pixels could be a great alternative for these applications, because they can be transversally small but with a length that matches the absorption length of the relevant light.

Popular methods for imaging the focal spot of such beams include scanning probes or knife-edges [98-110]. Knife-edge methods record the increase in intensity as the knife edge passes through the focal plane, which allows the shape of the focal spot to be reconstructed. Scanning probe methods instead use either a small reflective particle to image the reflected light or a sharpened optical fibre to collect light from the focal plane measure it via a photodetector. It is notable that none of these methods directly record the intensity but instead record scattered or propagated intensities.

Although scanning photocurrent measurements of single NW devices have been carried out, this was not done to characterise the optical beam but instead to characterise the optical absorption of the NW devices [59, 60]. We instead used our single NW photodetectors for imaging the focal spot by scanning them in planes along the optical axis and recording the photocurrent. Since the physical pixel size is far smaller than the wavelength of visible light we can record images with an ultra-small step size also below the wavelength. The results demonstrate the good photodetector properties of our NWs and show that even though physical pixel sizes can be reduced far below the wavelength, an increase in resolution does not necessarily follow.

### 3.3.1 Setup

The experimental setup used to realise these measurements consists of three parts: an electrical part, a high-resolution stage, and an optical part.

For the electrical part, the NW devices with SiO<sub>2</sub> insulation layer are wire-bonded to chip carriers and integrated into printed circuit boards. A femtoammeter is then used to measure the current through the devices or to record current-voltage curves .

For staging, a tomography stage with five linear stick-slip actuators is used [111]. Two are aligned in the  $z$ -axis, two in the  $x$ -axis, and one in the  $y$ -axis. The  $z$ -axis of the system is aligned along the optical axis. The linear stages provide ample driving range of up to 10 mm with accuracies around 1 – 10 nm.

The optical setup consists of a fibre-coupled diode laser at 633 nm wavelength. The fibre is fed into an off-axis reflective collimator. The collimated beam is, in turn, incident either directly on the sample or focused via a 0.8 numerical aperture (NA) objective.

### 3.3.2 Calibration of photoresponse

First, we want to understand the relationship between photocurrent and incident light intensity. We therefore alter the current through the laser diode to produce different light powers and record a scanning photocurrent image with the NW device for each of these power settings. Based on the known optical power and the measured photocurrent spot, we can calculate the average photocurrent yielded by each light intensity, as shown for one device in Figure 3.6a.

We find that the lower detection limit lies at 0.5 suns, below which it becomes difficult to distinguish the photocurrent from background noise. By fitting a linear power law  $I_{ph} \propto \phi^\alpha$  we see that the photoresponse appears approximately linear over six orders of magnitude for all devices, with  $\alpha \approx 1$ . A closer analysis of one device is shown in Figure 3.6b and reveals that there are three photoresponse regimes: a linear photoregime at low intensities ( $\alpha = 1.01$ ), a superlinear regime at medium to high intensities ( $\alpha = 1.24$ ), and a sublinear regime at very high intensities ( $\alpha = 0.64$ ).

A calculation of the EQE is also possible from this data, as shown in Figure 3.6b. As for the solar cell characterisation in the previous section, the values are based on the physical NW cross-section. This once again results in excessively large, physically impossible values for the EQE, due to the mismatch of physical cross-section and absorption cross-section [11, 12]. The development of the EQE follows the same three

regimes as those of the photoresponse: EQE is constant for the linear regime, increasing for the superlinear regime, and decreasing in the sublinear regime.

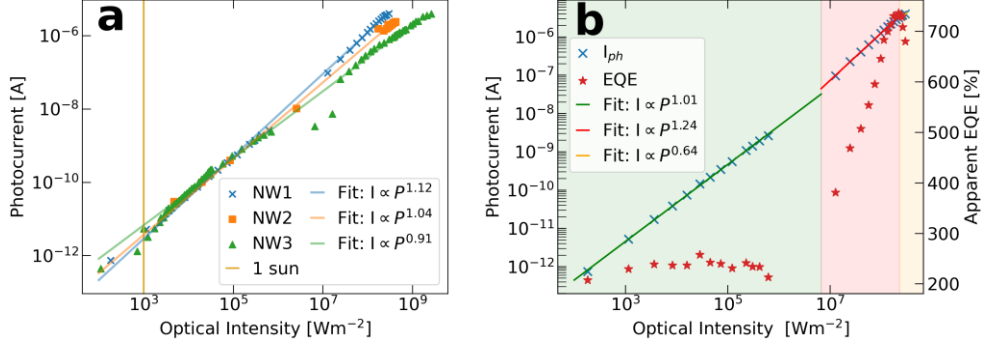


**Figure 3.6 Photocurrent response and analysis**

**a** Photocurrent response of three device with power law fits, shown in log-log. **b** A closer analysis of device labeled NW1 in **a**. Three regimes are seen for the photocurrent response, linear (green), superlinear (red), and sublinear (orange). Each has a corresponding power law fit. The apparent EQE based on the geometric cross-section of the NW is also shown for this device and also follows three regimes. Note that the photocurrent (left y-axis) is shown in log-log whereas the EQE (right y-axis) is shown with a log x-axis and linear y-axis. Adapted from paper II.

### 3.3.3 Characterisation of focal spot

By recording photocurrent images at different positions along the z-axis we can show the evolution of the beam spot through space. Using our previously obtained calibration, we can also convert the images from photocurrent to intensity. One such measurement is shown in Figure 3.7a-j, with both linear scale and log-scale images taken at 70 nm step size. A slight astigmatism is clear by the oval shape of the focus in front of and behind the focal plane at  $z = 0$ .

More interestingly, the log-scale images reveal additional detail inside the intensity distribution, as highlighted in the spot profile shown in Figure 3.7k. Here, we see along the  $y'$  profile that there are step-like features inside the intensity profile. These can also be seen in the images as ring-like features. This additional detail would be impossible to see with a commercial pixel-array detector due to density of four steps in intensity over just 2  $\mu\text{m}$ , comparable to the size of a single pixel in a commercial detector.

Following ISO 11146-1, we also analysed the focal spot diameters as shown in Figure 3.7l [112]. From this analysis, we obtain two diameters of  $d_x(0) = 2.6 \mu\text{m}$  and  $d_y(0) = 2.1 \mu\text{m}$ , which are much larger than the diffraction limited spot diameters of  $d_x = 1.0 \mu\text{m}$  and  $d_y = 1.1 \mu\text{m}$  (see paper II). The astigmatism visible in the images is also clear from the astigmatic waist separation of  $\Delta z = 0.9 \mu\text{m}$ .



While the astigmatism and other imperfections in the optical path may be responsible the difference between the theoretical and measured spot size, another possible cause could be caused by the high effective absorption area of NWs which exceeds their physical cross-section. To verify that this is not the case, optical modelling was performed.

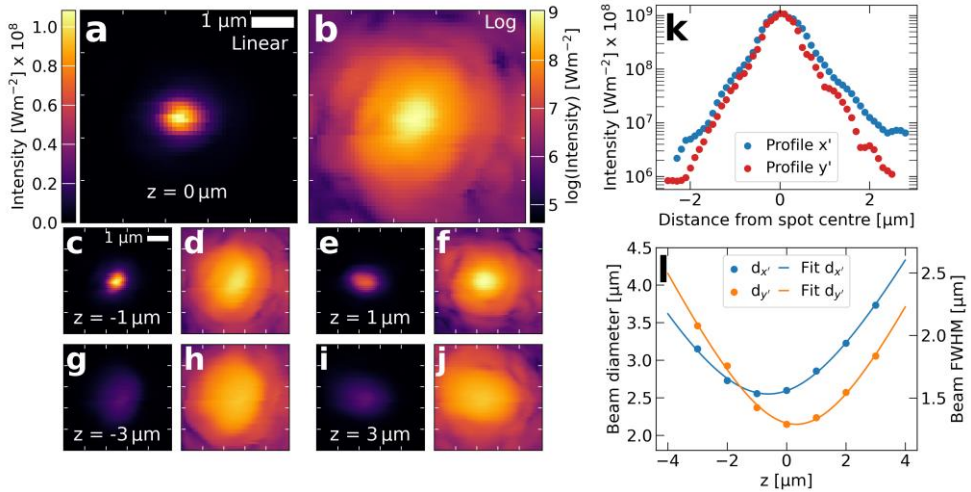


**Figure 3.7 Image slices through focal plane and spot analysis**

**a-j** Linear and log-scale images of laser focal spot taken at different z-positions using single NW photodetector at 70 nm step size. **k** Log-scale profiles of the major and minor axis of the spot at the focus ( $z = 0$ ). **l** Spot size analysis following ISO 11146-1 for image series in **a-j**. Reproduced from paper II.

### 3.3.4 Modelling of imaging with single nanowire detector

Optical modelling using finite-difference time-domain methods were performed by Assoc. Prof. Nicklas Anttu at Åbo Akademi in Finland. The 2 μm long InP NW was modelled to be fully embedded in a material of refractive index  $n = 1.5$ , a simplification ignoring the contact layers and details of the embedding isolation layer. The focused illumination was achieved by simulating a 0.8 NA lens with full filling, another difference from the experimental conditions.

The results of the modelling for a wavelength of 633 nm are shown in Figure 3.8. In Figure 3.8(a), we see that the expected spot diameters recorded with such a single NW probe are much smaller than the spot sizes observed in the experiment. This is in part due to the way the spot is simulated as perfectly diffraction limited but it shows that the enhanced optical absorption area of the single NW probe is not limiting. The experimental NW diameter of 80 nm is indicated by the dashed lines in Figure 3.8 and shows that we have, although accidentally, chosen the NW diameter which should

produce almost the smallest possible spot diameter possible when imaging. As shown in Figure 3.8b, the absorptance at our NW diameter is only around 36.1%, much lower than the maximum absorptance of 76.6% possible at 110 nm diameter. Interestingly, this increase in diameter and absorptance would not come with a huge loss in image resolution. It is therefore possible to optimise a NW detector not just for resolution but also for absorptance and sensitivity simultaneously. Additionally, the modelling was limited to NWs of 2  $\mu\text{m}$  length but an increase in NW length could also be used to increase absorption.

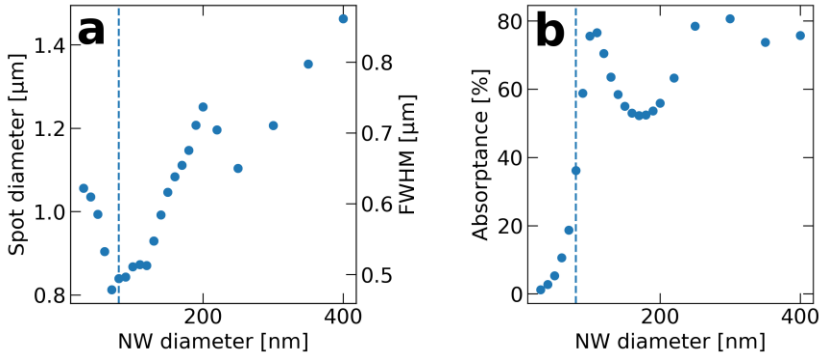


**Figure 3.8 Simulation of spot diameter and absorptance for imaging a 633 nm laser spot with single NW detector**  
**a** Relationship between apparent focal spot size and NW probe diameter. **b** Relationship between absorptance and NW probe diameter. The diameter of the NW used in the experiment is indicated by the dashed lines. Reproduced from paper II.

### 3.3.5 Imaging of a dense diffraction pattern

As a final demonstration of the capability of the detector, we image the diffraction pattern of a double slit. The double slit consists of two 100  $\mu\text{m}$  wide slits with 600  $\mu\text{m}$  spacing and is placed in the beam path ahead of the focusing objective, so that it ends up being focused by the objective. An image of the resulting diffraction pattern is shown in Figure 3.9a alongside a line profile through the centre of the diffraction pattern in Figure 3.9b. Both a single-slit and double-slit pattern are visible with the double-slit pattern having a spatial period of 2  $\mu\text{m}$ . Despite this, the fringes are clearly resolved, even for the much lower intensity second order peaks at the image edges. The patterns are also quite noise free and clear. It would be impossible to obtain such clear images with commercial array detectors due to the high spatial density, while scattering probe methods would struggle to image the low intensity parts of the image. This again highlights the capability of our single NW devices for high-resolution imaging in a direct detection scheme.

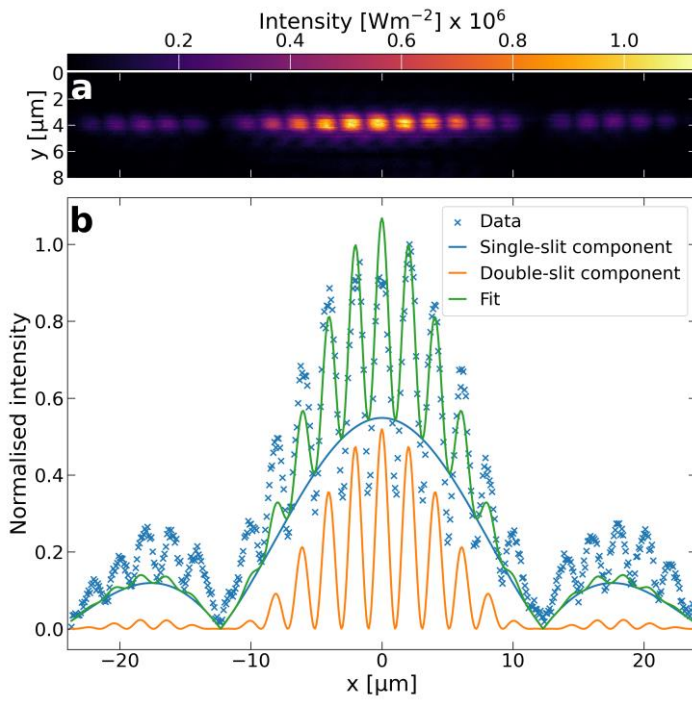


**Figure 3.9 Imaging of double-slit diffraction pattern**

**a** Image of focused double slit diffraction pattern. **b** Line profile through the centre of **a** with fitted double-slit, single-slit curves, and combined slit behaviour. Reproduced from paper II.

## 4 Horizontal single nanowire CsPbBr<sub>3</sub> devices

As MHPs have become a competitive solar cell technology [113-116], nanosized MHP devices have also proliferated [117]. Just as thin-film MHPs, they benefit from easy solvent-based fabrication methods, defect tolerance, and excellent optical properties. This has allowed for applications of MHP nanocrystals as LEDs [118, 119], lasers [38, 45, 120, 121], photo- and X-ray detectors [30, 33, 122-126].

However, while the active MHP crystal can often be a nanocrystal such as NWs, quantum dots, or nanoplates, the device features, like contacts and surface modifications such as etching, are not structured on the nanoscale. To make such features on the nanoscale, patterning methods such as the lithography methods are necessary. Unfortunately, due to their high solubility in polar solvents, MHPs are not compatible with established lithographic processing as it has been developed for conventional semiconductors like Si or III-Vs [61-65, 67].

While efforts have been made to adapt photolithography to MHPs [61, 65], EBL is more useful for working with nanoscale MHPs due to the higher resolution, adaptability of masks, and ease of alignment. Modifications to the standard version of the PMMA EBL process as used in Chapter 2 have been proposed, to make it MHP-compatible. *Zhang et. al.* utilised it with a much-reduced development time [67], while *Dou et. al.* relied on thoroughly drying the solvents before development [66]. These approaches may not be suitable for all MHPs and applications, as less stable MHPs cannot resist the solvents no matter how dry [64], nor can short development times reliably produce high-quality patterns in all cases. To remedy this, *Lin et. al.* put forth a proposal to replace the solvents with non-polar alternatives chlorobenzene and hexane [62]. The resulting process does not reproduce the performance of the existing polar developer well, which makes it difficult to pattern thick metal contacts for lift-off processes reliably. An alternative developer of *o*-xylene and hexane is put forth in the following chapter, which replicates the standard PMMA developer performance much more accurately. With it, complicated structures can be fabricated with thick metal layers, all in an MHP-compatible fashion.

However, even with the option for nanoscale contacting and processing via EBL, MHP nanocrystals still lack the band structure control that is possible for Si and III-V nanocrystals. Specifically, nanoscale heterostructures are a crucial part of commercial optoelectronic devices such as LEDs and lasers. Although heterostructured MHP NWs can be grown via CVD [45], anion exchange presents a post-growth modification option with much more versatility [69, 127, 128]. As the name suggests, during anion exchange the halide anion in an MHP is displaced by a different halide species, with a resulting shift in lattice constants and band gap. This can be utilised to tune the PL emission spectra of MHP crystals or MHP light emitting devices like LEDs and lasers. Dopant profiles and heterostructures are critical design elements for devices such as LEDs and lasers, which commonly use a heterostructure for the emissive layer [70]. It has also been proposed as a mechanism by which MHPs could be functionalised as chemical sensors [39, 129, 130].

Anion exchange was first observed for nanocrystals when precursor solution containing a different halide salt was added to colloidal nanocrystals [69]. Since then, anion exchange has been carried out using different methods and media. Solid-liquid anion exchange such as for colloidal nanocrystals has been replicated for larger crystals and films using precursor solutions but also other liquids such as halogenated solvents [131, 132]. Solid-solid halide exchange has been demonstrated by simply putting two different MHPs into physical contact [133]. Solid-gas anion exchange has also been demonstrated with halide gases, hydrohalic acids, or gaseous salts [16, 39, 129]. Often, halide exchange can be stimulated or accelerated using heat, plasma, or light stimulation [121].

Previously, halide exchange has been demonstrated on MHP NWs, including as heterostructured NWs by *Dou et. al.* [66]. However, this processing utilised niche chemicals not currently established in most cleanrooms. Instead, this chapter will describe two gas-based processes using HCl and Cl<sub>2</sub> gas to convert CsPbBr<sub>3</sub> to CsPb(Br<sub>1-x</sub>Cl<sub>x</sub>)<sub>3</sub> which are commonly available in all cleanrooms. Especially the Cl<sub>2</sub> method offers significantly higher control over the exchange parameters than either HCl or the liquid method used by *Dou et. al.* When combined with the EBL processing above, the anion exchange processing can produce heterostructured CsPbBr<sub>3</sub>/CsPb(Br<sub>1-x</sub>Cl<sub>x</sub>)<sub>3</sub> NWs with segments only hundreds of nanometers long. This demonstrates the immensely increased control possible over local MHP band and device structure when existing nanoscale processing is adapted and combined with the flexibility of MHP crystals.

In this chapter, I will first give a brief overview of MHPs as a material and explain the fundamental challenge of substituting MHP for an established semiconductor in

nanostructures. I will motivate the choice of  $\text{CsPbBr}_3$  over other MHPs as a material system for investigating NW MHPs further before discussing how free-standing  $\text{CsPbBr}_3$  NWs can be grown from anodised aluminium oxide (AAO) templates. I will then describe how horizontal single  $\text{CsPbBr}_3$  NW devices can be realised by developing an MHP-compatible EBL process. Then I will discuss the phenomenon of anion exchange and how we realised it with two gas-based processes for our NWs. Finally, I will show how it can be combined with the EBL method to create MHP devices with nanoscale heterostructures.

## 4.1 Basic properties of MHPs and $\text{CsPbBr}_3$

### 4.1.1 The perovskite crystal

Perovskites are identified by their crystal structure and the general formula  $ABX_3$ , with cations  $A^+$  and  $B^{2+}$ , and anion  $X$  [63]. The cubic perovskite structure is shown in Figure 4.1, but orthorhombic and tetragonal phases are the common phases for MHPs at room-temperature [56, 134-138].

For MHPs, the anion  $X$  is a halide atom other than fluoride and at least one of the cations is a metal, most commonly Pb or Sn as the  $B^{2+}$  cation. The  $A^+$  site cation can also be a metal such as Cs or an organic cation such as methylammonium (MA)  $\text{CH}_3\text{NH}_3^+$  or formadinium (FA)  $\text{CH}_5\text{N}_2^+$ . Each site of the crystal is not restricted to just one chemical species and instead different species can occupy the same site inside the same single crystal resulting in a mixed MHP. For example, the (currently) most efficient single-junction MHP solar cell relies on a mixture of  $\text{FA}^+$  and  $\text{Cs}^+$  for the  $A^+$  crystal site [114]. This compositional flexibility can result in incredibly complicated materials compositions with different properties.

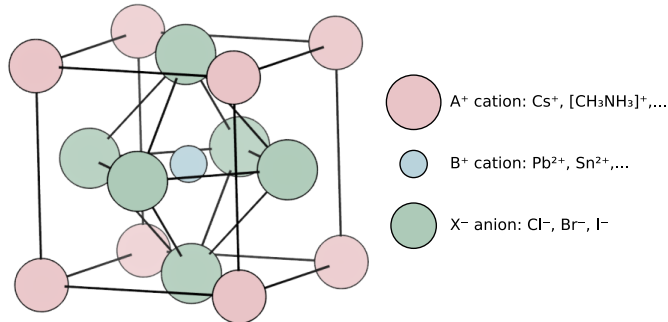


Figure 4.1 Schematic of cubic perovskite structure

### 4.1.2 MHP synthesis

Growth of MHP crystals is generally conducted via one of two methods: co-evaporation of precursor salts or crystallisation from precursor solutions [7, 16, 39, 44-46, 53, 55-57, 69, 118, 126, 127, 130, 131, 138, 139]. The precursor salts are normally  $AX$  and  $BX_3$ , e.g.  $CsBr$  and  $PbBr_2$  to create  $CsPbBr_3$ . While lead salts are mostly insoluble in water, they can be dissolved in polar organic solvents like DMSO and DMF [140, 141]. Meanwhile the  $AX$  salts, both inorganic and organic, readily dissolve in water and other polar solvents including DMSO and DMF [142, 143]. This allows for the creation of precursor solutions containing the necessary constituent salts to form MHP crystals.

Crystal growth from these precursor solutions is possible because the enthalpy of formation of MHP crystals compared to the dissolved salts is generally quite low, often even close to or above  $0 \text{ kJmol}^{-1}$  [63]. This also explains why simple co-evaporation of the salts will result in MHP crystals [63]. Very little energy is required to form these materials from the precursors and MHP formation will occur spontaneously even at low temperatures [63]. It is in part for this reason that MHPs have spread so rapidly through the research community and are generally touted as being low cost. Besides access to the necessary precursor salts and solvents, a hot plate is generally the only piece of equipment used. In terms of setup and running costs, this compares incredibly favourably to the complex reactors and precursors required for growth of Si or III-V semiconductors.

However, a direct consequence of their low enthalpy of formation is that MHPs are fragile. It takes just as little energy to revert the chemical reaction, meaning that degradation mechanisms can occur under mundane conditions simply from heat, illumination, and most notably from polar solvents [144]. While, as previously stated, lead salts are not very soluble, Cs-halides and organic halide salts are soluble even in water. This can lead to a degradation mechanism where the Cs or organic salt is leached out of the perovskite structure, leaving a Pb-halide husk [144]. The humidity in the air is sufficient to cause this degradation for many MHPs which necessitates the use of dry  $N_2$  gloveboxes for their synthesis and processing.

### 4.1.3 Properties of $CsPbBr_3$ and $CsPb(Br_{1-x}Cl_x)_3$

The MHP used in this thesis is  $CsPbBr_3$  alongside the intermediate Br-Cl mixed system  $CsPb(Br_{1-x}Cl_x)_3$ . Although  $CsPbBr_3$  is not competitive for solar cell devices due to its relatively large band gap (525 nm, 2.36 eV), it performs well in applications such as X-ray detectors [125, 126, 145, 146]. Additionally, it is among the most chemically stable MHPs [63, 147]. This is due to a comparatively high enthalpy of formation and makes

CsPbBr<sub>3</sub> an attractive choice for testing novel processes in a conventional cleanroom environment outside of a glovebox.

The properties of the mixed-halide CsPb(Br<sub>1-x</sub>Cl<sub>x</sub>)<sub>3</sub> lie in between these values as estimated by Vegard's law, which is a heuristic approach for estimating band gaps and lattice parameters of mixed crystals [148]. The lattice constants  $a_{Cl/Br}$  and band gap  $E_{G,Cl/Br}$  for the mixed CsPb(Br<sub>1-x</sub>Cl<sub>x</sub>)<sub>3</sub> are then given as:

$$E_{G, \frac{Cl}{Br}} = x \times E_{G, Br} + (1 - x) \times E_{G, Cl} \quad (4.1)$$

$$a_{G, \frac{Cl}{Br}} = x \times a_{G, Br} + (1 - x) \times a_{G, Cl} \quad (4.2)$$

This allows the band gap of the CsPb(Br<sub>1-x</sub>Cl<sub>x</sub>)<sub>3</sub> system to cover a large part of the visual spectrum. If CsPb(Br<sub>1-x</sub>I<sub>x</sub>)<sub>3</sub> is included in the consideration, this extends the range covered by the CsPbX<sub>3</sub> system to effectively the full range of the visual spectrum, with band gaps (wavelengths) of 3.04 eV (408 nm), 2.37 eV (523 nm), and 1.77 eV (700 nm) for CsPbCl<sub>3</sub>, CsPbBr<sub>3</sub>, and CsPbI<sub>3</sub> respectively [69, 149]. It should be noted that while Cl/Br and Br/I mixed MHPs are possible, Cl/I mixed MHPs are not due to the large difference in ionic radii and resultant lattice strain [69].

## 4.2 Synthesis of free-standing CsPbBr<sub>3</sub> nanowires via AAO templates

Growth of MHP NWs has been achieved for different MHP compositions and using different growth methods. Co-evaporation has been used to produce NWs via a VLS regime, mimicking the growth method used for InP NWs such as those described in Section 3 [16, 44-46]. Solution-based approaches have achieved NWs via both hot injection and template-assisted growth [7, 39, 53, 55-57, 69, 118, 126, 127, 130, 131, 138, 139]. The method growth used in this thesis is a form of template-assisted growth.

### 4.2.1 Anodised aluminium oxide

AAO is an inexpensive material with a wide range of commercial uses. When aluminium is electrochemically anodised, AAO forms in a self-aligned fashion forming a hexagonal matrix of pores [150-152]. The pore diameters can be as small as tens of nanometers and can be controlled by the electrochemical process parameters. The AAO can be both attached to a substrate or free-standing with pores open on both sides.



The shape and aspect ratio of the AAO pores is well suited for the growth of NW-like crystals on the inside. When investigating the use of AAOs as a matrix for CsPbBr<sub>3</sub> NW scintillators, we found that the NWs grow not only on the inside of the pores but continue to grow outside the AAO template as free-standing NWs.

#### 4.2.2 Growth of free-standing CsPbBr<sub>3</sub> nanowires

For our NW growth we use free-standing AAO templates with pore diameters of 200 nm to 350 nm. The precursor solution consists of 0.3 M of CsBr and 0.3 M of PbBr<sub>2</sub> in DMSO. This solution is dispensed onto a glass slide and then the AAO is placed onto the precursor droplet which infiltrates the pores via capillary forces. The sample is then placed on a 70 °C warm hot plate allowing the DMSO solvent to evaporate. As supersaturation of precursor salts is reached CsPbBr<sub>3</sub> crystals first form inside the pores where they grow into NWs encapsulate and guided by the pore shape. Later in the growth process, crystallisation also occurs on the AAO and glass surfaces as bulk crystal and at the same time free-standing NWs grow out of the AAO pores as a continuation of the NW crystals inside the pores. Notably, the growth of these NWs occurs preferentially on the downwards facing side of the AAO.

This growth mechanism is surprising since the NW growth outside the AAO pores occurs without any spatial confinement by the template. From XRD and TEM measurements, the NWs were found to be single crystalline and grow such that the

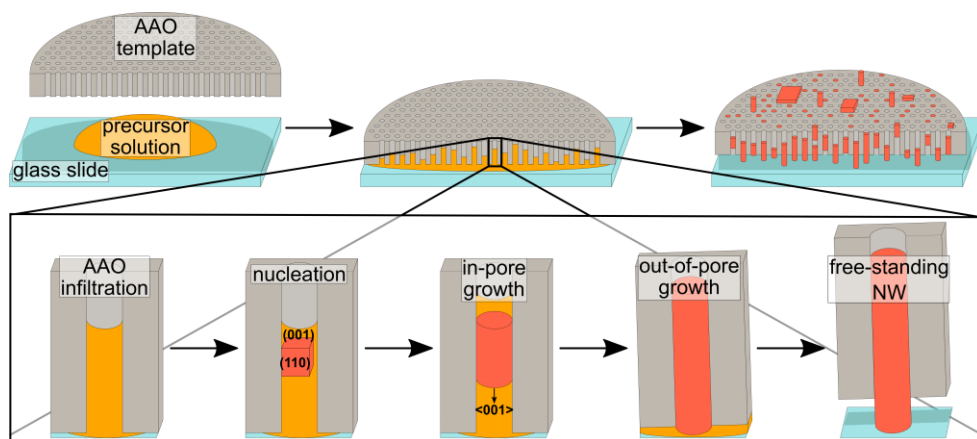


**Figure 4.2 Illustration of the growth of free-standing CsPbBr<sub>3</sub> nanowires from AAO templates**

Top shows the macroscopic view of the growth process, where the AAO template is placed onto a droplet of precursor solution, which infiltrates the AAO pores and growth CsPbBr<sub>3</sub> NWs and crystals. Bottom shows a close up of a single AAO pore throughout growth. It first fills with precursor solution, then a seed crystal nucleates, the growth propagates along the pore along the <001> direction, before continuing outside the AAO pore and resulting in a free-standing CsPbBr<sub>3</sub> NW.

(001) plane is perpendicular to their long axis with sidewall facets formed by the (110) plane. This means that the NWs must grow preferentially along the  $\langle 001 \rangle$  crystal direction, an effect which has also been observed in purely solution-based growth without any template [153]. This indicates that the solid-solid interfacial energy of the  $\text{CsPbBr}_3/\text{AAO}$  and the solid-liquid interfacial energy at the  $\text{CsPbBr}_3/\text{precursor solution}$  interface must be higher for the (001) crystal plane than the (110) crystal plane [154], as the NWs both crystallise with the (110) plane in contact with the AAO wall and then continue to grow such outside the AAO. This description is likely incomplete, as significant amounts of non-NW growth are nonetheless observed. The growth process must therefore lie in a careful balance where locally surface energies, supersaturation, temperatures and seed crystals combine to allow for NW growth.

The NW length can be adjusted by changing the precursor volume, as shown in Figure 4.3. Precursor amounts of 7  $\mu\text{L}$ , 15  $\mu\text{L}$ , and 25  $\mu\text{L}$  were used for growth, yielding NWs with average lengths of 3.2  $\mu\text{m}$ , 10  $\mu\text{m}$ , and 18  $\mu\text{m}$ , respectively. The longest NWs can reach up to 30  $\mu\text{m}$  in length.

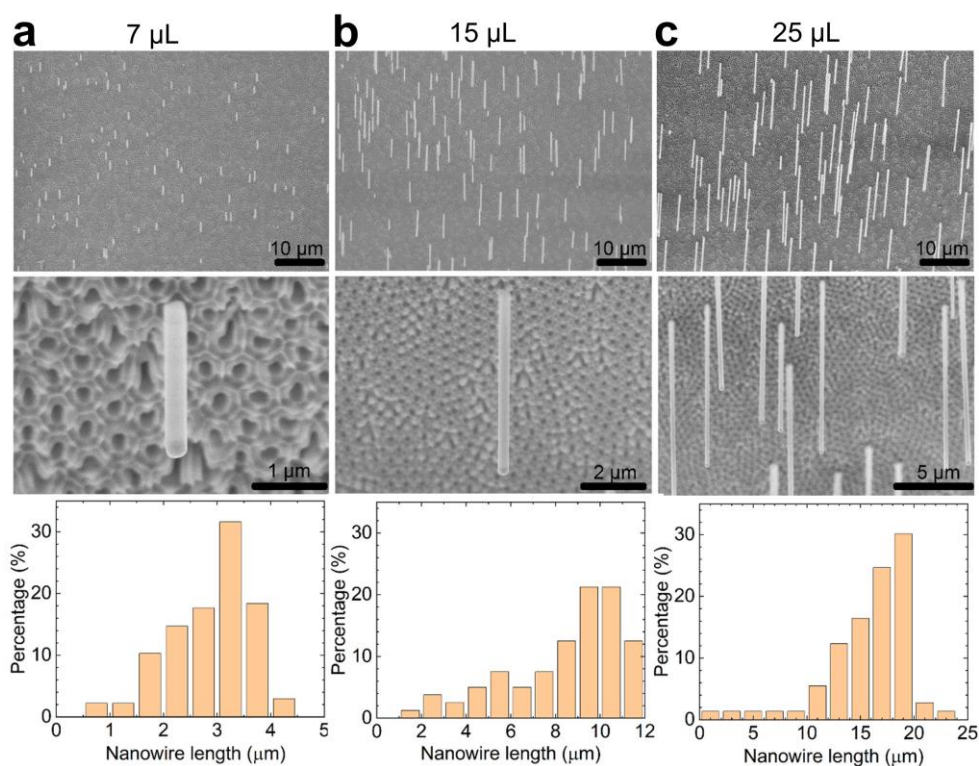


**Figure 4.3 Influence of precursor volume on free-standing nanowire length**

**a-c** SEM images taken at a 30° tilt and NW length statistics for NW growth using 7  $\mu\text{L}$ , 15  $\mu\text{L}$ , and 25  $\mu\text{L}$ , respectively. NWs clearly increase in length with greater precursor volume. Reproduced from paper III.

### 4.2.3 Improvement of growth via controlled-flow reactor

To further optimise the yield of free-standing NWs and obtain greater control over the growth, the growth can be conducted not in an open fume hood as in paper III but instead inside a controlled-flow reactor as described in paper VI. Unlike a complex MOCVD reactor such as those used for III-V growth, the reactor here is simply an enclosed chamber with gas inlet and outlet to allow for a controlled gas flow across the growth template.

The NW growth mechanism relies heavily on the formation of a supersaturation followed by the formation of a seed crystal and its subsequent growth, as explained previously. Supersaturation occurs based on the rate of evaporation of DMSO from the precursor solution which can be controlled not just by changing the temperature but also by the concentration of DMSO in the air above the sample. Optimising the gas flow during the growth should therefore allow for more consistent and controlled NW growth.

By SEM imaging, the yield of free-standing NWs per sample was estimated based on both temperature and flow rate of  $N_2$  across the sample, as shown in Figure 4.4. At the previously chosen temperature of 70 °C, a flow rate of 0.8 L min<sup>-1</sup> provides the highest yield of NW producing areas. When altering the temperature at this fixed flow rate, we find the best results still at 70 °C. This indicates a consistent match of temperature and flow rate for our growth system and reactor, which affords significantly more control and consistency when producing free-standing CsPbBr<sub>3</sub> NWs.

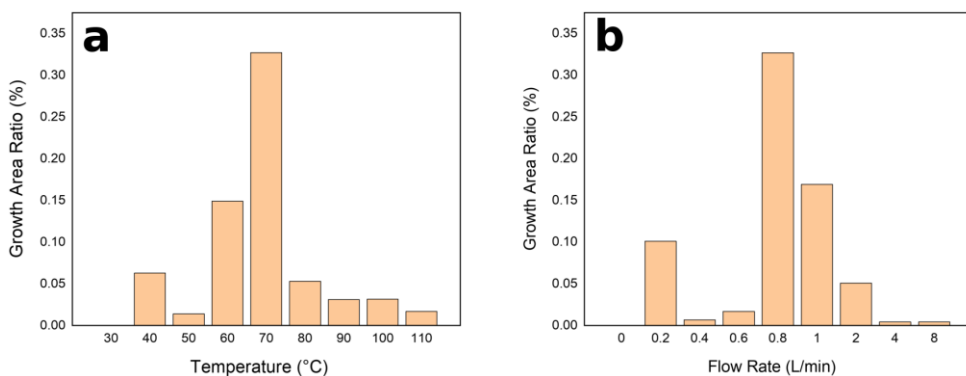


**Figure 4.4 Effect of growth temperature and flow rate on nanowire yield in controlled-flow reactor**  
**a-b** Growth area ratio as assessed by SEM images and its variation with temperature and flow rate, respectively. Reproduced from paper VI.

## 4.3 Horizontal single CsPbBr<sub>3</sub> nanowire devices

To fabricate devices from the single CsPbBr<sub>3</sub> NWs, as has been done for single NWs of other semiconductors, we first transfer the NWs to a new substrate so that they are no longer free-standing but lying horizontally. Then, we need to connect these NWs electrically by patterning and depositing contacts in an aligned fashion. It is during this step that the fragility of MHPs impacts our processing significantly. The lithographic methods that have been developed for contacting Si or III-V semiconductor NWs cannot be applied to MHPs without alteration due to high solubility of MHPs in polar solvents.

### 4.3.1 Lift-off processing

The lift-off process generally used for contacting consists of five steps which are also illustrated in Figure 4.5a for the case of PMMA resist:

1. Spin coat or otherwise deposit a polymer resist layer stack.
2. Write the pattern into the polymer resist layer as a local chemical change. This is typically done using electrons or light.
3. Transfer the written pattern into the resist layer physically. For this, we use a solvent that selectively dissolves either only the exposed or only the unexposed resist material (called positive and negative lithography, respectively). This process is called development, the selective solvent correspondingly is called developer.
4. Evaporate or sputter new material (e.g. electrode metal) onto the sample. Other surface modifications are also possible, such as etching or anion exchange as described later in Section 4.4.
5. Remove the polymer resist layer alongside any material deposited onto it by immersion into a solvent. This leaves behind any material that was deposited directly onto the sample surface. This is called step the lift-off and the solvent is referred to as the remover.

The combination of resist, developer, patterning process, and remover form a resist system. For the resist system to work, the resist material needs to be chemically sensitive and easily removable via solvents. At the same time, a developer chemical must exist that shows sufficient selectivity to differentiate exposed and unexposed material. If the developer is not selective enough then the sidewalls of the written features can become sloped and gradual. As a result, the lift-off step becomes difficult, if not impossible.

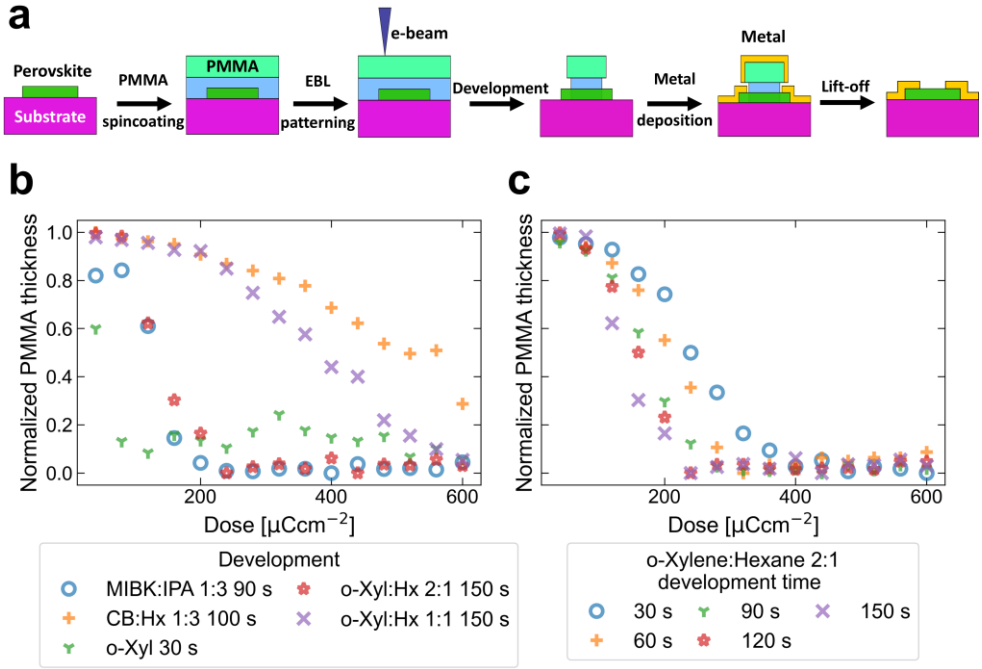


**Figure 4.5 Schematic of EBL lift-off process and EBL developer behaviour**

**a** Schematic of EBL lift-off processing using a double-layer PMMA resist. **b** Development behaviour of different developer solutions for PMMA EBL processing. Shown is the normalised thickness of the PMMA (apparent depth of the developed feature) with a value of 0 indicating full development with no dissolution of unexposed PMMA and 1 meaning no PMMA was dissolved. **c** Development behaviour of *o*-xylene:hexane 2:1 solution for different development times. Reproduced from paper IV.

In addition, all the chemicals involved must also be compatible with the underlying sample material.

It is this combination of criteria that makes lithography on MHPs difficult. While a wide variety of resist systems is available commercially, they have generally been developed for Si or III-V materials, which are much more chemically resistant compared to MHPs. We therefore cannot simply use these processes but instead must adapt and modify them to circumvent the instability of MHPs. For use with our NWs, we therefore modified the processing for PMMA as an EBL resist, specifically the development step (step 3 in the list above).

#### 4.3.2 MHP-compatible EBL with PMMA resist

PMMA has a high solubility in non-polar solvents [155] and is commercially available in MHP-compatible solvents like anisole or chlorobenzene. The de-facto standard processing for PMMA is described in paper I. The accepted standard developer is a

solution of MIBK:IPA 1:3 with acetone used as the remover. Acetone is easily replaced with a non-polar MHP-compatible solvent like anisole, chlorobenzene, or toluene. Both MIBK and IPA are moderately polar solvents as well and are generally not compatible with MHPs containing organic cations like MA or FA [62, 65]. However, the MIBK:IPA and acetone processing has been reported for use with CsPbBr<sub>3</sub> but in this case special care was taken to dry the solvents, i.e. to remove any water that may have mixed into the solvents as a result of humidity and storage [66, 156]. Besides this case of using the MIBK:IPA process there also exists a report on using a 1:3 mixture of chlorobenzene:hexane [62]. We investigated this mixture but could not obtain successful lift-offs with it. As an alternative we investigated a non-polar developer consisting of *ortho*-xylene (*o*-xylene) and hexane, where the *o*-xylene dissolves the PMMA while the hexane moderates via dilution.

To quantify the effectiveness of the development, we measure the apparent depths of the features written with EBL compared to the thickness of the as spin coated PMMA. The resulting data showing the development behaviour of MIBK:IPA 1:3, chlorobenzene:hexane 1:3, and several mixtures of *o*-xylene:hexane (1:0, 2:1, 1:1, 1:2) is shown in Figure 4.5b-c for a PMMA495/PMMA950 bi-layer resist using 20 kV acceleration voltage. At a normalised thickness of 1 the depth of the developed feature is 0 nm, whereas at a normalised thickness of 0 the depth of the developed feature is the entire pre-exposure PMMA layer of 400 nm. A value of 0 is ideal, since it means that the unexposed PMMA layer was not dissolved while the exposed PMMA is fully removed. A value above 0 indicates either that the exposed PMMA is not fully dissolved or that unexposed PMMA has also been dissolved, reducing the apparent feature depth. The number therefore indicates a combination of developer efficacy and developer selectivity.

We find that the *o*-xylene:hexane 2:1 mixture performance effectively mimics the MIBK:IPA performance. More dilute *o*-xylene solutions are too weak to develop at comparable doses while undiluted *o*-xylene develops quickly but never reaches a normalised thickness of 0. In this case, this indicates that it is not very selective. Similar behaviour is observed for the chlorobenzene:hexane formulation that was reported in literature and also never reaches a value of 0 [62]. This is likely due to a lack of selectivity where the unexposed PMMA is also dissolved which results in a lower resist thickness and sloped sidewalls without an undercut profile. In combination, these factors make the lift-off step much more difficult.

We can use the *o*-xylene:hexane process to create dense nanoscale features and extremely small features, such as the line and single lines shown in Figure 4.6a. This demonstrates that the process can be used to create the sorts of features we need to contact single NWs.

### 4.3.3 Fabrication of horizontal single CsPbBr<sub>3</sub> nanowire devices

To fabricate the single CsPbBr<sub>3</sub> NW devices, we first transfer the standing NWs from the AAO substrates to new substrates with prepared marker systems. The transfer is done using the folded tip of a cleanroom tissue. This tip is first scratched across the AAO surface where it picks up NWs and then across the sample surface where some of the picked-up NWs are deposited. We then image the transferred NWs in the SEM to locate them within the marker system and design corresponding EBL masks.

We use the adapted PMMA EBL process, as described in paper IV. Besides changing the developer solution to *o*-xylene:hexane 2:1, there are a few other necessary changes. We lower the baking temperature for the PMMA to 60 °C to avoid going above the phase transition temperature for CsPbBr<sub>3</sub> [135] but compensate by prolonging the baking step to 20 min. We also alter the development process by adding a short dip in *o*-xylene in between the development and rinse steps. This produces a cleaner developed surface and prevents redeposition of PMMA particulates from the developer solution onto the sample surface. We confirm that no degradation occurs by measuring the NW PL throughout the processing. The NWs remain photoluminescent and show a consistent CsPbBr<sub>3</sub> peak around 520 nm, visible in Figure 4.6d-e. SEM images of the finished devices are found in Figure 4.7a-c.

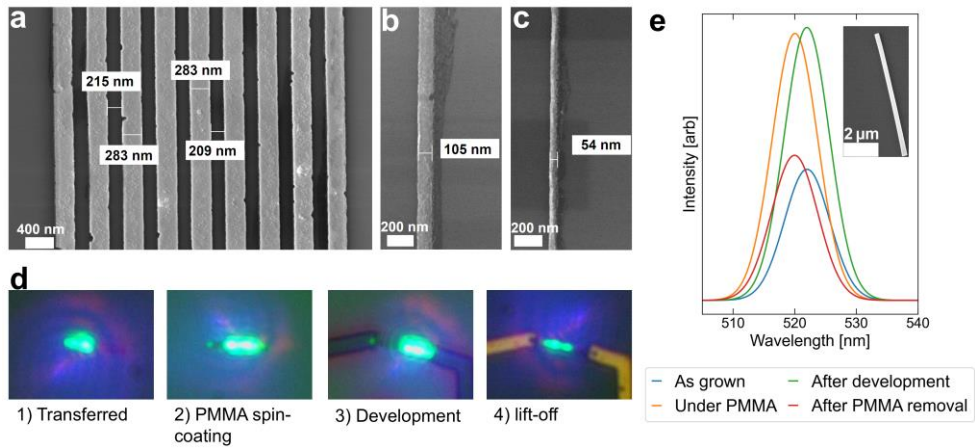


**Figure 4.6 SEM images of EBL test structures and PL of a nanowire throughout PMMA EBL processing**  
**a-c** SEM images of high-resolution test structures made with MHP-compatible EBL lift-off process. **a** Grating with a design pitch of 250 nm. **b-c** Single lines with design widths of 100 nm and 50 nm, respectively. **d** Optical PL microscopy images of the same CsPbBr<sub>3</sub> NW throughout the different steps of the MHP-compatible EBL lift-off process. **e** PL spectra of the same NW as in **d**. Inset shows an SEM image of the transferred CsPbBr<sub>3</sub> NW. Reproduced from paper IV.

### 4.3.4 Optoelectronic characterisation

We measured the resulting single NW devices electrically, with the current-voltage characteristics for one such device shown in Figure 4.7d. Without illumination, we find that the devices are not very conductive with currents below 1 pA even for bias voltages up to 4 V. However, once we induce photogenerated carriers by illumination with  $16 \text{ mWcm}^{-2}$  of 395 nm light, the currents increase by an order of magnitude to 20 pA. By biasing the device with 5 V and turning the illumination on/off, we can demonstrate an extremely strong photoresponse as shown in Figure 4.7e.

The shape of the current-voltage characteristics is not that of a simple ohmic resistor curve. Instead, the current-voltage characteristics are non-linear with a pronounced hysteresis which becomes very clear at logscale, as can be seen in Figure 4.8a-d. We attribute this not to poor contact quality, but to the high ionic mobility in MHPs. In fact, subsequent studies have indicated that the contacts are ohmic [157]. Instead, ionic movement convolutes carrier dynamics with ionic drift and resultant shielding effects. Without any external bias, ions are uniformly distributed throughout the crystal but once we begin biasing, Br-anions will move to the positive terminal, with possible movement of Br-vacancies to the negative terminal [157, 158]. Since the movement of the ions opposes the external electric field, this causes the anions and vacancies to shield the external field which affects the carrier transport through the device. The resulting transport phenomena are therefore highly dynamic and complex.

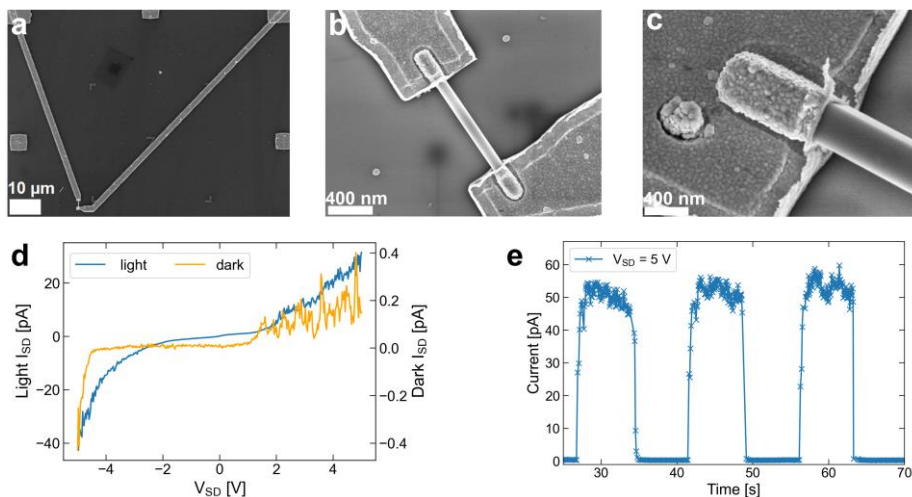


**Figure 4.7 SEM images and electrical characterisation of single CsPbBr<sub>3</sub> NW devices**

**a-c** SEM images of different single CsPbBr<sub>3</sub> NW devices. **a** Overview image of contact traces to single CsPbBr<sub>3</sub> NW. **b-c** Close-ups of single NW devices, note the square sidewalls of the NW visible in **c**, which is taken at a 30° tilt. **d** Current-voltage characteristics of a single CsPbBr<sub>3</sub> NW device with and without illumination. **e** On/Off photoresponse of single CsPbBr<sub>3</sub> NW device. Excitation in **d-e** was provided using an unfocused 395 nm laser with an approximate excitation intensity of  $16 \text{ mWcm}^{-2}$ . Reproduced from paper IV.



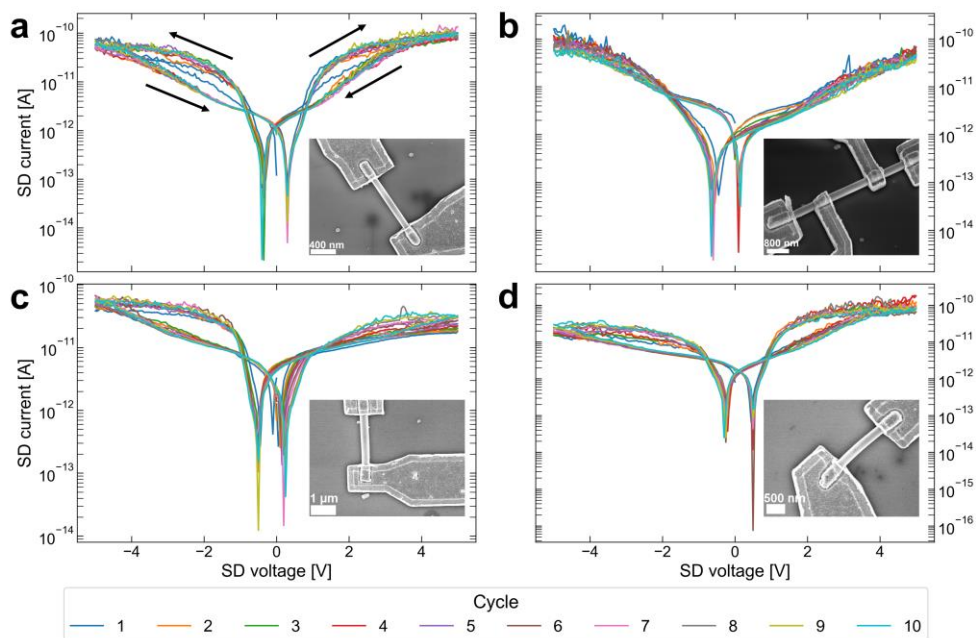


**Figure 4.8 Log-scale current-voltage characteristics of several single CsPbBr<sub>3</sub> NW devices**

**a-d** Photocurrent measurements (same excitation as Figure 4.7) for four different devices. Ten cycles of source-drain (SD) bias are shown for each device, which exhibit a similar shape with significant hysteresis. The sweep direction is indicated by the arrows in **a** and identical in the other measurements. Insets on each panel show an SEM image of the device under test. Note that the SEM image in **b** is taken at a 30° tilt. Reproduced from paper IV.

## 4.4 Anion exchange for CsPb(Br<sub>1-x</sub>Cl<sub>x</sub>)<sub>3</sub> nanowires

During anion exchange the  $X$  anion of an  $ABX_3$  MHP is exchanged for a different anion  $Y$ . This phenomenon appears to be unique to MHPs and not perovskite crystals generally. The precise mechanisms behind anion exchange are still not fully understood but it is currently thought to be a simple diffusion process mediated by the large amount of halide vacancies that typically form in MHPs during crystal growth [69]. This view is strengthened by the observation that anion exchange can be prevented if the MHP is given a post-growth treatment meant to fill halide vacancies [159].

In the following section, I will describe how we can use anion exchange to turn our CsPbBr<sub>3</sub> NWs into CsPb(Br<sub>1-x</sub>Cl<sub>x</sub>)<sub>3</sub> NWs using a gas-based exchange process. I will describe the two exchange processes I investigated and how I used PL and EDS to characterise them. I will then describe how we can model the diffusion into a NW and use it to extract diffusion parameters from our PL and EDS data to better understand the anion exchange. Lastly, I will show how we can combine anion exchange with our

previously developed EBL technique to create nanosized  $\text{CsPbBr}_3/\text{CsPb}(\text{Br}_{1-x}\text{Cl}_x)_3$  heterostructures in our NWs.

#### 4.4.1 Anion exchange processing with HCl and $\text{Cl}_2$ gases

Two easily available gas-based halide sources are HCl and  $\text{Cl}_2$ , both of which are staples in many cleanrooms. HCl is easily available as an aqueous solution and  $\text{Cl}_2$  gas is often found in Cl-based reactive ion etchers used for etching of metals such as chromium. Just as for the fabrication of single  $\text{CsPbBr}_3$  NW devices, the first step towards characterising the anion exchange was to transfer the NWs from the growth AAO to a new substrate.

The HCl-based process, as illustrated in Figure 4.9b, relies on placing the sample containing the NWs at the opening of a beaker containing concentrated HCl (37 wt%, 12M). At 24 °C, the partial pressure of HCl above the solution is expected to be roughly  $1.5 \times 10^{-3}$  bar [160]. It is this gaseous HCl which provides Cl-anions for the anion exchange process with the  $\text{CsPbBr}_3$ . An SEM image of an unexchanged reference NW can be seen in Figure 4.10a, while NW exchanged via the HCl process is shown in Figure 4.10b.

In Figure 4.9c, the  $\text{Cl}_2$ -based process is illustrated. Here we make use of a commercial RIE tool with  $\text{Cl}_2$  and Ar as process gases. We create a partial pressure of  $3.33 \times 10^{-5}$  bar  $\text{Cl}_2$  gas above the sample and supplement with Ar to reach a total pressure of  $1.33 \times 10^{-4}$  bar. While the tool is a plasma etcher, the plasma is never activated, and anion exchange simply occurs between the  $\text{Cl}_2$  gas and the  $\text{CsPbBr}_3$  NWs at room temperature. An SEM image of a NW exchanged via the  $\text{Cl}_2$  process is shown in Figure 4.10c alongside an EDS line profile along the same NW.

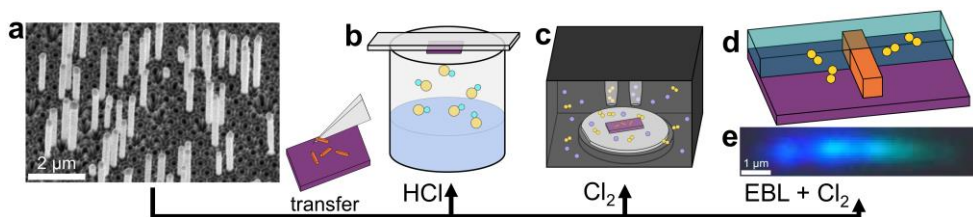


**Figure 4.9** Anion exchange processing for conversion of single  $\text{CsPbBr}_3$  nanowires to  $\text{CsPbBr}_3/\text{CsPb}(\text{Br}_{1-x}\text{Cl}_x)_3$  nanowires **a** SEM image of free-standing NWs on AAO before transfer taken at 30° tilt. **b-d** Schematics of HCl,  $\text{Cl}_2$ , and  $\text{Cl}_2$  heterojunction anion exchange processing. **e** PL microscopy optical image of heterojunction  $\text{CsPbBr}_3/\text{CsPb}(\text{Br}_{1-x}\text{Cl}_x)_3$  NW. Reproduced from paper V.

#### 4.4.2 Correlating PL and EDS with anion exchange

We investigated the HCl-based process for exposure times of 15 s to 90 s and the Cl<sub>2</sub>-based process for exposure times of 30 s to 300 s. To measure and classify how the crystal composition changes during the process we use PL and energy-dispersive spectroscopy (EDS) measurements.

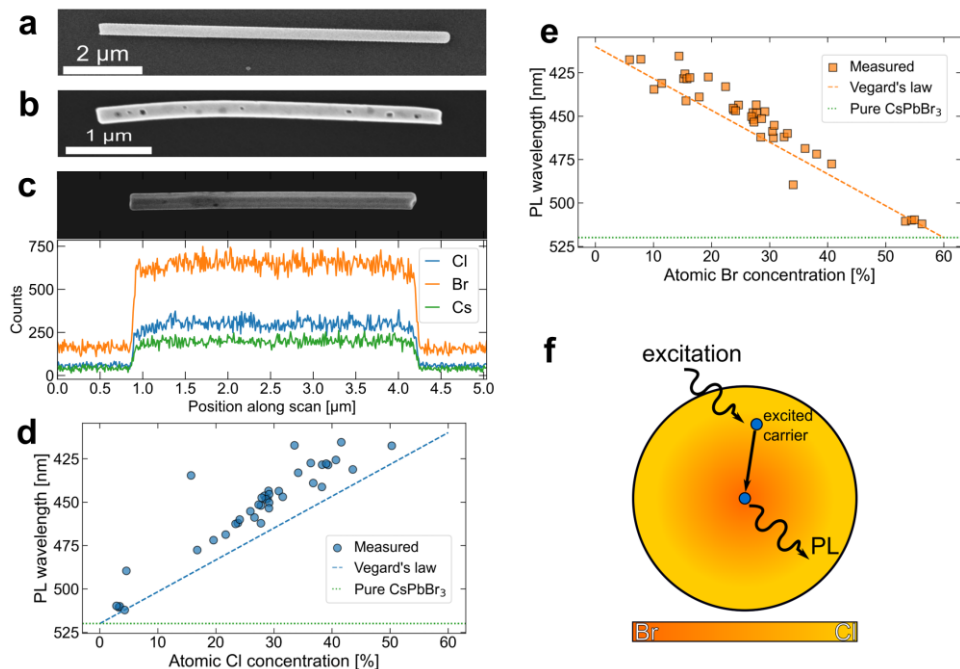


**Figure 4.10 EDS characterisation of CsPb(Br<sub>1-x</sub>Cl<sub>x</sub>)<sub>3</sub> nanowires and its relationship to PL emission**

**a-c** SEM images of unexchanged, HCl exchanged, and Cl<sub>2</sub> exchanged NWs, respectively. EDS line profile for the Cl<sub>2</sub> exchanged NW is shown in **c**. **d-e** PL peak emission wavelength versus Cl and Br concentrations as measured with EDS. **f** Schematic of radial migration of photoexcited carriers illustrating how PL peak wavelength is probed from NW core, which is Br-rich and hence has a longer PL emission wavelength. Reproduced from paper V.

Since the PL emission wavelength depends on the semiconductor band gap, we can use it to characterise the halide composition of the NWs because the band gap is linked to the halide composition as described by Vegard's law (Eq. 4.1–4.2). While this indirectly probes the composition, EDS directly probes the composition based on the emission of characteristic X-rays under electron beam excitation. This is especially powerful due to the high spatial resolution and ability to directly correlate each pixel of an image with a corresponding X-ray spectrum, as is done in Figure 4.10c for a Cl<sub>2</sub> exchanged NW.

A difference between the compositions determined via EDS and PL may arise in case of a radial composition variation inside the NW. While the EDS is more surface

sensitive, it still generates a signal from the entire diameter of the NW. This is attested by a strong Si peak from the substrate, which is always visible, even from underneath a NW. In contrast, the photocarriers generated by the excitation laser during PL measurements are likely to migrate to and recombine in the lowest band gap region. As illustrated in Figure 4.10f, this would lead us to generally observe a PL wavelength that is related more towards the composition of the more Br-rich NW core than to the average NW composition.

The relationship between PL emission wavelength and concentrations of Br and Cl as obtained with EDS are shown in Figure 4.10d-e. A clear linear relationship as expected from Vegard's law is apparent. However, we see that the Br concentration is consistently overestimated whereas Cl is consistently underestimated as compared to the values expected from PL. Since X-ray fluorescence yield scales with the atomic number of an element and Cl has a much lower atomic number than the other probed elements, this underestimation is not unexpected [161]. For all the samples, it remains clear that the total halide component stays around 56%. While this is lower than the expected 60%, this error is more likely due to the calibration and the fact that it does remain consistent is evidence that we are indeed exchanging anions.

#### 4.4.3 Anion exchange behaviour of HCl and Cl<sub>2</sub> processes

The PL peak wavelength vs. process time is shown in Fig 4.11a-b for both processes. The Cl<sub>2</sub> process saturates after around 100 s of exposure, reaching a final PL emission wavelength corresponding to around 94% Cl or  $x = 0.94$  in CsPb(Br<sub>1-x</sub>Cl<sub>x</sub>)<sub>3</sub>. Meanwhile, the HCl process saturates after 80 s but reaches a much more thorough conversion towards pure CsPbCl with a final PL emission wavelength of 415 nm, equivalent to 99% Cl or  $x = 0.99$  in CsPb(Br<sub>1-x</sub>Cl<sub>x</sub>)<sub>3</sub>. The difference in anion exchange completeness could originate with several factors.

Firstly, the partial pressure of Cl<sub>2</sub> used is much lower than that of HCl. This reduces the concentration gradient driving diffusion of Cl into the NW. Secondly, the chemical reaction that takes place at the NW surface to exchange a Br anion for a Cl anion is likely to be markedly different between the processes and occurring at different rates. Lastly, there may be a difference in vacancy levels between the NWs due to growth-to-growth variation. Both the corrosive nature of HCl and the presence of water vapour from the concentrated HCl solution could increase the number of vacancies, accelerating the anion exchange process.

Another question is the effect the anion exchange has on the PL emission intensity. Generally, we expect that there should be a decline in the PL emission intensity because

the EQE of  $\text{CsPbCl}_3$  is lower than that of  $\text{CsPbBr}_3$  [128], but also because for pure  $\text{CsPbCl}_3$  the excitation wavelength 405 nm is very close to the PL emission wavelength of 415 nm which reduces the absorption and excitation efficiency. Since we observe that the NWs appear etched and damaged from the HCl process (Figure 4.10b), we would expect these NWs to contain more non-radiative defects which would quench the PL intensity. When we look at the PL intensity vs. PL peak position as shown in Figure 4.11c, we find that as expected the PL is severely reduced at lower wavelengths to less than 1% of the original intensity for fully exchanged NWs. However, the behaviour appears identical for HCl-exchanged NWs and  $\text{Cl}_2$ -exchanged NWs despite the high level of visible damage to the HCl-exchanged NWs. This is quite remarkable and demonstrates the high level of defect tolerance that MHPs are known for.

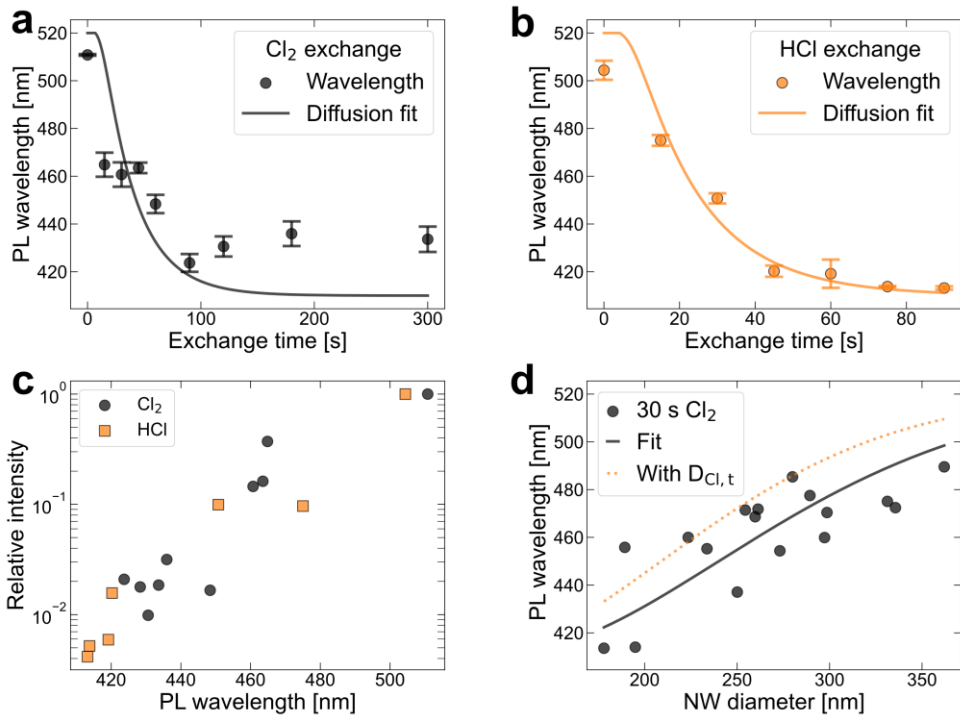


**Figure 4.11 Comparison of HCl and  $\text{Cl}_2$  anion exchange processes and diffusion modelling**

**a-b** Time-dependence of PL emission wavelength for  $\text{Cl}_2$  and HCl exchange processes, respectively. Fitted curves for the diffusion model from Section 4.4.4 are also shown. **c** Evolution PL emission intensity for different PL wavelengths, i.e. for longer anion exchange times. The behaviour appears identical for both the HCl and  $\text{Cl}_2$  anion exchange process. **d** NW diameter dependency of PL emission wavelength for 30 s of  $\text{Cl}_2$  anion exchange processing. A fitted diffusion model curve using a fixed time  $t = 30$  s and a curve using parameters fit parameters from panel **a** are shown. Reproduced from paper V.

A final observation during the anion exchange process was large NW-to-NW variation in terms of the PL peak position for NWs on the same sample. The error bars in Figures 4.11a-b indicate the standard deviation for each time step. Shown in Figure 4.11d are the PL peak positions versus the diameter of the corresponding NWs only for 30 s of  $\text{Cl}_2$  processing. Even though the AAO pore size is consistent, the free-standing NWs have diameters distributed around this pore diameter. We see that during the 30 s process step NWs with diameters below 200 nm appear already almost fully exchanged with a PL peak below 420 nm, while the thickest NWs with diameters above 350 nm are only moderately blue-shifted to around 490 nm. How this effect comes to be requires a better understanding of the diffusion processes that occur during anion exchange.

#### 4.4.4 Modelling the diffusion into a nanowire

Fundamentally, diffusion refers to the movement of particles or heat along a concentration gradient, such as the movement of Cl atoms from a gas into the  $\text{CsPbBr}_3$  crystal. In a single dimension, the diffusion flux  $J$  through an area  $A$  is given by Fick's first law as [162]:

$$J = -D \frac{\partial C}{\partial x} \quad (4.3)$$

Where  $D$  is the diffusion constant (also called diffusivity) and  $C(x,t)$  is the concentration of the diffusing particles along the direction  $x$ , where  $x$  is along the surface normal of  $A$ .

As the diffusion progresses, the concentration gradient will change. This rate of change  $\frac{\partial C}{\partial t}$ , again in one-dimension, is given by Fick's second law as the differential equation

$$\frac{\partial C}{\partial t} = D \frac{\partial^2 C}{\partial x^2} \quad (4.4)$$

Collections of solutions to the resulting diffusion equations for different geometries and experimental parameters can be found in literature, such as those in Crank's "The Mathematics of Diffusion" [163]. While not all systems are analytically solvable, a system that reasonably describes the diffusion of Cl into the  $\text{CsPbBr}_3$  NWs is.

This solution is that for non-steady state diffusion into an infinite length cylinder with a finite radius  $r$  and a constant surface concentration  $C_0$ . The approximation of an infinite length cylinder can be justified by the ratio of radius to length for NWs since the radius is up to two orders of magnitude smaller than the length. Similarly, the assumption of a constant surface concentration is justified if the diffusion from the gas phase into the NW is faster than along the radial direction. This case can be understood

as a constant monolayer of  $\text{CsPbCl}_3$  at the surface of the NW which is maintained by the high concentration of Cl atoms in the gas above the NW.

It is easier not to consider the diffusion of Cl into the NW but instead consider the diffusion of Br out of the NW, which is possible because the halide concentration was observed by EDS to remain constant during the anion exchange (paper V). The radial concentration profile of Br is then given by Eq. 4.5, as described in Crank:

$$\frac{C(t,x,R)-C_1}{C_0-C_1} = 1 - \left( \frac{2}{R} \sum_{n=1}^{\infty} \frac{\exp(-D \alpha_n^2 t) J_0(\alpha_n x)}{\alpha_n J_1(\alpha_n R)} \right) \quad (4.5)$$

With  $J_0$  and  $J_1$  Bessel functions of the 0<sup>th</sup> and 1<sup>st</sup> kind, time coordinate  $t$ , and radial coordinate  $x$  defined such that  $x = 0$  at the centre of the NW. As before  $D$  is the diffusion constant and  $R$  is the maximum diffusion distance, i.e. the radius of the NW. The coefficients  $\alpha_n$  are define such that the term  $(R \times \alpha_n)$  gives the  $n^{\text{th}}$  root of the 0<sup>th</sup> order Bessel function satisfying  $J_0(\alpha_n R) = 0$ . The concentration of Br outside the NW is  $C_0 = 0$  and the starting concentration of Br inside the NW is the uniform concentration  $C_1 = 6.3$  mol/L, which can be calculated from the unit cell parameters [149]. If we assume, as described above, that photoexcited carriers preferentially recombine in the low band gap region, i.e. the NW core, then we find that the PL measurement probes the concentration exclusively at  $x = 0$ . Since  $J_0(x \alpha_n) = J_0(0) = 1$  this allows us to express the first three terms of Eq. 4.5 as:

$$C(t, x=0, R) = C_1 \frac{2}{R} \left( \frac{\exp(-D \alpha_1^2 t)}{\alpha_1 J_1(\alpha_1 R)} + \frac{\exp(-D \alpha_2^2 t)}{\alpha_2 J_1(\alpha_2 R)} + \frac{\exp(-D \alpha_3^2 t)}{\alpha_3 J_1(\alpha_3 R)} \right) \quad (4.6)$$

When we fit this equation to the data for the HCl and  $\text{Cl}_2$  exchange processes as shown in Figure 4.11(a)-(b). We use a fixed NW diameter of  $2R = 250$  nm and therefore fit only the diffusion constant  $D$ . The behaviour of the HCl process follows the equation very well but the  $\text{Cl}_2$  process deviates strongly from the equation for long exposure times. This is because we on average do not see a complete conversion to  $\text{CsPbCl}_3$  with this process. The resulting diffusivities are  $D_{\text{Cl}_2,t} = 0.9 \times 10^{-12} \text{ cm}^2\text{s}^{-1}$  for the  $\text{Cl}_2$  process and  $D_{\text{HCl}} = 1.5 \times 10^{-12} \text{ cm}^2\text{s}^{-1}$  for the HCl process. But as we discussed earlier and see in Figure 4.11d, it is incorrect to assume a uniform NW diameter. Indeed, the dependence of  $C(t = 30 \text{ s}, x = 0, R)$  on  $R$  plotted in Figure 4.11d for a fixed exchange time of  $t = 30$  s and  $D_{\text{Cl}_2,t} = 0.9 \times 10^{-12} \text{ cm}^2\text{s}^{-1}$  does not match the data well at all. If instead, we now fix the time at  $t = 30$  s and fit for the diffusivity again, we instead find  $D_{\text{Cl}_2,R} = 1.2 \times 10^{-12} \text{ cm}^2\text{s}^{-1}$ . This is both a much better fit for this data and in better agreement

with  $D_{\text{HCl}}$ . In literature, values of  $1.0 \times 10^{-12} \text{ cm}^2 \text{ s}^{-1}$  [156] and  $0.25 \times 10^{-12} \text{ cm}^2 \text{ s}^{-1}$  [133] have been reported, which are close to the values from our fitting.

The fact that we can fit this diffusion model to our data and obtain good results for both processes shows that the absorption of Cl into the NW and the diffusion of Cl inside the NW can indeed be separated, and that the underlying assumption that PL originates from the lowest band gap region appears correct. It also demonstrates that it is the solid diffusion of Cl inside the  $\text{CsPbBr}_3$  that is rate-limiting, not the absorption of Cl from the gas or mass transport within the gas phase. This is not trivial, since the mechanism of Cl absorption from the gas phase should be different for HCl and  $\text{Cl}_2$ .

## 4.5 Heterostructured $\text{CsPbBr}_3/\text{CsPb}(\text{Br}_{1-x}\text{Cl}_x)_3$ nanowires

### 4.5.1 Self-aligned free-standing heterojunctions

Returning to our free-standing  $\text{CsPbBr}_3$  NWs before transfer, we find that they are perfectly suited already for the manufacturing of heterojunctions. The free-standing sections of these NWs are surrounded by free space but below the free-standing section is the section of the NW, which is stuck inside the AAO protected from the elements.

To create heterojunctions inside these NWs, the  $\text{Cl}_2$  process is best suited because it does not etch the AAO template, unlike HCl. We then used the same parameters as before and find that we can easily produce heterojunctions, confirmed with EDS and PL measurements. Optical images taken with laser excitation clearly show the blue emission from the free-standing NWs alongside green emission from the NWs inside the AAO, as shown in Figure 4.12.

### 4.5.2 Nanostructured heterojunctions in horizontal nanowires

To make nanostructured heterojunctions or heterojunctions on horizontal NWs, we can combine the anion exchange processes with the EBL patterning process. As before, we transfer the NWs and construct EBL masks followed by EBL processing. Then, instead of evaporating metal and doing a lift-off process, we carry out an anion exchange process where the undeveloped PMMA acts as a barrier. This allows us to create NWs with simple single heterojunctions, such as that shown in Figure 4.13a-d. Here, it is also clearly visible in the PL emission, although the much lower PL emission intensity of the chlorinated segments (compare Fig. 4.11c) means that this effect is difficult to visualise with uniform excitation intensity. However, if we use a focused laser for



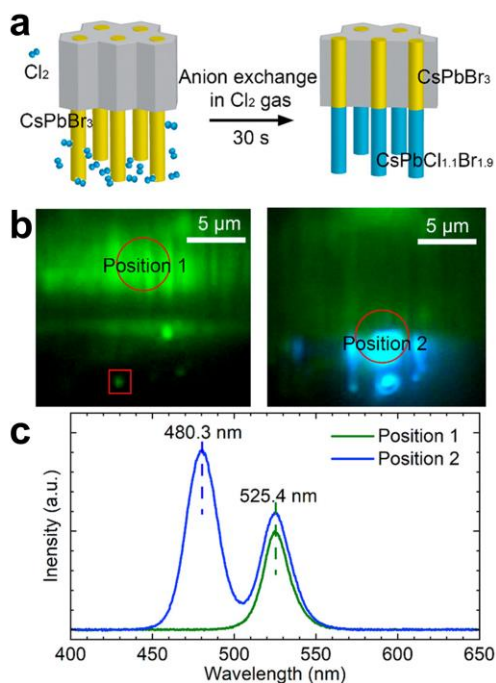


**Figure 4.12 Self-aligned heterojunctions via anion exchange of free-standing CsPbBr<sub>3</sub> nanowires**

**a** Schematic of exchange for Cl<sub>2</sub> exchange on free-standing NWs directly on AAO growth template. **b-c** PL microscopy images and PL spectra of free-standing as-grown CsPbBr<sub>3</sub> and Cl<sub>2</sub> exchanged CsPb(Br<sub>1-x</sub>Cl<sub>x</sub>)<sub>3</sub> NWs. Light guiding is clearly visible in **b** where emission occurs from free-standing NW tips (red square) while excitation occurs within the AAO bulk. Note that both images in **b** are real colour photographs, no false colour is used. Reproduced from paper III.

excitation, then we can obtain both optical images and spectra by exciting the chlorinated segment more strongly than the CsPbBr<sub>3</sub> segment. We can also create much more complicated structures, such as barcoded NWs like the one shown in Figure 4.13e-g. The smallest segments we were able to create this way were 500 nm segments and the EDS data clearly shows the changes in Br and Cl composition along the NW. Unfortunately, due to the low PL emission intensity of the chlorinated segments and/or migration of photogenerated carriers from these segments into CsPb(Br<sub>1-x</sub>Cl<sub>x</sub>)<sub>3</sub> segments, we cannot obtain PL peaks from both chlorinated and unchlorinated segments simultaneously.

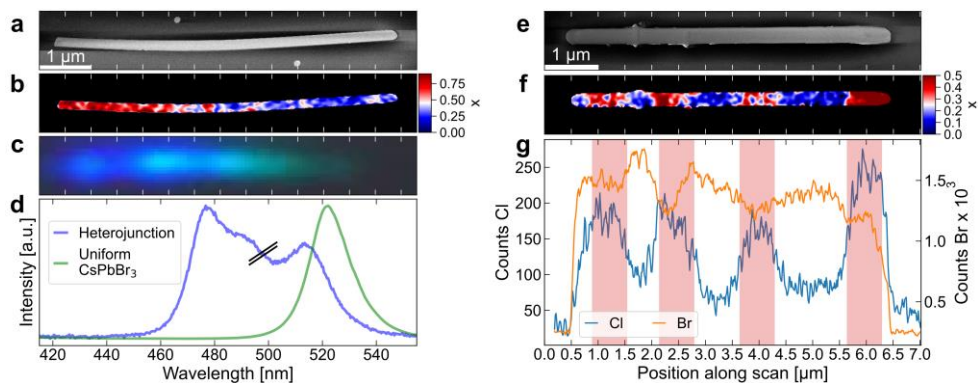


**Figure 4.13 SEM, PL, and EDS characterisation of heterojunction  $\text{CsPbBr}_3/\text{CsPb}(\text{Br}_{1-x}\text{Cl}_x)_3$  nanowires**

**a-d** SEM image, EDS map, PL microscopy image, and PL spectrum of one single heterojunction  $\text{CsPbBr}_3/\text{CsPb}(\text{Br}_{1-x}\text{Cl}_x)_3$  NW. Since a focused laser was used for PL excitation in **d**, the blue segment of the NW is excited more strongly than the green segment. The intensity is therefore not accurate, as indicated by the black bars. Likewise, the emission from the pure  $\text{CsPbBr}_3$  NW has been scaled down. For the true PL intensity relationship at uniform excitation, compare Figure 4.11c. **e-g** SEM image, EDS map, and EDS line profile of a barcode-junction  $\text{CsPbBr}_3/\text{CsPb}(\text{Br}_{1-x}\text{Cl}_x)_3$  NW. Red-shaded regions in NW indicate where the windows were written into the PMMA, according to the EBL mask. Reproduced from paper V.

## 5 Conclusions and Outlook

The work presented in this thesis has demonstrated advancements in single NW optoelectronics and shown cutting-edge devices for both the InP and CsPbBr<sub>3</sub> MHP material systems.

The work on InP NWs presented in papers I and II illustrates what level of sophistication is ultimately possible with single NW devices and state-of-the art, fine-tuned processing methods. This work establishes how single vertical InP NW devices can be reliably fabricated with good diode properties. The versatility of these devices is demonstrated by how the single NW devices work adequately as both a solar cell, photodetector, and LED without any application-specific optimisation of the materials. In paper II, we then demonstrate that these novel devices enable unique measurements like the direct imaging of an optical focus close to the diffraction limit with a detector much smaller than the wavelength of light.

In the future, these devices can be optimised for the individual application. As revealed by the modelling, it is possible to create NW detectors which are optimised for both absorption and resolution, although this is also dependent on the intended wavelength. Interesting further measurements could be undertaken when looking at more well-defined optical foci, as well as optical phenomena which are densely structured. Further, the axial structure of the III-V NWs can be optimised for LED applications, creating an incredibly high-resolution display as opposed to a photodetector.

The work on MHP NWs presented in papers III through VI represents major progress in nanoprocessing for MHP nanomaterials. The solvent-based growth displayed in papers III and VI highlights how MHP nanomaterials can offer a great cost advantage when compared to the complicated MOCVD growth necessary for the InP NWs. The lithography method presented in paper IV shows that nanoscale engineering is indeed possible for MHPs, despite their high solubility in polar solvents. In fact, as demonstrated by the anion exchange process in paper V, we can capitalise on the unique properties of MHPs to enable post-growth modification at the nanoscale. In combination, these two methods bring MHP nanostructures much closer to the complexity possible with established semiconductors.

Furthermore, by using these methods, major improvements may be made in the understanding of MHP materials by taking advantage of the NW geometry as a lower-dimensional test system. The methods presented in this thesis offer multiple interesting paths of exploration. Studies of ion migration benefit from the reduced dimensionality of NWs due to the much-simplified diffusion equations, which could help address some fundamental questions about MHPs. At the same time, the EBL process opens the path for many different metallisations which may unlock interesting electrical properties in the finished devices, as contact engineering has always been an important part of device design. The anion exchange processes demonstrated in paper V show that heterojunctions can be produced with possible applications as  $pn$ -junctions, emissive layers for MHP LEDs, or at low levels as a sort of “doping”. Much further study, based on the devices enabled by the research demonstrated here, is warranted and already underway [157, 164, 165].

## 6 References

- [1] E. Ertekin, P. A. Greaney, D. C. Chrzan, and T. D. Sands, "Equilibrium limits of coherency in strained nanowire heterostructures", *Journal of Applied Physics* **2005**, vol. 97, no. 11, doi: <http://doi.org/10.1063/1.1903106>
- [2] F. Glas, "Critical dimensions for the plastic relaxation of strained axial heterostructures in free-standing nanowires", *Physical Review B* **2006**, vol. 74, no. 12, doi: <http://doi.org/10.1103/PhysRevB.74.121302>
- [3] S. Andric, F. Lindelow, L. O. Fhager, E. Lind, and L.-E. Wernersson, "Lateral III–V Nanowire MOSFETs in Low-Noise Amplifier Stages", *IEEE Transactions on Microwave Theory and Techniques* **2022**, vol. 70, no. 2, pp. 1284-1291, doi: <http://doi.org/10.1109/tmmt.2021.3124088>
- [4] G. Rangasamy, Z. Zhu, and L.-E. Wernersson, "High Current Density Vertical Nanowire TFETs With  $I_{60} > 1 \mu\text{A}/\mu\text{m}$ ", *IEEE Access* **2023**, vol. 11, pp. 95692-95696, doi: <http://doi.org/10.1109/access.2023.3310253>
- [5] K. Tomioka, M. Yoshimura, and T. Fukui, "A III-V nanowire channel on silicon for high-performance vertical transistors", *Nature* **2012**, vol. 488, no. 7410, pp. 189-92, doi: <http://doi.org/10.1038/nature11293>
- [6] L. J. Lauhon, M. S. Gudiksen, D. Wang, and C. M. Lieber, "Epitaxial core-shell and core-multishell nanowire heterostructures", *Nature* **2002**, vol. 420, no. 6911, pp. 57-61, doi: <http://doi.org/10.1038/nature01141>
- [7] Z. Zhang, N. Lamers, C. Sun, C. Hetherington, I. G. Scheblykin, and J. Wallentin, "Free-Standing Metal Halide Perovskite Nanowire Arrays with Blue-Green Heterostructures", *Nano Letters* **2022**, vol. 22, no. 7, pp. 2941-2947, doi: <http://doi.org/10.1021/acs.nanolett.2c00137>
- [8] A. B. Greytak, C. J. Barrelet, Y. Li, and C. M. Lieber, "Semiconductor nanowire laser and nanowire waveguide electro-optic modulators", *Applied Physics Letters* **2005**, vol. 87, no. 15, doi: <http://doi.org/10.1063/1.2089157>
- [9] C. J. Barrelet, A. B. Greytak, and C. M. Lieber, "Nanowire photonic circuit elements", *Nano Letters* **2004**, vol. 4, no. 10, pp. 1981-1985, doi: <http://doi.org/10.1021/nl048739k>
- [10] X. Guo, Y. Ying, and L. Tong, "Photonic nanowires: from subwavelength waveguides to optical sensors", *Accounts of Chemical Research* **2014**, vol. 47, no. 2, pp. 656-66, doi: <http://doi.org/10.1021/ar400232h>
- [11] N. Anttu, "Absorption of light in a single vertical nanowire and a nanowire array", *Nanotechnology* **2019**, vol. 30, no. 10, p. 104004, doi: <http://doi.org/10.1088/1361-6528/aafa5c>

- [12] N. Anttu, A. Abrand, D. Asoli, M. Heurlin, I. Åberg, L. Samuelson, and M. Borgström, "Absorption of light in InP nanowire arrays", *Nano Research* **2014**, vol. 7, no. 6, pp. 816-823, doi: <http://doi.org/10.1007/s12274-014-0442-y>
- [13] H. Park, Y. Dan, K. Seo, Y. J. Yu, P. K. Duane, M. Wober, and K. B. Crozier, "Filter-free image sensor pixels comprising silicon nanowires with selective color absorption", *Nano Letters* **2014**, vol. 14, no. 4, pp. 1804-9, doi: <http://doi.org/10.1021/nl404379w>
- [14] J. Goldberger, A. I. Hochbaum, R. Fan, and P. D. Yang, "Silicon vertically integrated nanowire field effect transistors", *Nano Letters* **2006**, vol. 6, no. 5, pp. 973-977, doi: <http://doi.org/10.1021/nl060166j>
- [15] N. Han, F. Wang, J. J. Hou, F. Xiu, S. Yip, A. T. Hui, T. Hung, and J. C. Ho, "Controllable p-n switching behaviors of GaAs nanowires via an interface effect", *ACS Nano* **2012**, vol. 6, no. 5, pp. 4428-33, doi: <http://doi.org/10.1021/nn3011416>
- [16] Y. Meng, Z. Lai, F. Li, W. Wang, S. Yip, Q. Quan, X. Bu, F. Wang, Y. Bao, T. Hosomi et al., "Perovskite Core-Shell Nanowire Transistors: Interfacial Transfer Doping and Surface Passivation", *ACS Nano* **2020**, vol. 14, no. 10, pp. 12749-12760, doi: <http://doi.org/10.1021/acsnano.0c03101>
- [17] C. Thelander, T. Mårtensson, M. T. Björk, B. J. Ohlsson, M. W. Larsson, L. R. Wallenberg, and L. Samuelson, "Single-electron transistors in heterostructure nanowires", *Applied Physics Letters* **2003**, vol. 83, no. 10, pp. 2052-2054, doi: <http://doi.org/10.1063/1.1606889>
- [18] J. Wallentin, M. Ek, L. R. Wallenberg, L. Samuelson, and M. T. Borgström, "Electron trapping in InP nanowire FETs with stacking faults", *Nano Letters* **2012**, vol. 12, no. 1, pp. 151-5, doi: <http://doi.org/10.1021/nl203213d>
- [19] E. D. Minot, F. Kelkensberg, M. van Kouwen, J. A. van Dam, L. P. Kouwenhoven, V. Zwiller, M. T. Borgström, O. Wunnicke, M. A. Verheijen, and E. P. Bakkers, "Single quantum dot nanowire LEDs", *Nano Letters* **2007**, vol. 7, no. 2, pp. 367-71, doi: <http://doi.org/10.1021/nl062483w>
- [20] X. Dai, A. Messanvi, H. Zhang, C. Durand, J. Eymery, C. Bougerol, F. H. Julien, and M. Tchernycheva, "Flexible Light-Emitting Diodes Based on Vertical Nitride Nanowires", *Nano Lett* **2015**, vol. 15, no. 10, pp. 6958-64, doi: <http://doi.org/10.1021/acs.nanolett.5b02900>
- [21] C. Hahn, Z. Zhang, A. Fu, C. H. Wu, Y. J. Hwang, D. J. Gargas, and P. Yang, "Epitaxial growth of InGaN nanowire arrays for light emitting diodes", *ACS Nano* **2011**, vol. 5, no. 5, pp. 3970-6, doi: <http://doi.org/10.1021/nn200521r>
- [22] K. Adham, Y. Zhao, P. Kivisaari, and M. T. Borgström, "Characterization of n-doped branches in nanotree LEDs", *Energy Advances* **2024**, vol. 3, no. 12, pp. 2922-2928, doi: <http://doi.org/10.1039/d4ya00414k>
- [23] Y. Zhao, K. Adham, D. Hessman, and M. T. Borgström, "Direct band gap white light emission from charge carrier diffusion induced nanowire light-emitting diodes", *Nano Energy* **2024**, vol. 132, doi: <http://doi.org/10.1016/j.nanoen.2024.110400>
- [24] H. Jeddi, K. Adham, Y. Zhao, B. Witzigmann, F. Romer, M. Bermeo, M. T. Borgström, and H. Pettersson, "Enhanced LWIR response of InP/InAsP quantum discs-in-nanowire array photodetectors by photogating and ultra-thin ITO

- contacts", *Nanotechnology* **2024**, vol. 35, no. 21, doi: <http://doi.org/10.1088/1361-6528/ad2bd0>
- [25] H. Jeddi, B. Witzigmann, K. Adham, L. Hrachowina, M. T. Borgström, and H. Pettersson, "Spectrally Tunable Broadband Gate-All-Around InAsP/InP Quantum Discs-in-Nanowire Array Phototransistors with a High Gain-Bandwidth Product", *ACS Photonics* **2023**, vol. 10, no. 6, pp. 1748-1755, doi: <http://doi.org/10.1021/acsp Photonics.2c02024>
- [26] L. Chayanun, L. Hrachowina, A. Bjorling, M. T. Borgström, and J. Wallentin, "Direct Three-Dimensional Imaging of an X-ray Nanofocus Using a Single 60 nm Diameter Nanowire Device", *Nano Letters* **2020**, vol. 20, no. 11, pp. 8326-8331, doi: <http://doi.org/10.1021/acs.nanolett.0c03477>
- [27] L. Chayanun, S. Hammarberg, H. Dierks, G. Otnes, A. Björling, M. T. Borgström, and J. Wallentin, "Combining Nanofocused X-Rays with Electrical Measurements at the NanoMAX Beamline", *Crystals* **2019**, vol. 9, no. 8, doi: <http://doi.org/10.3390/cryst9080432>
- [28] C. Gutsche, A. Lysov, D. Braam, I. Regolin, G. Keller, Z. A. Li, M. Geller, M. Spasova, W. Prost, and F. J. Tegude, "n-GaAs/InGaP/p-GaAs Core-Multishell Nanowire Diodes for Efficient Light-to-Current Conversion", *Advanced Functional Materials* **2011**, vol. 22, no. 5, pp. 929-936, doi: <http://doi.org/10.1002/adfm.201101759>
- [29] M. Zapf, M. Ritzer, L. Liborius, A. Johannes, M. Hafermann, S. Schonherr, J. Segura-Ruiz, G. Martinez-Criado, W. Prost, and C. Ronning, "Hot electrons in a nanowire hard X-ray detector", *Nature Communications* **2020**, vol. 11, no. 1, p. 4729, doi: <http://doi.org/10.1038/s41467-020-18384-x>
- [30] W. Deng, L. Huang, X. Xu, X. Zhang, X. Jin, S. T. Lee, and J. Jie, "Ultrahigh-Responsivity Photodetectors from Perovskite Nanowire Arrays for Sequentially Tunable Spectral Measurement", *Nano Letters* **2017**, vol. 17, no. 4, pp. 2482-2489, doi: <http://doi.org/10.1021/acs.nanolett.7b00166>
- [31] Y. Guan, C. Zhang, Z. Liu, Y. Zhao, A. Ren, J. Liang, F. Hu, and Y. S. Zhao, "Single-Crystalline Perovskite p-n Junction Nanowire Arrays for Ultrasensitive Photodetection", *Adv Mater* **2022**, vol. 34, no. 35, p. e2203201, doi: <http://doi.org/10.1002/adma.202203201>
- [32] K. D. M. Rao, M. Hossain, Umesh, A. Roy, A. Ghosh, G. S. Kumar, P. Moitra, T. Kamilya, S. Acharya, and S. Bhattacharya, "Transparent, flexible MAPbI<sub>3</sub> perovskite microwire arrays passivated with ultra-hydrophobic supramolecular self-assembly for stable and high-performance photodetectors", *Nanoscale* **2020**, vol. 12, no. 22, pp. 11986-11996, doi: <http://doi.org/10.1039/d0nr01394c>
- [33] T. Yang, Y. Zheng, Z. Du, W. Liu, Z. Yang, F. Gao, L. Wang, K. C. Chou, X. Hou, and W. Yang, "Superior Photodetectors Based on All-Inorganic Perovskite CsPbI<sub>3</sub> Nanorods with Ultrafast Response and High Stability", *ACS Nano* **2018**, vol. 12, no. 2, pp. 1611-1617, doi: <http://doi.org/10.1021/acsnano.7b08201>
- [34] Q. Zhou, J. G. Park, R. Nie, A. K. Thokchom, D. Ha, J. Pan, S. I. Seok, and T. Kim, "Nanochannel-Assisted Perovskite Nanowires: From Growth Mechanisms to Photodetector Applications", *ACS Nano* **2018**, vol. 12, no. 8, pp. 8406-8414, doi: <http://doi.org/10.1021/acsnano.8b03826>

- [35] A. C. Farrell, P. Senanayake, X. Meng, N. Y. Hsieh, and D. L. Huffaker, "Diode Characteristics Approaching Bulk Limits in GaAs Nanowire Array Photodetectors", *Nano Letters* **2017**, vol. 17, no. 4, pp. 2420-2425, doi: <http://doi.org/10.1021/acs.nanolett.7b00024>
- [36] M. H. Huang, S. Mao, H. Feick, H. Yan, Y. Wu, H. Kind, E. Weber, R. Russo, and P. Yang, "Room-temperature ultraviolet nanowire nanolasers", *Science* **2001**, vol. 292, no. 5523, pp. 1897-9, doi: <http://doi.org/10.1126/science.1060367>
- [37] D. Ren, L. Ahtapodov, J. S. Nilsen, J. Yang, A. Gustafsson, J. Huh, G. J. Conibeer, A. T. J. van Helvoort, B. O. Fimland, and H. Weman, "Single-Mode Near-Infrared Lasing in a GaAsSb-Based Nanowire Superlattice at Room Temperature", *Nano Letters* **2018**, vol. 18, no. 4, pp. 2304-2310, doi: <http://doi.org/10.1021/acs.nanolett.7b05015>
- [38] X. X. He, P. Liu, S. N. Wu, Q. Liao, J. N. Yao, and H. B. Fu, "Multi-color perovskite nanowire lasers through kinetically controlled solution growth followed by gas-phase halide exchange", *Journal of Materials Chemistry C* **2017**, vol. 5, no. 48, pp. 12707-12713, doi: <http://doi.org/10.1039/c7tc03939e>
- [39] D. I. Markina, S. S. Anoshkin, M. A. Masharin, S. A. Khubezhov, I. Tzibizov, D. Dolgintsev, I. N. Terterov, S. V. Makarov, and A. P. Pushkarev, "Perovskite Nanowire Laser for Hydrogen Chloride Gas Sensing", *ACS Nano* **2023**, vol. 17, no. 2, pp. 1570-1582, doi: <http://doi.org/10.1021/acs.nano.2c11013>
- [40] L. Hrachowina, Y. Chen, E. Barrigon, R. Wallenberg, and M. T. Borgström, "Realization of axially defined GaInP/InP/InAsP triple-junction photovoltaic nanowires for high-performance solar cells", *Materials Today Energy* **2022**, vol. 27, doi: <http://doi.org/10.1016/j.mtener.2022.101050>
- [41] L. Hrachowina, Y. Zhang, A. Saxena, G. Siefer, E. Barrigon, and M. T. Borgström, "Development and Characterization of a bottom-up InP Nanowire Solar Cell with 16.7% Efficiency", in *2020 47th IEEE Photovoltaic Specialists Conference (PVSC)*, **2020**, pp. 1754-1756, doi: <http://doi.org/10.1109/PVSC45281.2020.9300394>
- [42] C. Colombo, M. Heiss, M. Grätzel, and A. F. I. Morral, "Gallium arsenide p-i-n radial structures for photovoltaic applications", *Applied Physics Letters* **2009**, vol. 94, no. 17, doi: <http://doi.org/10.1063/1.3125435>
- [43] J. Wallentin, N. Anttu, D. Asoli, M. Huffman, I. Aberg, M. H. Magnusson, G. Siefer, P. Fuss-Kailuweit, F. Dimroth, B. Witzigmann et al., "InP nanowire array solar cells achieving 13.8% efficiency by exceeding the ray optics limit", *Science* **2013**, vol. 339, no. 6123, pp. 1057-60, doi: <http://doi.org/10.1126/science.1230969>
- [44] D. Li, Y. Meng, Y. Zheng, P. Xie, X. Kang, Z. Lai, X. Bu, W. Wang, W. Wang, F. Chen et al., "Surface Energy-Mediated Self-Catalyzed CsPbBr<sub>3</sub> Nanowires for Phototransistors", *Advanced Electronic Materials* **2022**, vol. 8, no. 12, doi: <http://doi.org/10.1002/aelm.202200727>
- [45] P. Guo, D. Liu, X. Shen, Q. Lv, Y. Wu, Q. Yang, P. Li, Y. Hao, J. C. Ho, and K. M. Yu, "On-wire axial perovskite heterostructures for monolithic dual-wavelength laser", *Nano Energy* **2022**, vol. 92, p. 106778, doi: <http://doi.org/10.1016/j.nanoen.2021.106778>



- [46] Y. Meng, C. Lan, F. Li, S. Yip, R. Wei, X. Kang, X. Bu, R. Dong, H. Zhang, and J. C. Ho, "Direct Vapor-Liquid-Solid Synthesis of All-Inorganic Perovskite Nanowires for High-Performance Electronics and Optoelectronics", *ACS Nano* **2019**, vol. 13, no. 5, pp. 6060-6070, doi: <http://doi.org/10.1021/acs.nano.9b02379>
- [47] J. Chen, Y. Fu, L. Samad, L. Dang, Y. Zhao, S. Shen, L. Guo, and S. Jin, "Vapor-Phase Epitaxial Growth of Aligned Nanowire Networks of Cesium Lead Halide Perovskites ( $\text{CsPbX}_3$ , X = Cl, Br, I)", *Nano Letters* **2017**, vol. 17, no. 1, pp. 460-466, doi: <http://doi.org/10.1021/acs.nanolett.6b04450>
- [48] Y. Wang, X. Sun, R. Shivanna, Y. Yang, Z. Chen, Y. Guo, G. C. Wang, E. Wertz, F. Deschler, Z. Cai et al., "Photon Transport in One-Dimensional Incommensurately Epitaxial  $\text{CsPbX}_3$  Arrays", *Nano Letters* **2016**, vol. 16, no. 12, pp. 7974-7981, doi: <http://doi.org/10.1021/acs.nanolett.6b04297>
- [49] E. Oksenberg, A. Merdasa, L. Houben, I. Kaplan-Ashiri, A. Rothman, I. G. Scheblykin, E. L. Unger, and E. Joselevich, "Large lattice distortions and size-dependent bandgap modulation in epitaxial halide perovskite nanowires", *Nature Communications* **2020**, vol. 11, no. 1, p. 489, doi: <http://doi.org/10.1038/s41467-020-14365-2>
- [50] D. Zhang, S. W. Eaton, Y. Yu, L. Dou, and P. Yang, "Solution-Phase Synthesis of Cesium Lead Halide Perovskite Nanowires", *Journal of the American Chemical Society* **2015**, vol. 137, no. 29, pp. 9230-3, doi: <http://doi.org/10.1021/jacs.5b05404>
- [51] M. Gao, H. Liu, S. Yu, S. Louisia, Y. Zhang, D. P. Nenon, A. P. Alivisatos, and P. Yang, "Scaling Laws of Exciton Recombination Kinetics in Low Dimensional Halide Perovskite Nanostructures", *Journal of the American Chemical Society* **2020**, vol. 142, no. 19, pp. 8871-8879, doi: <http://doi.org/10.1021/jacs.0c02000>
- [52] Y. Fu, H. Zhu, A. W. Schrader, D. Liang, Q. Ding, P. Joshi, L. Hwang, X. Y. Zhu, and S. Jin, "Nanowire Lasers of Formamidinium Lead Halide Perovskites and Their Stabilized Alloys with Improved Stability", *Nano Letters* **2016**, vol. 16, no. 2, pp. 1000-8, doi: <http://doi.org/10.1021/acs.nanolett.5b04053>
- [53] A. B. Wong, M. Lai, S. W. Eaton, Y. Yu, E. Lin, L. Dou, A. Fu, and P. Yang, "Growth and Anion Exchange Conversion of  $\text{CH}_3\text{NH}_3\text{PbX}_3$  Nanorod Arrays for Light-Emitting Diodes", *Nano Letters* **2015**, vol. 15, no. 8, pp. 5519-24, doi: <http://doi.org/10.1021/acs.nanolett.5b02082>
- [54] M. L. Lai, Q. Kong, C. G. Bischak, Y. Yu, L. T. Dou, S. W. Eaton, N. S. Ginsberg, and P. D. Yang, "Structural, optical, and electrical properties of phase-controlled cesium lead iodide nanowires", *Nano Research* **2017**, vol. 10, no. 4, pp. 1107-1114, doi: <http://doi.org/10.1007/s12274-016-1415-0>
- [55] S. Z. Oener, P. Khoram, S. Brittan, S. A. Mann, Q. Zhang, Z. Fan, S. W. Boettcher, and E. C. Garnett, "Perovskite Nanowire Extrusion", *Nano Letters* **2017**, vol. 17, no. 11, pp. 6557-6563, doi: <http://doi.org/10.1021/acs.nanolett.7b02213>
- [56] S. Ma, S. H. Kim, B. Jeong, H. C. Kwon, S. C. Yun, G. Jang, H. Yang, C. Park, D. Lee, and J. Moon, "Strain-Mediated Phase Stabilization: A New Strategy for Ultrastable  $\alpha\text{-CsPbI}_3$  Perovskite by Nanoconfined Growth", *Small* **2019**, vol. 15, no. 21, p. e1900219, doi: <http://doi.org/10.1002/sml.201900219>

- [57] Y. Fu, S. Poddar, B. Ren, Y. Xie, Q. Zhang, D. Zhang, B. Cao, Y. Tang, Y. Ding, X. Qiu et al., "Strongly Quantum-Confined Perovskite Nanowire Arrays for Color-Tunable Blue-Light-Emitting Diodes", *ACS Nano* **2022**, vol. 16, no. 5, pp. 8388-8398, doi: <http://doi.org/10.1021/acsnano.2c02795>
- [58] D. Q. Zhang, Q. P. Zhang, B. T. Ren, Y. D. Zhu, M. Abdellah, Y. Fu, B. Cao, C. Wang, L. L. Gu, Y. C. Ding et al., "Large-scale planar and spherical light-emitting diodes based on arrays of perovskite quantum wires", *Nature Photonics* **2022**, vol. 16, no. 4, pp. 284-+, doi: <http://doi.org/10.1038/s41566-022-00978-0>
- [59] P. Krogstrup, H. I. Jørgensen, M. Heiss, O. Demichel, J. V. Holm, M. Aagesen, J. Nygard, and A. Fontcuberta i Morral, "Single-nanowire solar cells beyond the Shockley–Queisser limit", *Nature Photonics* **2013**, vol. 7, no. 4, pp. 306-310, doi: <http://doi.org/10.1038/nphoton.2013.32>
- [60] Z. Li, L. Li, F. Wang, L. Xu, Q. Gao, A. Alabadla, K. Peng, K. Vora, H. T. Hattori, H. H. Tan et al., "Investigation of light-matter interaction in single vertical nanowires in ordered nanowire arrays", *Nanoscale* **2022**, vol. 14, no. 9, pp. 3527-3536, doi: <http://doi.org/10.1039/d1nr08088a>
- [61] J. Harwell, J. Burch, A. Fikouras, M. C. Gather, A. Di Falco, and I. D. W. Samuel, "Patterning Multicolor Hybrid Perovskite Films via Top-Down Lithography", *ACS Nano* **2019**, vol. 13, no. 4, pp. 3823-3829, doi: <http://doi.org/10.1021/acsnano.8b09592>
- [62] C. H. Lin, B. Cheng, T. Y. Li, J. R. D. Retamal, T. C. Wei, H. C. Fu, X. Fang, and J. H. He, "Orthogonal Lithography for Halide Perovskite Optoelectronic Nanodevices", *ACS Nano* **2019**, vol. 13, no. 2, pp. 1168-1176, doi: <http://doi.org/10.1021/acsnano.8b05859>
- [63] E. L. Unger, O. Shargaieva, S. Braunger, and P. Docampo, "CHAPTER 4 Solution-processed Solar Cells: Perovskite Solar Cells," in *Solar Energy Capture Materials: The Royal Society of Chemistry*, **2019**, pp. 153-192.
- [64] Y. Zhang, T. D. Siegler, C. J. Thomas, M. K. Abney, T. Shah, A. De Gorostiza, R. M. Greene, and B. A. Korgel, "A “Tips and Tricks” Practical Guide to the Synthesis of Metal Halide Perovskite Nanocrystals", *Chemistry of Materials* **2020**, vol. 32, no. 13, pp. 5410-5423, doi: <http://doi.org/10.1021/acs.chemmater.0c01735>
- [65] D. Lyashenko, A. Perez, and A. Zakhidov, "High-resolution patterning of organohalide lead perovskite pixels for photodetectors using orthogonal photolithography", *Physica Status Solidi A* **2017**, vol. 214, no. 1, p. 1600302, doi: <http://doi.org/10.1002/pssa.201600302>
- [66] L. Dou, M. Lai, C. S. Kley, Y. Yang, C. G. Bischak, D. Zhang, S. W. Eaton, N. S. Ginsberg, and P. Yang, "Spatially resolved multicolor CsPbX<sub>3</sub> nanowire heterojunctions via anion exchange", *Proceedings of the National Academy of Sciences of the United States of America* **2017**, vol. 114, no. 28, pp. 7216-7221, doi: <http://doi.org/10.1073/pnas.1703860114>
- [67] N. Zhang, W. Sun, S. P. Rodrigues, K. Wang, Z. Gu, S. Wang, W. Cai, S. Xiao, and Q. Song, "Highly Reproducible Organometallic Halide Perovskite Microdevices based on Top-Down Lithography", *Advanced Materials* **2017**, vol. 29, no. 15, p. 1606205, doi: <http://doi.org/10.1002/adma.201606205>

- [68] B. E. A. Saleh and M. C. Teich, *Fundamentals of Photonics*. Somerset, USA: John Wiley & Sons, Incorporated, **2013**.
- [69] G. Nedelcu, L. Protesescu, S. Yakunin, M. I. Bodnarchuk, M. J. Grotevent, and M. V. Kovalenko, "Fast Anion-Exchange in Highly Luminescent Nanocrystals of Cesium Lead Halide Perovskites ( $\text{CsPbX}_3$ ,  $X = \text{Cl, Br, I}$ )", *Nano Letters* **2015**, vol. 15, no. 8, pp. 5635-40, doi: <http://doi.org/10.1021/acs.nanolett.5b02404>
- [70] S. M. Sze and K. N. Kwok, *Physics of Semiconductor Devices*. Wiley-Interscience, **2007**.
- [71] U. W. Pohl, *Epitaxy of Semiconductors* (Graduate Texts in Physics). **2013**.
- [72] P. Y. C. Yu, Manuel, *Fundamentals of Semiconductors* (Graduate Texts in Physics). **2010**.
- [73] W. Shockley, "The Theory of p-n Junctions in Semiconductors and p-n Junction Transistors", *Bell System Technical Journal* **1949**, vol. 28, no. 3, pp. 435-489, doi: <http://doi.org/10.1002/j.1538-7305.1949.tb03645.x>
- [74] C. T. Sah, R. N. Noyce, and W. Shockley, "Carrier Generation and Recombination in P-N Junctions and P-N Junction Characteristics", *Proceedings of the Institute of Radio Engineers* **1957**, vol. 45, no. 9, pp. 1228-1243, doi: <http://doi.org/10.1109/Jrproc.1957.278528>
- [75] E. Amerling, H. P. Lu, B. W. Larson, A. E. Maughan, A. Phillips, E. Lafalce, L. Whittaker-Brooks, J. J. Berry, M. C. Beard, Z. V. Vardeny et al., "A Multi-Dimensional Perspective on Electronic Doping in Metal Halide Perovskites", *ACS Energy Letters* **2021**, vol. 6, no. 3, pp. 1104-1123, doi: <http://doi.org/10.1021/acsenerylett.0c02476>
- [76] W. Shockley and W. T. Read, "Statistics of the Recombinations of Holes and Electrons", *Physical Review* **1952**, vol. 87, no. 5, pp. 835-842, doi: <http://doi.org/10.1103/PhysRev.87.835>
- [77] R. N. Hall, "Electron-Hole Recombination in Germanium", *Physical Review* **1952**, vol. 87, no. 2, pp. 387-387, doi: <http://doi.org/10.1103/PhysRev.87.387>
- [78] B. M. Kayes, H. Nie, R. Twist, S. G. Spruytte, F. Reinhardt, I. C. Kizilyalli, and G. S. Higashi, "27.6% Conversion efficiency, a new record for single-junction solar cells under 1 sun illumination", in *2011 37th IEEE Photovoltaic Specialists Conference*, **2011**, pp. 000004-000008, doi: <http://doi.org/10.1109/PVSC.2011.6185831>
- [79] T. Chen, P. Catrysse, A. El Gamal, and B. Wandell, "How small should pixel size be?", in *Electronic Imaging*, **2000**, vol. 3965: SPIE, doi: <http://doi.org/10.1117/12.385463>
- [80] F. Xiao, J. Farrell, P. Catrysse, and B. Wandell, "Mobile imaging: the big challenge of the small pixel", in *IS&T/SPIE Electronic Imaging*, **2009**, vol. 7250: SPIE, doi: <http://doi.org/10.1117/12.806616>
- [81] B. J. Lechner, F. J. Marlowe, E. O. Nester, and J. Tults, "Liquid Crystal Matrix Displays", *Proceedings of the Institute of Electrical and Electronics Engineers* **1971**, vol. 59, no. 11, pp. 1566-&, doi: <http://doi.org/10.1109/Proc.1971.8489>
- [82] E. S. Eid, "Study of limitations on pixel size of very high resolution image sensors", in *Proceedings of the Eighteenth National Radio Science Conference*.

- NRSC'2001 (IEEE Cat. No.01EX462), **2001**, vol. 1, pp. 15-28 vol.1, doi: <http://doi.org/10.1109/NRSC.2001.929154>
- [83] R. S. Wagner and W. C. Ellis, "Vapor-Liquid-Solid Mechanism of Single Crystal Growth", *Applied Physics Letters* **1964**, vol. 4, no. 5, pp. 89-90, doi: <http://doi.org/10.1063/1.1753975>
- [84] Y. Wu and P. Yang, "Direct Observation of Vapor-Liquid-Solid Nanowire Growth", *Journal of the American Chemical Society* **2001**, vol. 123, no. 13, pp. 3165-3166, doi: <http://doi.org/10.1021/ja0059084>
- [85] H. Temkin, B. V. Dutt, and W. A. Bonner, "Photoluminescence study of native defects in InP", *Applied Physics Letters* **1981**, vol. 38, no. 6, pp. 431-433, doi: <http://doi.org/10.1063/1.92386>
- [86] G. Hirt, D. Hofmann, F. Mosel, N. Schäfer, and G. Müller, "Compensation mechanisms in nominally undoped semi-insulating InP and comparison with undoped InP grown under stoichiometry control", *Journal of Electronic Materials* **1991**, vol. 20, no. 12, pp. 1065-1068, doi: <http://doi.org/10.1007/bf03030208>
- [87] D. Hausmann, J. Becker, S. Wang, and R. G. Gordon, "Rapid vapor deposition of highly conformal silica nanolaminates", *Science* **2002**, vol. 298, no. 5592, pp. 402-6, doi: <http://doi.org/10.1126/science.1073552>
- [88] L. Hrachowina, X. S. Zou, Y. Chen, Y. W. Zhang, E. Barrigón, A. Yartsev, and M. T. Borgström, "Imaging the influence of oxides on the electrostatic potential of photovoltaic InP nanowires", *Nano Research* **2021**, vol. 14, no. 11, pp. 4087-4092, doi: <http://doi.org/10.1007/s12274-021-3344-9>
- [89] Y. C. Wenas, S. Mokkapati, H. H. Tan, and C. Jagadish, "Extremely high short-circuit current density in vertical single nanowire solar cells", in *2014 Conference on Optoelectronic and Microelectronic Materials & Devices*, **2014**, pp. 77-78, doi: <http://doi.org/10.1109/COMMAD.2014.7038656>
- [90] W. Shockley and H. J. Queisser, "Detailed Balance Limit of Efficiency of p-n Junction Solar Cells", *Journal of Applied Physics* **1961**, vol. 32, no. 3, pp. 510-519, doi: <http://doi.org/10.1063/1.1736034>
- [91] N. M. Shmidt, "INDIUM PHOSPHIDE (InP)," in *Handbook Series on Semiconductor Parameters*, **1996**, pp. 169-190.
- [92] Y. P. Varshni, "Temperature dependence of the energy gap in semiconductors", *Physica* **1967**, vol. 34, no. 1, pp. 149-154, doi: [http://doi.org/10.1016/0031-8914\(67\)90062-6](http://doi.org/10.1016/0031-8914(67)90062-6)
- [93] A. Jash, A. Yangui, S. Lehmann, I. G. Scheblykin, K. A. Dick, A. Gustafsson, and M. E. Pistol, "Time-resolved photoluminescence studies of single interface wurtzite/zincblende heterostructured InP nanowires", *Applied Physics Letters* **2022**, vol. 120, no. 11, doi: <http://doi.org/10.1063/5.0083159>
- [94] A. De and C. E. Pryor, "Predicted band structures of III-V semiconductors in the wurtzite phase", *Physical Review B* **2010**, vol. 81, no. 15, doi: <http://doi.org/10.1103/PhysRevB.81.155210>
- [95] A. Mishra, L. V. Titova, T. B. Hoang, H. E. Jackson, L. M. Smith, J. M. Yarrison-Rice, Y. Kim, H. J. Joyce, Q. Gao, H. H. Tan et al., "Polarization and temperature dependence of photoluminescence from zincblende and wurtzite InP nanowires",

*Applied Physics Letters* **2007**, vol. 91, no. 26, doi:

<http://doi.org/10.1063/1.2828034>

- [96] J. Wallentin, K. Mergenthaler, M. Ek, L. R. Wallenberg, L. Samuelson, K. Deppert, M. E. Pistol, and M. T. Borgström, "Probing the wurtzite conduction band structure using state filling in highly doped InP nanowires", *Nano Letters* **2011**, vol. 11, no. 6, pp. 2286-90, doi: <http://doi.org/10.1021/nl200492g>
- [97] H. H. Solak, C. Dais, and F. Clube, "Displacement Talbot lithography: a new method for high-resolution patterning of large areas", *Optics Express* **2011**, vol. 19, no. 11, pp. 10686-91, doi: <http://doi.org/10.1364/OE.19.010686>
- [98] B. Hecht, B. Sick, U. P. Wild, V. Deckert, R. Zenobi, O. J. F. Martin, and D. W. Pohl, "Scanning near-field optical microscopy with aperture probes: Fundamentals and applications", *Journal of Chemical Physics* **2000**, vol. 112, no. 18, pp. 7761-7774, doi: <http://doi.org/10.1063/1.481382>
- [99] B. H. Jia, X. S. Gan, and M. Gu, "Direct observation of a pure focused evanescent field of a high numerical aperture objective lens by scanning near-field optical microscopy", *Applied Physics Letters* **2005**, vol. 86, no. 13, doi: <http://doi.org/10.1063/1.1886250>
- [100] G. Brost, P. D. Horn, and A. Abtahi, "Convenient spatial profiling of pulsed laser beams", *Applied Optics* **1985**, vol. 24, no. 1, pp. 38-40, doi: <http://doi.org/10.1364/ao.24.000038>
- [101] M. A. de Araujo, R. Silva, E. de Lima, D. P. Pereira, and P. C. de Oliveira, "Measurement of Gaussian laser beam radius using the knife-edge technique: improvement on data analysis", *Applied Optics* **2009**, vol. 48, no. 2, pp. 393-6, doi: <http://doi.org/10.1364/ao.48.000393>
- [102] J. M. Khosrofian and B. A. Garetz, "Measurement of a Gaussian laser beam diameter through the direct inversion of knife-edge data", *Applied Optics* **1983**, vol. 22, no. 21, p. 3406, doi: <http://doi.org/10.1364/ao.22.003406>
- [103] A. H. Firester, M. E. Heller, and P. Sheng, "Knife-edge scanning measurements of subwavelength focused light beams", *Applied Optics* **1977**, vol. 16, no. 7, pp. 1971-4, doi: <http://doi.org/10.1364/AO.16.001971>
- [104] A. E. Siegman, M. W. Sasnett, and T. F. Johnston, "Choice of Clip Levels for Beam Width Measurements Using Knife-Edge Techniques", *IEEE Journal of Quantum Electronics* **1991**, vol. 27, no. 4, pp. 1098-1104, doi: <http://doi.org/10.1109/3.83346>
- [105] J. J. Chapman, B. G. Norton, E. W. Streed, and D. Kielpinski, "An automated submicron beam profiler for characterization of high numerical aperture optics", *Review of Scientific Instruments* **2008**, vol. 79, no. 9, p. 095106, doi: <http://doi.org/10.1063/1.2991112>
- [106] X. S. Xie, L. Li, S. C. Wang, Z. X. Wang, and J. Y. Zhou, "Three-dimensional measurement of a tightly focused laser beam", *AIP Advances* **2013**, vol. 3, no. 2, doi: <http://doi.org/10.1063/1.4791764>
- [107] J. Trägårdh, K. Macrae, C. Travis, R. Amor, G. Norris, S. H. Wilson, G. L. Oppo, and G. McConnell, "A simple but precise method for quantitative measurement of the quality of the laser focus in a scanning optical microscope", *Journal of*

- Microscopy* **2015**, vol. 259, no. 1, pp. 66-73, doi:  
<http://doi.org/10.1111/jmi.12249>
- [108] D. K. Cohen, B. Little, and F. S. Luecke, "Techniques for measuring 1- $\mu$ m diam Gaussian beams", *Applied Optics* **1984**, vol. 23, no. 4, p. 637, doi:  
<http://doi.org/10.1364/ao.23.000637>
  - [109] M. B. Schneider and W. W. Webb, "Measurement of submicron laser beam radii", *Applied Optics* **1981**, vol. 20, no. 8, pp. 1382-8, doi:  
<http://doi.org/10.1364/AO.20.001382>
  - [110] T. Bauer, S. Orlov, U. Peschel, P. Banzer, and G. Leuchs, "Nanointerferometric amplitude and phase reconstruction of tightly focused vector beams", *Nature Photonics* **2013**, vol. 8, no. 1, pp. 23-27, doi:  
<http://doi.org/10.1038/nphoton.2013.289>
  - [111] H. Dierks, P. Stjärneblad, and J. Wallentin, "A versatile laboratory setup for high resolution X-ray phase contrast tomography and scintillator characterization", *Journal of X-Ray Science and Technology* **2023**, vol. 31, no. 1, pp. 1-12, doi:  
<http://doi.org/10.3233/XST-221294>
  - [112] International Organization for Standardization, *Lasers and laser-related equipment — Test methods for laser beam widths, divergence angles and beam propagation ratios — Part 1: Stigmatic and simple astigmatic beams*, **2021**.  
<https://www.iso.org/standard/77769.html>
  - [113] A. S. Shikoh and A. Polyakov, "A Quantitative Analysis of the Research Trends in Perovskite Solar Cells in 2009–2019", *Physica Status Solidi A* **2020**, vol. 217, no. 23, doi: <http://doi.org/10.1002/pssa.202000441>
  - [114] Y. Li, Y. Duan, J. Feng, Y. Sun, K. Wang, H. Li, H. Wang, Z. Zang, H. Zhou, D. Xu et al., "25.71 %-Efficiency FACsPbI<sub>3</sub> Perovskite Solar Cells Enabled by A Thiourea-based Isomer", *Angewandte Chemie International Edition* **2024**, vol. 63, no. 49, p. e202410378, doi: <http://doi.org/10.1002/anie.202410378>
  - [115] N. R. E. Laboratory. (2025). *Best Research-Cell Efficiency Chart*. Available:  
<https://www.nrel.gov/pv/cell-efficiency.html>
  - [116] Z. Li, T. R. Klein, D. H. Kim, M. J. Yang, J. J. Berry, M. F. A. M. van Hest, and K. Zhu, "Scalable fabrication of perovskite solar cells", *Nature Reviews Materials* **2018**, vol. 3, no. 4, p. 18017, Art. no. 18017, doi:  
<http://doi.org/10.1038/natrevmats.2018.17>
  - [117] A. Dey, J. Ye, A. De, E. Debroye, S. K. Ha, E. Bladt, A. S. Kshirsagar, Z. Wang, J. Yin, Y. Wang et al., "State of the Art and Prospects for Halide Perovskite Nanocrystals", *ACS Nano* **2021**, vol. 15, no. 7, pp. 10775-10981, doi:  
<http://doi.org/10.1021/acsnano.0c08903>
  - [118] Q. Zhang, D. Zhang, L. Gu, K. H. Tsui, S. Poddar, Y. Fu, L. Shu, and Z. Fan, "Three-Dimensional Perovskite Nanophotonic Wire Array-Based Light-Emitting Diodes with Significantly Improved Efficiency and Stability", *ACS Nano* **2020**, vol. 14, no. 2, pp. 1577-1585, doi: <http://doi.org/10.1021/acsnano.9b06663>
  - [119] Q. Zhang, M. M. Tavakoli, L. Gu, D. Zhang, L. Tang, Y. Gao, J. Guo, Y. Lin, S. F. Leung, S. Poddar et al., "Efficient metal halide perovskite light-emitting diodes with significantly improved light extraction on nanophotonic substrates", *Nature*



- Communications* **2019**, vol. 10, no. 1, p. 727, doi: <http://doi.org/10.1038/s41467-019-08561-y>
- [120] O. Bar-On, P. Brenner, U. Lemmer, and J. Scheuer, "Micro Lasers by Scalable Lithography of Metal-Halide Perovskites", *Advanced Materials Technologies* **2018**, vol. 3, no. 12, p. 1800212, doi: <http://doi.org/10.1002/admt.201800212>
- [121] N. Zhang, K. Wang, H. Wei, Z. Gu, W. Sun, J. Li, S. Xiao, and Q. Song, "Postsynthetic and Selective Control of Lead Halide Perovskite Microlasers", *Journal of Physical Chemistry Letters* **2016**, vol. 7, no. 19, pp. 3886-3891, doi: <http://doi.org/10.1021/acs.jpclett.6b01751>
- [122] J. Z. Song, Q. Z. Cui, J. H. Li, J. Y. Xu, Y. Wang, L. M. Xu, J. Xue, Y. H. Dong, T. Tian, H. D. Sun et al., "Ultralarge All-Inorganic Perovskite Bulk Single Crystal for High-Performance Visible-Infrared Dual-Modal Photodetectors", *Advanced Optical Materials* **2017**, vol. 5, no. 12, p. 1700157, doi: <http://doi.org/10.1002/adom.201700157>
- [123] W. Lee, J. Lee, H. Yun, J. Kim, J. Park, C. Choi, D. C. Kim, H. Seo, H. Lee, J. W. Yu et al., "High-Resolution Spin-on-Patterning of Perovskite Thin Films for a Multiplexed Image Sensor Array", *Advanced Materials* **2017**, vol. 29, no. 40, p. 1702902, doi: <http://doi.org/10.1002/adma.201702902>
- [124] Z. Li, Z. Li, Z. Shi, and X. Fang, "Facet-Dependent, Fast Response, and Broadband Photodetector Based on Highly Stable All-Inorganic CsCu<sub>2</sub>I<sub>3</sub> Single Crystal with 1D Electronic Structure", *Advanced Functional Materials* **2020**, vol. 30, no. 28, p. 2002634, doi: <http://doi.org/10.1002/adfm.202002634>
- [125] J. H. Heo, D. H. Shin, J. K. Park, D. H. Kim, S. J. Lee, and S. H. Im, "High-Performance Next-Generation Perovskite Nanocrystal Scintillator for Nondestructive X-Ray Imaging", *Adv Mater* **2018**, p. e1801743, doi: <http://doi.org/10.1002/adma.201801743>
- [126] Z. Zhang, H. Dierks, N. Lamers, C. Sun, K. Novakova, C. Hetherington, I. G. Scheblykin, and J. Wallentin, "Single-Crystalline Perovskite Nanowire Arrays for Stable X-ray Scintillators with Micrometer Spatial Resolution", *ACS Applied Nano Materials* **2022**, vol. 5, no. 1, pp. 881-889, doi: <http://doi.org/10.1021/acsanm.1c03575>
- [127] D. Zhang, Y. Yang, Y. Bekenstein, Y. Yu, N. A. Gibson, A. B. Wong, S. W. Eaton, N. Kornienko, Q. Kong, M. Lai et al., "Synthesis of Composition Tunable and Highly Luminescent Cesium Lead Halide Nanowires through Anion-Exchange Reactions", *Journal of the American Chemical Society* **2016**, vol. 138, no. 23, pp. 7236-9, doi: <http://doi.org/10.1021/jacs.6b03134>
- [128] Y. Tong, E. Bladt, M. F. Aygüler, A. Manzi, K. Z. Milowska, V. A. Hintermayr, P. Docampo, S. Bals, A. S. Urban, L. Polavarapu et al., "Highly Luminescent Cesium Lead Halide Perovskite Nanocrystals with Tunable Composition and Thickness by Ultrasonication", *Angewandte Chemie International Edition* **2016**, vol. 55, no. 44, pp. 13887-13892, doi: <http://doi.org/10.1002/anie.201605909>
- [129] X. Chen, H. W. Hu, Z. M. Xia, W. Gao, W. Y. Gou, Y. Q. Qu, and Y. Y. Ma, "CsPbBr perovskite nanocrystals as highly selective and sensitive spectrochemical probes for gaseous HCl detection", *Journal of Materials*

- Chemistry C* **2017**, vol. 5, no. 2, pp. 309-313, doi: <http://doi.org/10.1039/c6tc04136a>
- [130] G. Zhang, P. Song, Z. Shen, B. Qiao, D. Song, J. Cao, Z. Xu, W. Swelm, A. Al-Ghamdi, and S. Zhao, "CsPbBr<sub>3</sub>@CsPbBr<sub>3-x</sub>Cl<sub>x</sub> Perovskite Core-Shell Heterojunction Nanowires via a Postsynthetic Method with HCl Gas", *ACS Omega* **2020**, vol. 5, no. 20, pp. 11578-11584, doi: <http://doi.org/10.1021/acsomega.0c00824>
- [131] D. Parobek, Y. Dong, T. Qiao, D. Rossi, and D. H. Son, "Photoinduced Anion Exchange in Cesium Lead Halide Perovskite Nanocrystals", *Journal of the American Chemical Society* **2017**, vol. 139, no. 12, pp. 4358-4361, doi: <http://doi.org/10.1021/jacs.7b01480>
- [132] L. J. Xu, M. Worku, Q. He, H. Lin, C. Zhou, B. Chen, X. Lin, Y. Xin, and B. Ma, "Ligand-Mediated Release of Halides for Color Tuning of Perovskite Nanocrystals with Enhanced Stability", *Journal of Physical Chemistry Letters* **2019**, vol. 10, no. 19, pp. 5836-5840, doi: <http://doi.org/10.1021/acs.jpclett.9b02431>
- [133] D. Pan, Y. Fu, J. Chen, K. J. Czech, J. C. Wright, and S. Jin, "Visualization and Studies of Ion-Diffusion Kinetics in Cesium Lead Bromide Perovskite Nanowires", *Nano Letters* **2018**, vol. 18, no. 3, pp. 1807-1813, doi: <http://doi.org/10.1021/acs.nanolett.7b05023>
- [134] Y. Fujii, S. Hoshino, Y. Yamada, and G. Shirane, "Neutron-Scattering Study on Phase-Transitions of CsPbCl<sub>3</sub>", *Physical Review B* **1974**, vol. 9, no. 10, pp. 4549-4559, doi: <http://doi.org/10.1103/PhysRevB.9.4549>
- [135] S. Hirotsu, J. Harada, M. Iizumi, and K. Gesi, "Structural Phase-Transitions in CsPbBr<sub>3</sub>", *Journal of the Physical Society of Japan* **1974**, vol. 37, no. 5, pp. 1393-1398, doi: <http://doi.org/10.1143/Jpsj.37.1393>
- [136] H. Ohta, J. Harada, and S. Hirotsu, "Superstructure and Phase-Transitions in CsPbCl<sub>3</sub>", *Solid State Communications* **1973**, vol. 13, no. 12, pp. 1969-1972, doi: [http://doi.org/10.1016/0038-1098\(73\)90011-2](http://doi.org/10.1016/0038-1098(73)90011-2)
- [137] S. Plesko, R. Kind, and J. Roos, "Structural Phase-Transitions in CsPbCl<sub>3</sub> and RbCdCl<sub>3</sub>", *Journal of the Physical Society of Japan* **1978**, vol. 45, no. 2, pp. 553-557, doi: <http://doi.org/10.1143/Jpsj.45.553>
- [138] Z. Zhang, K. Suchan, J. Li, C. Hetherington, A. Kilgaridis, E. Unger, I. G. Scheblykin, and J. Wallentin, "Vertically Aligned CsPbBr<sub>3</sub> Nanowire Arrays with Template-Induced Crystal Phase Transition and Stability", *Journal of Physical Chemistry C* **2021**, vol. 125, no. 8, pp. 4860-4868, doi: <http://doi.org/10.1021/acs.jpcc.0c11217>
- [139] P. Jastrzebska-Perfect, W. Zhu, M. Saravanapavanantham, Z. Li, S. O. Spector, R. Brenes, P. F. Satterthwaite, R. J. Ram, and F. Niroui, "On-site growth of perovskite nanocrystal arrays for integrated nanodevices", *Nature Communications* **2023**, vol. 14, no. 1, p. 3883, doi: <http://doi.org/10.1038/s41467-023-39488-0>
- [140] A. A. Petrov, A. A. Ordinartsev, S. A. Fateev, E. A. Goodilin, and A. B. Tarasov, "Solubility of Hybrid Halide Perovskites in DMF and DMSO", *Molecules* **2021**, vol. 26, no. 24, doi: <http://doi.org/10.3390/molecules26247541>



- [141] S. Cheng and H. Zhong, "What Happens When Halide Perovskites Meet with Water?", *Journal of Physical Chemistry Letters* **2022**, vol. 13, no. 10, pp. 2281-2290, doi: <http://doi.org/10.1021/acs.jpclett.2c00166>
- [142] A. Kirakosyan, Y. Kim, M. R. Sihn, M. G. Jeon, J. R. Jeong, and J. Choi, "Solubility-Controlled Room-Temperature Synthesis of Cesium Lead Halide Perovskite Nanocrystals", *ChemNanoMat* **2020**, vol. 6, no. 12, pp. 1863-1869, doi: <http://doi.org/10.1002/cnma.202000471>
- [143] B. Li, D. Binks, G. Cao, and J. Tian, "Engineering Halide Perovskite Crystals through Precursor Chemistry", *Small* **2019**, vol. 15, no. 47, p. e1903613, doi: <http://doi.org/10.1002/sml.201903613>
- [144] J. S. Manser, M. I. Saidaminov, J. A. Christians, O. M. Bakr, and P. V. Kamat, "Making and Breaking of Lead Halide Perovskites", *Accounts of Chemical Research* **2016**, vol. 49, no. 2, pp. 330-8, doi: <http://doi.org/10.1021/acs.accounts.5b00455>
- [145] H. Dierks, Z. Zhang, N. Lamers, and J. Wallentin, "3D X-ray microscopy with a CsPbBr<sub>3</sub> nanowire scintillator", *Nano Research* **2022**, vol. 16, no. 1, pp. 1084-1089, doi: <http://doi.org/10.1007/s12274-022-4633-7>
- [146] M. Gandini, I. Villa, M. Beretta, C. Gotti, M. Imran, F. Carulli, E. Fantuzzi, M. Sassi, M. Zaffalon, C. Brofferio et al., "Efficient, fast and reabsorption-free perovskite nanocrystal-based sensitized plastic scintillators", *Nature Nanotechnology* **2020**, vol. 15, no. 6, pp. 462-468, doi: <http://doi.org/10.1038/s41565-020-0683-8>
- [147] W. F. Fu, A. G. Ricciardulli, Q. A. Akkerman, R. A. John, M. M. Tavakoli, S. Essig, M. V. Kovalenko, and M. Saliba, "Stability of perovskite materials and devices", *Materials Today* **2022**, vol. 58, pp. 275-296, doi: <http://doi.org/10.1016/j.mattod.2022.06.020>
- [148] L. Vegard, "Die Konstitution der Mischkristalle und die Raumfüllung der Atome", *Zeitschrift für Physik* **1921**, vol. 5, no. 1, pp. 17-26, doi: <http://doi.org/10.1007/bf01349680>
- [149] T. G. Liashenko, E. D. Cherotchenko, A. P. Pushkarev, V. Pakstas, A. Naujokaitis, S. A. Khubezhov, R. G. Polozkov, K. B. Agapev, A. A. Zakhidov, I. A. Shelykh et al., "Electronic structure of CsPbBr<sub>3-x</sub>Cl<sub>x</sub> perovskites: synthesis, experimental characterization, and DFT simulations", *Physical Chemistry Chemical Physics* **2019**, vol. 21, no. 35, pp. 18930-18938, doi: <http://doi.org/10.1039/c9cp03656c>
- [150] H. Buff, "Ueber das electrische Verhalten des Aluminiums", *Annalen der Chemie und Pharmacie* **1857**, vol. 102, no. 3, pp. 265-284, doi: <http://doi.org/10.1002/jlac.18571020302>
- [151] G. E. Thompson, "Porous anodic alumina: Fabrication, characterization and applications", *Thin Solid Films* **1997**, vol. 297, no. 1-2, pp. 192-201, doi: [http://doi.org/10.1016/S0040-6090\(96\)09440-0](http://doi.org/10.1016/S0040-6090(96)09440-0)
- [152] H. Masuda and K. Fukuda, "Ordered metal nanohole arrays made by a two-step replication of honeycomb structures of anodic alumina", *Science* **1995**, vol. 268, no. 5216, pp. 1466-8, doi: <http://doi.org/10.1126/science.268.5216.1466>

- [153] Y. Chen, G. Chen, Z. Zhou, X. Li, P. Ma, L. Li, W. Yin, H. Zeng, and G. Zou, "Amplifying Surface Energy Difference toward Anisotropic Growth of All-Inorganic Perovskite Single-Crystal Wires for Highly Sensitive Photodetector", *Advanced Functional Materials* **2021**, vol. 31, no. 31, doi: <http://doi.org/10.1002/adfm.202101966>
- [154] J. W. Mullin, "Crystal growth," in *Crystallization*, J. W. Mullin, Ed. Oxford: Butterworth-Heinemann, **2001**, pp. 216-288.
- [155] I. Y. Evchuk, R. I. Musii, R. G. Makitra, and R. E. Pristanskii, "Solubility of polymethyl methacrylate in organic solvents", *Russian Journal of Applied Chemistry* **2005**, vol. 78, no. 10, pp. 1576-1580, doi: <http://doi.org/10.1007/s11167-005-0564-9>
- [156] M. Lai, A. Obliger, D. Lu, C. S. Kley, C. G. Bischak, Q. Kong, T. Lei, L. Dou, N. S. Ginsberg, D. T. Limmer et al., "Intrinsic anion diffusivity in lead halide perovskites is facilitated by a soft lattice", *Proceedings of the National Academy of Sciences of the United States of America* **2018**, vol. 115, no. 47, pp. 11929-11934, doi: <http://doi.org/10.1073/pnas.1812718115>
- [157] Y. P. Liu, N. Lamers, Z. Zhang, N. Zaiats, A. Mikkelsen, J. Wallentin, R. Dittmann, and R. Timm, "Ion Migration and Redox Reactions in Axial Heterojunction Perovskite CsPb(Br(1-x)Clx)(3) Nanowire Devices Revealed by Operando Nanofocused X-ray Photoelectron Spectroscopy", *ACS Nano* **2024**, vol. 18, no. 51, pp. 34763-34775, doi: <http://doi.org/10.1021/acsnano.4c11458>
- [158] Y. Luo, P. Khoram, S. Brittman, Z. Zhu, B. Lai, S. P. Ong, E. C. Garnett, and D. P. Fenning, "Direct Observation of Halide Migration and its Effect on the Photoluminescence of Methylammonium Lead Bromide Perovskite Single Crystals", *Advanced Materials* **2017**, vol. 29, no. 43, doi: <http://doi.org/10.1002/adma.201703451>
- [159] M. Shahjahan, K. i. Yuyama, T. Okamoto, and V. Biju, "Heterojunction Perovskite Microrods Prepared by Remote-Controlled Vacancy Filling and Halide Exchange", *Advanced Materials Technologies* **2021**, vol. 6, no. 2, p. 2000934, doi: <http://doi.org/10.1002/admt.202000934>
- [160] J. J. Fritz and C. R. Fuget, "Vapor Pressure of Aqueous Hydrogen Chloride Solutions, 0° to 50° C", *Industrial & Engineering Chemistry Chemical & Engineering Data Series* **2002**, vol. 1, no. 1, pp. 10-12, doi: <http://doi.org/10.1021/i460001a002>
- [161] J. H. Hubbell, P. N. Trehan, N. Singh, B. Chand, D. Mehta, M. L. Garg, R. R. Garg, S. Singh, and S. Puri, "A Review, Bibliography, and Tabulation of K, L, and Higher Atomic Shell X-Ray-Fluorescence Yields", *Journal of Physical and Chemical Reference Data* **1994**, vol. 23, no. 2, pp. 339-364, doi: <http://doi.org/10.1063/1.555955>
- [162] A. Fick, "Ueber Diffusion", *Annalen der Physik* **1855**, vol. 170, no. 1, pp. 59-86, doi: <http://doi.org/10.1002/andp.18551700105>
- [163] J. Crank, *The Mathematics of Diffusion*, 2nd edition ed. Oxford, UK: Clarendon Press, **1975**.
- [164] S. Hammarberg, L. A. B. Marcal, N. Lamers, Z. Zhang, H. Chen, A. Bjorling, and J. Wallentin, "Nanoscale X-ray Imaging of Composition and Ferroelastic

- Domains in Heterostructured Perovskite Nanowires: Implications for Optoelectronic Devices", *ACS Applied Nano Materials* **2023**, vol. 6, no. 19, pp. 17698-17705, doi: <http://doi.org/10.1021/acsanm.3c02978>
- [165] L. A. B. Marcal, N. Lamers, S. Hammarberg, Z. Zhang, H. Chen, D. Dzhigaev, M. A. Gomez-Gonzalez, J. E. Parker, A. Bjorling, A. Mikkelsen et al., "Structural and chemical properties of anion exchanged CsPb(Br<sub>(1-x)</sub>Cl<sub>x</sub>)<sub>3</sub> heterostructured perovskite nanowires imaged by nanofocused x-rays", *Nanotechnology* **2024**, vol. 35, no. 26, doi: <http://doi.org/10.1088/1361-6528/ad355c>



